

B. Done

58 ✓
TP 76-8

Wave Reflection and Transmission at Permeable Breakwaters

by

Charles K. Sollitt and Ralph H. Cross III

TECHNICAL PAPER NO. 76-8
JULY 1976



Approved for public release;
distribution unlimited.

Prepared for
U.S. ARMY, CORPS OF ENGINEERS
COASTAL ENGINEERING
RESEARCH CENTER

Kingman Building
Fort Belvoir, Va. 22060

SECURITY CLASSIFICATION OF THIS PAGE (When Data Entered)

REPORT DOCUMENTATION PAGE		READ INSTRUCTIONS BEFORE COMPLETING FORM	
1. REPORT NUMBER TP 76-8	2. GOVT ACCESSION NO.	3. RECIPIENT'S CATALOG NUMBER	
4. TITLE (and Subtitle) WAVE REFLECTION AND TRANSMISSION AT PERMEABLE BREAKWATERS		5. TYPE OF REPORT & PERIOD COVERED Technical Paper	
7. AUTHOR(s) Charles K. Sollitt Ralph H. Cross III		6. PERFORMING ORG. REPORT NUMBER	
9. PERFORMING ORGANIZATION NAME AND ADDRESS Department of Civil Engineering Massachusetts Institute of Technology Cambridge, Massachusetts 02139		8. CONTRACT OR GRANT NUMBER(s) DACW72-68-C-0032	
11. CONTROLLING OFFICE NAME AND ADDRESS Department of the Army Coastal Engineering Research Center (CERRE-SP) Kingman Building, Fort Belvoir, Virginia 22060		10. PROGRAM ELEMENT, PROJECT, TASK AREA & WORK UNIT NUMBERS F31019	
14. MONITORING AGENCY NAME & ADDRESS (if different from Controlling Office)		12. REPORT DATE July 1976	
		13. NUMBER OF PAGES 172	
		15. SECURITY CLASS. (of this report) UNCLASSIFIED	
		15a. DECLASSIFICATION/DOWNGRADING SCHEDULE	
16. DISTRIBUTION STATEMENT (of this Report) Approved for public release; distribution unlimited.			
17. DISTRIBUTION STATEMENT (of the abstract entered in Block 20, if different from Report)			
18. SUPPLEMENTARY NOTES			
19. KEY WORDS (Continue on reverse side if necessary and identify by block number) Breakwaters Wave transmission Permeable breakwaters Waves Wave reflection			
20. ABSTRACT (Continue on reverse side if necessary and identify by block number) Rubble-mound breakwaters are designed to protect exposed marine areas from excessive wave activity. Observations of breakwaters interacting with surface waves in laboratory models and in full-scale field applications demonstrate that significant wave energy is transmitted through the interstices of structures commonly regarded as being impervious. The objective			

(Continued)

20. Abstract (Continued)

of this investigation is the development of a theoretical analysis to account for this phenomenon. The results are intended for use by coastal engineers to compare the effectiveness of alternative breakwater configurations, independent of repetitive experimental programs.

Three breakwater configurations are considered: (a) crib-style breakwaters with vertical walls and homogeneous fill; (b) conventional trapezoidal-shaped breakwaters with layered fill; and (c) pile-array breakwaters composed of vertical piles placed in symmetric patterns. The two-dimensional problem is studied. Waves are assumed to arrive at normal incidence.

The theoretical development begins with the unsteady equations of motion for flow in the voids of an arbitrary porous structure. The equations are linearized using a technique which approximates the known turbulent damping condition inside the structure. This yields a potential flow problem satisfied by an eigen-series solution. Linear wave theory is assumed to apply outside the structure and the excitation is provided by a monochromatic incident wave. The reflected, transmitted, solutions at the sea-breakwater interfaces and requiring continuity of pressure and horizontal mass flux. Inclusion of sloping-face structures necessitates an estimation of the breaking losses incurred on the windward slope. A semiempirical method is used to approximate the effect of wave breaking.

An experimental program is conducted to verify the analytical models. Theory and experiment yield the following general conclusions: (a) the transmission coefficient decreases with decreasing wavelength, breakwater porosity and permeability, and increasing wave height and breakwater width; (b) the reflection coefficient decreases with increasing wavelength, breakwater porosity and permeability, and decreasing breakwater width.

Application of the theory is limited to wave heights which exceed the medium grain diameter. Experimental results correlate better with the theoretical transmission coefficient than with the reflection coefficient. This seems to be due to the sensitivity of the reflection coefficient to surface effects.

The theory provides useful design estimates for all three breakwater water configurations and a full range of wavelengths. The proposed wave-breaking calculation gives favorable results for the sloping-face structure tested in this study. However, further comparison is needed to establish the general validity of the wave-breaking analysis.

PREFACE

This report is published to provide coastal engineers with the results of an investigation to develop a theoretical analysis to account for wave reflection and transmission at permeable breakwaters; and to compare the effectiveness of alternative breakwater configurations, independent of repetitive experimental programs. The work was carried out under the coastal construction program of the U.S. Army Coastal Engineering Research Center (CERC).

This report is published, with only minor editing, as received from the contractor; results and conclusions are those of the authors and are not necessarily accepted by CERC or the Corps of Engineers.


The report was prepared by Charles K. Sollitt (as partial fulfillment of the requirements for a Ph.D.), and by Dr. Ralph H. Cross III (who provided project supervision) of the Department of Civil Engineering, Massachusetts Institute of Technology (MIT), Cambridge, Massachusetts, under CERC Contract No. DACW72-68-C-0032. The research was carried out in the Ralph M. Parsons Laboratory for Water Resources and Hydrodynamics at MIT.

The authors gratefully acknowledge the contributions of Mr. Keh Wilson who performed most of the model construction (assisted by Mr. John Fisher), data acquisition, and reduction; and Mrs. Melissa Sollitt who assisted in the preparation of the figures. Dr. O.S. Madsen reviewed the initial drafts; his comments were helpful in the preparation of the final manuscript.

Dr. R.M. Sorensen, Chief, Coastal Structures Branch, was the CERC monitor for this report under the general supervision of Mr. R.P. Savage, Chief, Research Division.

Comments on this publication are invited.

Approved for publication in accordance with Public Law 166, 79th Congress, approved 31 July 1945, as supplemented by Public Law 172, 88th Congress, approved 7 November 1963.


WILSON P. ANDREWS
LTC, Corps of Engineers
Commander and Director

CONTENTS

	Page
SYMBOLS AND DEFINITIONS	8
I INTRODUCTION AND REVIEW OF PREVIOUS INVESTIGATIONS.	15
1. Introduction	15
2. Scope of the Investigation	16
3. Review of Previous Investigations.	17
4. Summary.	21
II THEORY.	21
1. Introduction	21
2. Derivation of the Equations of Motion for Damped, Small-Amplitude Water Waves in a Coarse Porous Medium.	22
3. Boundary Value Problem	34
4. Vertical-Wall Breakwaters.	45
5. Conventional Breakwater Schemes.	71
6. Pile-Array Breakwaters	79
III EXPERIMENTAL APPARATUS AND PROCEDURES	85
1. Introduction	85
2. Media Properties	86
3. Homogeneous Rectangular Breakwater	91
4. Trapezoidal-Layered Breakwater	93
5. Wave Testing Facilities and Procedures	97
IV EXPERIMENTAL AND THEORETICAL RESULTS.	101
1. Introduction	101
2. Homogeneous Crib-Style Breakwaters	102
3. Trapezoidal-Layered Breakwater	119
4. Pile-Array Breakwaters	126
5. Scale Effects and Prototype Application.	128
V CONCLUSION.	130
1. Summary.	130
2. Evaluation	131
3. Future Investigations.	132
LITERATURE CITED.	133
APPENDIX	
A ESTIMATING THE ROOTS TO THE COMPLEX DISPERSION EQUATION	137
B GENERAL CHARACTERISTICS OF THE COMPLEX DISPERSION EQUATION.	138
C EVALUATING LORENTZ'S CONDITION OF EQUIVALENT WORK	139
D COMPUTER PROGRAM LISTING.	144

CONTENTS

APPENDIX--Continued

	Page
E DISCRETIZATION OF NONHOMOGENEOUS BREAKWATER CROSS SECTIONS.	164
F PERMEABILITY AND FRICTION-FACTOR CALCULATIONS	166
G WAVE DATA FOR TRAPEZOIDAL-LAYERED BREAKWATER.	172

TABLES

1 Media physical properties	86
2 Media hydraulic properties.	91
3 Model dimensions.	91
4 Revised media hydraulic properties.	116

FIGURES

1 Friction factor versus Reynolds number.	29
2 Unconfined periodic flow.	35
3 Kinematic free-surface condition.	37
4 One term in the horizontal velocity distribution.	46
5 Crib-style breakwater	46
6 Reflection and transmission coefficient dependence on damping .	64
7 Reflection and transmission coefficient dependence on break-water width.	66
8 Reflection and transmission coefficient dependence on porosity	68
9 Reflection and transmission coefficient dependence on inertial coefficient.	69
10 Convergence dependence on number of eigen functions	70
11 Trapezoidal breakwater.	71
12 Equivalent rectangular breakwater	72
13 Pile-array pattern.	80
14 Drag coefficient versus Reynolds number, circular cylinder. . .	84

CONTENTS

FIGURES--Continued

	Page
15 Media samples	87
16 Permeameter	89
17 Friction factor versus Reynolds number.	92
18 Rectangular homogeneous crib-style breakwater	94
19 Trapezoidal-layered breakwater.	95
20 Trapezoidal-layered breakwater model.	96
21 Wave testing facility	98
22 Partial standing wave record.	100
23 Reflection and transmission coefficient dependence on wave steepness.	103
24 Reflection and transmission coefficient dependence on wave steepness.	104
25 Reflection and transmission coefficient dependence on wave steepness.	105
26 Reflection and transmission coefficient dependence on wave steepness.	106
27 Reflection and transmission coefficient dependence on wave steepness.	107
28 Reflection and transmission coefficient dependence on wave steepness.	108
29 Reflection and transmission coefficient dependence on wave steepness.	110
30 Reflection and transmission coefficient dependence on wave steepness.	111
31 Reflection and transmission coefficient dependence on wave steepness.	112
32 Reflection and transmission coefficient dependence on wave steepness.	113
33 Reflection and transmission coefficient dependence on wave steepness.	114

CONTENTS

FIGURES--Continued

	Page
34 Reflection and transmission coefficient dependence on wave number	115
35 Reflection and transmission coefficient sensitivity to media hydraulic properties	117
36 Reflection and transmission coefficient dependence on wave steepness.	120
37 Reflection and transmission coefficient dependence on wave steepness.	121
38 Reflection and transmission coefficient dependence on wave steepness.	122
39 Reflection and transmission coefficient dependence on wave steepness.	122
40 Reflection and transmission coefficient dependence on wave steepness.	123
41 Reflection and transmission coefficient dependence on wave steepness.	123
42 Reflection and transmission coefficient dependence on wave number	124
43 Reflection and transmission coefficient dependence on wave number	124
44 Transmission coefficient dependence on wave steepness, pile-array breakwater.	127

SYMBOLS AND DEFINITIONS

A	integration constant
A_p	average horizontal surface area per pile within array
A_1	constant with unit of length squared
A_2	constant with unit of length
A_I	per pore vertical projection of water surface area
A_{II}	cross-sectional pore area
a_i	incident wave amplitude
a_{rn}	n^{th} mode complex reflected wave amplitude
a_{tn}	n^{th} mode complex transmitted wave amplitude
a_1	complex amplitude of wave propagating in positive x-direction
a_2	complex amplitude of wave propagating in negative x-direction
a_{1n}	n^{th} mode complex amplitude of wave propagating in positive x-direction
a_{2n}	n^{th} mode complex amplitude of wave propagating in negative x-direction
B	integration constant
b	breakwater width (longitudinal extent)
b_1	horizontal projection of windward breakwater slope below stillwater level
b_2	trapezoidal breakwater width at stillwater level
b_3	horizontal projection of leeward breakwater slope below stillwater level
C_D	circular cylinder drag coefficient
C_f	turbulent friction coefficient governing high Reynolds number porous media losses
C_g	linear wave theory group celerity
C_M	virtual mass coefficient

SYMBOLS AND DEFINITIONS--Continued

C_n	phase velocity of nth mode
C_R	reflection coefficient
C_r	long-wave complex reflection coefficient
C_{rn}	dimensionless complex reflected amplitude of nth mode
C_T	transmission coefficient
C_t	long-wave complex transmission coefficient
C_{tn}	dimensionless complex transmitted amplitude of nth mode
C_1	dimensionless complex amplitude of wave propagating in positive x-direction
C_2	dimensionless complex amplitude of wave propagating in negative x-direction
C_{1n}	dimensionless complex amplitude of nth mode propagating in positive x-direction
C_{2n}	dimensionless complex amplitude of nth mode propagating in negative x-direction
C_δ	dimensionless amplitude of fictitious wave representing wave energy remaining after breaking
C_δ^i	Miches reflection coefficient from smooth impermeable slope
ch	hyperbolic cosine
cos	cosine
D	pile diameter and total derivative operator
d	equivalent sphere diameter and differential operator
\dot{E}_{loss}	period averaged power loss to wave breaking
e	natural logarithm base = 2.7183
F_p	wave force exerted on pile
f	dimensionless linearized friction or damping coefficient
f_{Kp}	permeability friction factor

SYMBOLS AND DEFINITIONS--Continued

f_s	dimensionless surface-roughness coefficient for breaking wave slope
g	acceleration due to gravity
H_i	incident wave height
H_o	deepwater incident wave height
h	water depth
$\Delta h/\Delta \ell$	head-loss gradient through a resistive medium
i	square root of minus one and incident wave subscript
\hat{i}	unit vector in positive x-direction
j	integral subscript identifying pile-array row number
\hat{j}	unit vector in lateral direction
K	complex wave number inside breakwater
K_n	n^{th} mode eigenvalue which is equal to the n^{th} mode complex wave number
K_p	permeability
K_{po}	non-Darcian permeability
k	linear wave theory progressive mode wave number
k_n	n^{th} mode linear wave theory wave number
k_n^r	real value of linear wave theory local mode wave number
\hat{k}	unit vector in positive z-direction
L	wavelength; unit of length
L_o	deepwater wavelength
m	subscript denoting mode number or a model parameter
N	number of particles in gravel sample
n	subscript denoting mode number
N_x	number of rows of piles longitudinally in pile array

SYMBOLS AND DEFINITIONS--Continued

N_y	number of rows of piles per unit width laterally in pile array
P	pore-averaged complex pressure or subscript denoting a prototype parameter
P_s	spatial perturbation pressure component
P_t	temporal perturbation pressure component
p^*	local instantaneous pressure
P_I, II, III	local pressure in zones I, II, and III, respectively
Q	complex local velocity vector with periodic time dependence removed
Q_I	imaginary component of Q
Q_R	real component of Q
Q_x	x-component of Q
Q_y	y-component of Q
q	pore-averaged complex vector seepage velocity
q_d	discharge velocity
q_R	real component of q
q_s	spatial perturbation velocity vector component
q_t	temporal perturbation velocity vector component
q^*	local instantaneous velocity vector, Eulerian
R_D	drag coefficient Reynolds number = uD/ν
R_{K_p}	permeability Reynolds number = $u\sqrt{K_p}/\nu$
r	reflected wave subscript
S	inertial coefficient
$S.G.$	specific gravity
SWL	stillwater level

SYMBOLS AND DEFINITIONS--Continued

sh	hyperbolic sine
sin	sine
T	wave period; temporal function
ΔT	increment of time
t	time; transmitted wave subscript
tan	tangent
th	hyperbolic tangent
U_I	real part of u
U_R	imaginary part of u
u	x-component of complex seepage velocity
\dot{u}	local rate of change of u
u_I, II, III	horizontal velocity in zones I, II, and III, respectively
V	volume
ΔV	incremental volume
W	weight of container filled with water and solids
W_f	weight of container filled with water
W_s	weight of container filled with solids
X	spatial function of x
x	longitudinal coordinate
y	lateral coordinate
Z	spatial function of depth
z	depth coordinate
α	ratio of imaginary to real part of complex wave number
α_n	ratio of imaginary to real part of nth mode complex wave number

SYMBOLS AND DEFINITIONS--Continued

β	radian slope of windward breakwater face
Γ	real part of complex wave number
Γ_n	real part of nth mode of complex wave number
γ	weight density of water
Δ	incremental prefix
∇	vector gradient operator = $\hat{i} \frac{\partial}{\partial x} + \hat{j} \frac{\partial}{\partial y} + \hat{k} \frac{\partial}{\partial z}$
δ	Miches intrinsic surface reflection coefficient
ϵ	porosity = ratio of void volume to total volume
η	wave surface profile
η_n	n th mode wave surface profile
η_1	surface profile of wave propagating in positive x-direction
η_2	surface profile of wave propagating in negative x-direction
θ, θ_1	phase angles
ν	kinematic viscosity of water
Π	3.14159265
ρ	mass density of water
σ	angular frequency of wave = $2 \Pi/T$
ϕ	velocity potential
ϕ_i	incident wave velocity potential
ϕ_n	n th mode velocity potential inside breakwater
ϕ_r	reflected wave velocity potential
ϕ_{rn}	n th mode reflected wave velocity potential
ϕ_t	transmitted wave velocity potential
ϕ_{tn}	n th mode transmitted wave velocity potential

SYMBOLS AND DEFINITIONS--Continued

$\phi_{I, II, III}$	velocity potential in zones I, II, and III, respectively
T	dummy variable
\bar{T}	temporal average of
\bar{x}	spatial average of
I	zone on windward side of breakwater
II	zone encompassing breakwater itself
III	zone on leeward side of breakwater
*	superscript denoting local instantaneous value or complex conjugate
∂	partial derivative operator

WAVE REFLECTION AND TRANSMISSION AT PERMEABLE BREAKWATERS

by
Charles K. Sollitt and Ralph H. Cross III

I. INTRODUCTION AND REVIEW OF PREVIOUS INVESTIGATIONS

1. Introduction.

It is common practice in coastal engineering design to account for wave transmission past rubble-mound breakwaters by considering two possible mechanisms: (a) diffraction around the ends of a structure or through navigation openings, and (b) overtopping across the crest of the structure. Standard optical techniques have been modified to successfully account for the diffraction process. The overtopping process is less well defined; however, recent semiempirical methods (Cross and Sollitt, 1971) have improved design capabilities.

Both procedures are based on the assumption that the structure itself is impervious. Engineers have been compelled to make this assumption because of inadequate design techniques for considering the alternative condition. Field and laboratory observations raise some doubts about the universal applicability of this assumption. Indeed, many structures seem to be highly pervious with respect to long-wave activity. The most graphic example of this is presented by the interaction of tides with breakwaters. Tidal motions are the manifestation of very low-frequency and low-steepness waves. They propagate through permeable rubble-mound breakwaters with little change in phase or range. In fact, the breakwater is practically transparent with respect to motions of this scale.

Significant transmission has also been reported for wave periods in the swell and storm wave range. Calhoun (1971) measured transmission and reflection coefficients in excess of 40 percent for 23-second waves at Monterey Harbor breakwater, Monterey, California. Similar observations have been made by the U.S. Army Engineer Division, New England, for the Isle of Shoals breakwater off the Maine-New Hampshire coast. Two-dimensional model tests conducted in conjunction with this study have demonstrated that some standard breakwater designs admit transmission coefficients greater than 30 percent for intermediate range wavelengths. In all of the above examples, no overtopping occurred.

Wave height constraints in protected high-density anchorage areas are quite severe. The Corps of Engineers restricts wave activity in its designs to wave heights less than 2 feet for commercial craft moorings and less than 1 foot for recreational craft moorings. Results of this study for standard three-layer breakwater structures indicate that transmission coefficients equal to 15 percent are attainable for water depth to wavelength ratios of 1 to 12, and wave height to wavelength ratios of 1 to 50. This yields transmitted wave heights greater than the recreational craft limit of 1 foot for a 12-second incident wave which has a height of 7 feet in a water depth of 27 feet.

The potential for harbor seiche in basins enclosed by permeable breakwaters is also great. This type of basin acts as an energy trap because any wave energy which is transmitted through the breakwater and which subsequently reflects off interior basin surfaces is also partially reflected off the interior breakwater slope. Initially, more wave energy is transmitted in through the breakwater than out. If the incident wave excitation persists, the energy level inside the basin may increase until equilibrium is reached between the incoming and outgoing wave energy. Consequently, the wave activity inside the harbor may become significant even though the transmission coefficient is small.

These few examples serve to illustrate that direct transmission through permeable breakwaters can be an important consideration in harbor design. Furthermore, assuming that rubble-mound breakwaters are impervious may lead to an erroneously low estimation of the wave activity on the leeward side of the breakwater.

To account for this feature in breakwater design it is necessary to have some method to predict the behavior of a permeable breakwater interacting with a surface wave train. A literature survey demonstrates that no independent design techniques are presently available and little has been written about the phenomenon itself. The results of this study are intended to contribute to both of these areas.

2. Scope of the Investigation.

The analytical approach used in this study begins with the unsteady equations of motion for flow in the pores of a coarse granular medium. The equations are linearized by a technique which approximates the known turbulent damping condition inside the medium. This yields a potential flow problem satisfied by an eigen-series solution. Linear wave theory is assumed to apply outside the breakwater and the excitation is provided by a monochromatic incident wave. The solutions are matched at the sea-breakwater interfaces by requiring continuity of horizontal mass flux and pressure.

Three different breakwater designs are considered: (a) crib-style breakwaters with vertical walls and homogeneous fill, (b) conventional, trapezoidal-shaped structures with layered fill, and (c) pile-array breakwaters composed of vertical piles placed in symmetric patterns. Inclusion of sloping-faced structures necessitates an estimation of the breaking losses incurred on the windward face of the breakwater. A semiempirical method, adapted from Miche (1951), is used to approximate the effect of wave breaking.

Experimental results are presented for crib-style and trapezoidal-layered models which are constructed and tested as a part of this study. Pile-array experimental data are taken from Costello (1952).

The theoretical solution is compared with experimental results and the following general conclusions are reached: (a) The transmission

coefficient decreases with decreasing wavelength, breakwater porosity and permeability, and increasing wave height and breakwater width, (b) the reflection coefficient decreases with increasing wavelength, breakwater porosity and permeability, and decreasing breakwater width. Experimental results correlate better with the theoretical transmission coefficient than with the reflection coefficient. This seems to be due to the sensitivity of the reflection coefficient to surface effects. Application of the theoretical results is limited to wave heights which are larger than the medium grain diameter and to wave steepnesses which are within the linear wave theory range.

3. Review of Previous Investigations.

Some of the early work in permeable structures was directed toward an understanding of the behavior of wave filters. Wave filters are very porous structures which are placed in front of laboratory wave generators to reduce surface ripples, higher harmonics, and secondary reflections, in experimental wave trains. Filters are similar to breakwaters in that they cause partial reflection and reduced transmission of the incident wave.

Biéssel (1950) developed one of the first analytical approaches to this problem. His work identified the unsteady potential flow equations of motion for a hypothetical wave filter which was infinitely long, 100 percent porous, and which resisted fluid motion according to Darcy's law. The resulting boundary value problem was similar in form to that derived in this study. However, his solution was expressed in a particular form which incorporated some of the frequency-dependent features and the wave amplitude in an undefined leading coefficient. Nevertheless, Biéssel showed that the motion decays exponentially in the direction of wave propagation. The decay rate and wavelength were specified by a pair of dispersion equations which paralleled those obtained in this study. The results were not applied to any specific examples.

Although Biéssel (1950) did not actually solve the wave filter problem, his work was significant because it identified the form of the spatial and temporal functions which described a linearly damped, periodic, free-surface motion.

Le Méhauté (1957) recognized that the resistance forces in large-scale granular media were not prescribed by Darcy's law. However, to develop an analytical solution he assumed that a resistance law could be written which was linearly proportional to the local velocity. He anticipated that a constant of proportionality could be fitted to the theoretical approximation which would be subsequently evaluated by comparison with experimental results. He further recognized that any imbalance of pressure and resistance forces in the flow results in an acceleration of the pore velocity rather than the local gross flow rate. This permitted him to account for the effect of porosity in his equations of motion. He prescribed an irrotational velocity field so the boundary value problem became similar to Biéssel (1950). Le Méhauté (1957) accepted Biéssel's

solution to the problem without resolving the dynamic free-surface condition to find the correct combination of parameters to specify the actual wave surface profile. Comparison of Le Méhauté's velocity potential with this study or with Ijima, Eguchi, and Kobayashi (1971) makes this error apparent. In addition, Le Méhauté's pair of dispersion equations was presented incorrectly, as demonstrated by comparison with Biéssel's results. These errors do not affect the outcome of Le Méhauté's study because he ultimately abandoned the solution for the declared reason that the equations were too cumbersome to extract answers. As an alternative, he accepted the experimental results that reflection coefficients are nearly constant to 60 percent, and he modified that part of the theory which predicts exponential decay in the internal wave amplitude to formulate an empirical equation for the transmission coefficient. He attempted to evaluate the constants in his empirical expression by comparison with experiments, but the results were inconclusive. Consequently, Le Méhauté (1957) concluded his study without having solved either the wave filter or the permeable breakwater problem.

In addition to analytical studies, Le Méhauté conducted an extensive experimental program on multilayered, sloping-faced breakwaters and homogeneous crib-style breakwaters. However, his results cannot be used to verify other theories because he did not determine the hydraulic properties of the media composing the models. Section II shows that these properties are necessary inputs to independent analytical solutions.

The studies of Biéssel (1950) and Le Méhauté (1957) were important because they represent the first attempts to define the nature of wave motion within a porous media. Significant advances on their work were not made for more than a decade. During the interim many investigators attempted approximate methods of solution by combining linear wave theory with various energy conservation requirements. The work of the following four investigators typifies this latter approach.

Straub and Herbich (1956) proposed an artificial viscosity theory to account for wave damping in a filter. They combined the Navier-Stokes laminar dissipation function with a linear progressive wave theory velocity field to determine the power consumed by the filter. The kinematic viscosity was replaced by an artificial viscosity and the value of the latter was adjusted until theory and experiment agree. The method is not generally applicable to less permeable structures because the linear progressive wave theory assumption is invalid inside the structure. In addition, wave reflection is ignored and it is impossible to predict the artificial viscosity *a priori*.

Goda and Ippen (1963) conducted experimental and theoretical studies of wave filters composed of wire-mesh screens. An analysis was performed which resolved the mesh into two sets of horizontal and vertical cylinders. Linear wave theory was assumed to give the proper depth and temporal dependence for the velocity field. The power loss was computed from well-known drag-force relationships on circular cylinders. Partial reflection from individual screens was ignored so that the change in energy flux across

each screen was simply equated to the power loss at the screen. Linear drag-force relationships on circular cylinders. Partial reflection from individual screens was ignored so that the change in energy flux across each screen was simply equated to the power loss at the screen. Linear wave theory established the relationship between energy flux and wave amplitude; the total effect of the filter was found by summing across each screen. The theory was not completely independent since it had to be calibrated to experimental results to determine the appropriate unsteady drag-coefficient relationship. After this calibration was performed, the correlation between experimental and theoretical transmission coefficients was quite good. However, the method can not be applied to less porous structures because neglecting wave reflection becomes a poor approximation. Furthermore, linear wave theory does not adequately describe the flow field in less permeable structures.

Keulegan (1948) also used an energy dissipation approach to analyze wave damping in composite screen filters. Instead of superimposing the drag force on rows and columns of cylinders to predict the effective screen-resistance coefficient, Keulegan measured the quantity directly in separate uniform flow tests. He used both cnoidal and linear wave theory to relate the particle velocity to the wave amplitude between adjacent screens. Then, assuming the local wave energy to be proportional to the square of the local amplitude, he wrote a differential equation which expressed the rate of change of amplitude as a function of the power lost to filter resistance forces. The solution ultimately requires that one or more parameters be evaluated by comparison with experimental results. As with the previous wave filter theories, the solution cannot be applied to less porous structures because it does not account for wave reflection.

Kamel (1969) modified Keulegan's (1948) theory for wave filters and applied it to idealized homogeneous crib-style breakwaters. The structures were fabricated from vertical-walled wire baskets filled with spheres or cubes. Experimental reflection coefficients exceeding 60 percent were reported and yet this important process was ignored in the analysis. A fitting parameter which was used to calibrate the theory to the experiments was evaluated. The parameter should be constant for a particular breakwater, but it varies by almost an order of magnitude. This result tends to confirm that wave filter theories which do not account for wave reflection simply do not model less pervious structures correctly.

Sawargi and Koichiro (1970) employed a technique similar to that of Goda and Ippen (1963) to analyze wave transmission through arrays of vertical cylindrical piles. They assumed that linear wave theory applied in the region between rows of piles and solved the unsteady Bernoulli equation for the effect of drag-force losses across the piles. Horizontal mass continuity was also required. This second condition permitted the investigators to solve the reflection coefficient as well as the transmission coefficient. Several approximations were made to expedite the solution: (a) the reflected and transmitted waves were assumed to be in phase with the incident wave, (b) long-wave conditions were assumed so that depth dependence could be ignored, and (c) the temporal functions

were all evaluated with the arguments arbitrarily set equal to $\pi/2$. Theoretical and experimental results were compared and the drag coefficient was evaluated to optimize correlation. Results were presented for one- and two-row configurations and only one incident wave condition, so general conclusions are not readily inferred. However, the three stated approximations would seem to limit the applicability of the results.

Kondo (1970) developed an analytical approach to long-wave interaction with homogeneous, vertical-face breakwaters. He solved the one-dimensional equation of motion for periodic, linearly damped free-surface flow in porous media. The linear damping law approximated the known turbulent damping law by requiring that the two expressions yield the same time average resistance force at the center of the breakwater. Kondo's general solution was similar to that developed by Lean (1967) for permeable absorbers. It yielded exponential decay of wave amplitude in the direction of wave propagation. Linear wave theory was applied outside the breakwater and the two solutions were coupled by requiring continuity of horizontal velocity and pressure at the sea-breakwater interfaces. The boundary conditions yielded solutions to the reflected and transmitted wave amplitudes. Experimental and theoretical transmission coefficients were compared. Although considerable scatter was present in the result, correlation for short-wave data was significantly better than for long-wave data. This paradox was left unexplained but may be partially due to Kondo's approximate method of evaluating the linear damping coefficient. The analysis cannot be applied to the general case of intermediate or short-wave excitation unless the equations of motion are rewritten to account for depth dependence. Wave interaction with conventional breakwater forms was not discussed.

The work of Ijima, Eguchi, and Kobayashi (1971) was conducted simultaneously and independently of the investigation described herein. Although both studies solve similar boundary value problems for homogeneous crib-style breakwaters, there are several important differences which distinguish the two solutions. These investigators began with Le Méhauté's (1957) boundary value problem and developed a solution in terms of an unknown linearized damping coefficient. They evaluated the coefficient by fitting the theoretical solution to experimental data. This fitting technique yielded empirical equations which equate the damping coefficient to functions of the incident wave properties for a particular model breakwater. The empirical equations did not include the effect of media properties on breakwater dimensions. They were valid only for the conditions existing in the model which was used to generate the equations. This precluded the use of the theory independent of model studies.

In the present investigation, the boundary value problem is derived from fundamental considerations. The simplifying assumptions and limiting conditions are identified and discussed. A technique is defined which permits a linearized damping law to be determined in terms of known media properties and independent of model breakwater data. An eigen-series solution is developed for readily identified wave and

breakwater parameters as opposed to the auxiliary variables used in the solution by Ijima, Eguchi, and Kobayashi (1971).

Ijima, Eguchi, and Kobayashi did not investigate layered or sloping-face structures. Nevertheless, their work verified the form of the complex eigen-series solution used in this study to describe the velocity field for idealized crib-style breakwaters. In addition, their work substantiated a prior assertion that the solutions proposed by Biéssel (1950) and Le Méhauté (1957) were incomplete in their published form.

4. Summary.

This brief survey summarizes the state of technology as applied to permeable breakwater analysis. It may be concluded that presently available theories can not predict wave transmission through idealized structures for a variety of incident wave conditions unless experimental breakwater tests are conducted simultaneously. Scaling of the results to prototype conditions has not been considered. Furthermore, no theories have been proposed to include the effect of heterogeneous layering or inclined surfaces. In the following sections, each of these important problems is considered.

II. THEORY

1. Introduction.

The literature review revealed a need for a theory to predict the effect of a permeable structure interacting with a surface wave train. The analytical part of this study is formulated to provide insights into breakwater behavior for a variety of wave and structural conditions. The total solution may be divided into two major parts. First, general solutions are derived for the flow fields inside and outside of the permeable structure. Second, the two general solutions are coupled with some specified excitation to yield the complete problem solution. The major effort is employed in describing the fluid motion within the interstices of the permeable structure.

An overview of the solution technique begins with a close look at the flow field within the structure. Most structures of interest, e.g., rubble-mound breakwaters, are composed of materials which are randomly shaped and placed so that it becomes impractical, if not impossible, to specify the local instantaneous velocity and pressure at all interior points. The first part of this section identifies an appropriate substitute velocity and pressure field which can be evaluated. The resulting quantities are the pore-averaged seepage velocity and pressure. The Navier-Stokes equations are operated on to reveal the character of these quantities and to disclose the dominant stresses which govern their behavior. One of these stresses is the total stress tensor of apparent turbulent friction. It is intractable in its general form and is replaced by an established damping law which is a deterministic function of the seepage velocity. This leads to a set of equations which are linearized to

permit an analytical solution. The linearized equations specify a boundary value problem which is shown to be satisfied by a series of eigen functions. The problem inside the structure is solved using standard techniques and the important features are discussed. The internal solution is coupled to a linear wave theory solution outside the structure by requiring continuity of velocity and pressure at the sea-structure interfaces. The orthogonal properties of the solution are used to reduce the coupled expressions to simple algebraic equations for the reflected, transmitted, and internal wave amplitudes. The equations are reduced further for the case of long-wave excitation. After discussing the solution behavior for vertical-faced breakwaters, an approximate method is introduced to apply the results to conventional breakwater forms. Finally, a solution for pile-array breakwaters is presented.

2. Derivation of the Equations of Motion for Damped, Small-Amplitude Water Waves in a Coarse Porous Medium.

a. A Microscopic View. A complete mathematical description of flow through a coarse granular material requires exact information about the shape, location, and orientation of each individual particle. If the geometry of the sample of interest is precisely known, then one can proceed with the incompressible Navier-Stokes equations and the necessary boundary conditions to describe the velocity and pressure distribution. The appropriate equation of motion is:

$$\frac{Dq^*}{Dt} = -\frac{1}{\rho} \nabla (p^* + \gamma z) + \nu \nabla^2 q^*,$$

with

$$\nabla \cdot q^* = 0,$$

where q^* is the actual, instantaneous Eulerian velocity vector at any point; p^* is the corresponding pressure; γ is the fluid weight density; ρ is the fluid mass density; ν is the fluid kinematic viscosity; z is the vertical coordinate; t is time; ∇ is the gradient operator

$$(\nabla = \hat{i} \frac{\partial}{\partial x} + \hat{j} \frac{\partial}{\partial y} + \hat{k} \frac{\partial}{\partial z})$$

in an orthogonal coordinate system; and D/Dt is the total derivative

$$\left(\frac{D}{Dt} = \frac{\partial}{\partial t} + q^* \cdot \nabla\right).$$

Obtaining an exact geometric description of a closely packed structure of randomly placed and shaped particles would be a very difficult and tedious task. Solving the equations of motion for such a complex geometry would require extensive computer memory and time. A more reasonable approach to the problem is to determine the important physical and hydraulic properties of the media and then evaluate the macroscopic

flow field in terms of these properties. This approach yields the well-known seepage velocity concept in porous media flow.

b. Applying the Seepage Velocity Concept to the Equations of Motion.

The seepage velocity concept assumes that pores and flow-resistance properties are uniformly distributed throughout the structure in some known manner. The analysis attempts to evaluate velocities and pressures which are averaged over the small but finite pore volumes. The resulting solution yields the "seepage velocity" which ignores perturbations in the flow field due to the presence of individual particles and pore irregularities.

The applicability of the Navier-Stokes equations has been established historically. For the present application it is necessary to operate on these equations and the flow variables to replace the actual velocity with the seepage velocity. To accomplish this the local instantaneous vector velocity, q^* , is resolved into three components:

$$q^* = q + q_s + q_t,$$

where q is the seepage velocity, the average velocity within small but finite and uniformly distributed void spaces; q_s is a spatial perturbation accounting for local additional velocity components due to pore irregularities or boundary layers; and q_t is the time perturbation accounting for local transient eddy fluctuations within the pores. q and q_s are time-averaged over intervals large enough to eliminate q_t but small enough so as to not hide the overall unsteady effects associated with the macroscopic flow field.

If a velocity probe is inserted into a pore, the total velocity q^* will be measured at any instant. However, if the total velocity is measured at a point for some small-time interval, ΔT , and the average velocity within that time interval is determined, then the resulting quantity is simply the seepage velocity, q , plus the spatial perturbation, q_s , associated with that location in the pore. If several probes were able to perform this same temporal average simultaneously at different points throughout the pore, then the spatial average of all of the temporal averages is simply the mean velocity in the pore at that instance, q . Likewise, the pressure may be written as:

$$p^* = p + p_s + p_t.$$

Utilizing these definitions, one may operate on the complete Navier-Stokes equations to determine the effect of the transient and spatial perturbations on the mean flow within the pore. The time-averaging operation is defined as:

$$\bar{T} = \frac{1}{\Delta T} \int_t^{t + \Delta T} T dt,$$

where T is any quantity of interest and ΔT is much smaller than the time scale of macroscopic unsteadiness. Then,

$$\overline{q^*} = \overline{(q + q_s + q_t)} = q + q_s,$$

because, by definition, the time average of q_t is zero. Similarly, all functions linear in q_t average to zero.

The total derivative may be expanded to reveal its local and convective terms;

$$\frac{Dq^*}{Dt} = \frac{\partial q^*}{\partial t} + (q^* \cdot \nabla) q^*.$$

When this is introduced into the Navier-Stokes equation and the temporal integration is performed, the result is:

$$\begin{aligned} \frac{\partial}{\partial t} (q + q_s) + (q + q_s) \cdot \nabla (q + q_s) + \overline{q_t \cdot \nabla q_t} \\ = - \frac{1}{\rho} \nabla (p + p_s + \gamma z) + \nu \nabla^2 (q + q_s), \end{aligned}$$

with

$$\nabla \cdot (q + q_s) = 0.$$

The effect of spatial fluctuations within the pore may be isolated by integrating the equations of motion over small but finite pore volumes, ΔV . The volume average is defined as:

$$\overline{\quad} = \frac{1}{\Delta V} \int_{\Delta V} T dV.$$

Within any particular pore there is, by definition, an equal distribution of positive and negative q_s 's. Consequently, the pore-averaged q_s is zero and all functions linear in q_s integrate to zero over the pore volume if the pore volume, ΔV , remains constant throughout the medium. This last condition allows one to interchange the order of the spatial integration and the gradient operation, Thus,

$$\overline{(q + q_s)} = q,$$

and the pore volume-averaged Navier-Stokes equations become:

$$\frac{\partial q}{\partial t} + q \cdot \nabla q + \overline{q_s \cdot \nabla q_s} + \overline{q_t \cdot \nabla q_t} = - \frac{1}{\rho} \nabla (p + \gamma z) + \nu \nabla^2 q.$$

To be completely rigorous, these equations should be applied only to homogeneous media where the length scale of the seepage motion is much greater than a pore diameter.

c. The Effect of the Spatial and Temporal Fluctuations. It is apparent from the form of the resulting equations that the effect of the spatial and temporal fluctuation is to modify the seepage velocity in a manner analogous to a Reynolds stress (Schlichting, 1968). However, this stress is distinguished from the usual Reynolds stress in the turbulent Navier-Stokes equation in that it contains a spatially derived component,

$$\overline{q_s \cdot \nabla q_s},$$

and a transient eddy component,

$$\overline{\dot{q}_t \cdot \nabla q_t}.$$

These terms remain in the equations of motion after the two integrating operations have been performed because of the inherent nonlinearity of the convective acceleration terms. They may be interpreted as stresses with respect to the mean motion because they consume momentum from the force imbalance on the right-hand side of equation and thus prohibit this momentum from being transferred to the mean motion. As a result of the momentum-consumption character of these terms, it is customary to transpose them to the right-hand side of the equation where they assume the identity of a stress tensor.

d. Scaling Arguments. It is important to note that q , q_s , and q_t may all be of the same order of magnitude. Two examples illustrate this. At solid boundaries, the no-slip requirement imposes the restriction that

$$q^* = q + q_s + q_t = 0.$$

Likewise, eddy fluctuations must vanish at solid boundaries, so:

$$q_s = -q.$$

The magnitude of the transient eddies may be argued heuristically if one accepts the idea that some of the eddies result from vortex shedding at abrupt protrusions in the pore. Since the velocity distribution must be continuous from the external flow through the vortex, it is necessary that the magnitude of the velocity near the edge of the vortex be of the same order as external flow. Consequently, $q_t \sim O(q)$. This result concurs with the large turbulent velocity components observed in turbulent jets and wakes (Rouse, 1959).

However, the magnitudes of the respective velocity gradients may be entirely out of scale. Gradients in the seepage velocity occur over a distance corresponding to a macroscopic flow-field length scale. For the

particular problem of interest, this scale is represented by a wavelength. Gradients in the spatial and temporal velocity perturbations occur over distances on the order of a pore diameter. For problems of any practical importance, the wavelength is always much greater than the pore diameter, thus,

$$\nabla q \ll \nabla q_s, \nabla q_t,$$

and

$$q \cdot \nabla q \ll \frac{q_s \cdot \nabla q_s}{q_s} + \frac{q_t \cdot \nabla q_t}{q_t}.$$

As a result of these order of magnitude arguments, the convective acceleration term containing the seepage velocity will be ignored. This simplification is consistent with the small-amplitude wave assumption to be imposed subsequently.

The small-amplitude wave assumption leads directly to linear wave theory in the region exterior to the breakwater. In linear wave theory, one assumes that the quadratic terms in the equation of motion may be ignored. The quadratic terms are the velocity products in the convective acceleration terms. Wave field velocities are proportional to the wave amplitude divided by the wave period. Because damping causes a reduction in wave amplitude within the breakwater, the quotient of wave amplitude divided by wave period should be smaller inside the breakwater than outside. Consequently, it is consistent with linear wave theory to neglect seepage velocity convective acceleration terms in the equation of motion.

A solution is developed later in this study for a pile-array breakwater. It will be shown that for the case of widely spaced piles, the equations of motion are similar to the large-grain porous media problem with an additional requirement imposed by the added mass of the pile. This requirement introduces the virtual mass coefficient, C_M , to the local acceleration term such that $\partial q / \partial t$ becomes $(1 + \text{func.}(C_M)) \partial q / \partial t$. To incorporate this effect into the general derivation, a coefficient $S = (1 + \text{func.}(C_M))$ is introduced as a cofactor in the local acceleration term. It should be understood that with respect to porous media flow, S has a value of unity.

e. Turbulent Damping Law. The spatial and temporal Reynolds stress terms are combined with the laminar shear stress to yield the total stress tensor of apparent turbulent friction. With the assumption of small convective seepage acceleration the equation of motion becomes:

$$S \frac{\partial q}{\partial t} = -\frac{1}{\rho} \nabla (p + \gamma z) + \nu \nabla^2 q - \left(\frac{q_s \cdot \nabla q_s}{q_s} + \frac{q_t \cdot \nabla q_t}{q_t} \right), \quad (1)$$

with

$$\nabla \cdot q = 0.$$

Equation (1) represents the equation of motion for the seepage velocity and pressure with a total stress tensor which accounts for the effect of local spatial and temporal fluctuations.

The total stress tensor contains a laminar damping term and a turbulent damping term. The laminar term is linearly proportional to a velocity and inversely proportional to the square of the gradient length scale. The turbulent damping term is directly proportional to the square of a velocity and inversely proportional to the gradient length scale. The quantities q_s and q_t can not be evaluated directly. However, it is possible to relate them to other deterministic quantities in a manner which retains the essential character of the total stress tensor.

One might hypothesize from the structure of the stress tensor that the laminar term could be replaced by an equivalent damping law,

$$\nu \nabla^2 q \rightarrow \frac{\nu q}{A_1 \{L^2\}}.$$

Similarly, using the seepage velocity to scale q_s and q_t , the turbulent term could be replaced by:

$$\frac{\overline{q_s \cdot \nabla q_s}}{(q_s \cdot \nabla q_s)} + \frac{\overline{q_t \cdot \nabla q_t}}{q_t \cdot \nabla q_t} \rightarrow \frac{q^2}{A_2 \{L\}},$$

where $\{ \}$ refers to the units of the quantities, A_1 and A_2 . In fact, it has been demonstrated that under steady, nonconvective flow conditions the pressure drop through large-grain permeable media is specified by (Ward, 1964; Dinoy, 1971):

$$-\frac{1}{\rho} \nabla (p + \gamma z) = \frac{\nu q_d}{K_p} + \frac{C_f}{K_p^{1/2}} q_d |q_d|. \quad (2)$$

For the conditions stated, this established the equivalency of:

$$\nu \nabla^2 q - \left(\frac{\overline{q_s \cdot \nabla q_s}}{q_s \cdot \nabla q_s} + \frac{\overline{q_t \cdot \nabla q_t}}{q_t \cdot \nabla q_t} \right) = - \frac{\nu q_d}{K_p} + \frac{C_f}{K_p^{1/2}} q_d |q_d|, \quad (3)$$

where K_p is the intrinsic permeability, a hydraulic property of the medium with a dimension of length squared; C_f is a dimensionless turbulent coefficient; and q_d is the discharge velocity. The discharge velocity is a conceptual quantity defined by distributing the seepage velocity over the solid volume as well as the void volume. The discharge velocity is analytically expedient in that it allows one to apply the continuum concept to flow fields with unknown internal boundaries.

Algebraically, the discharge velocity may be expressed as the product of the seepage velocity and the porosity, ϵ :

$$q_d = \epsilon q, \quad (4)$$

where

$$\epsilon = \frac{\text{void volume}}{(\text{void} + \text{solid}) \text{ volume}}.$$

K_p and C_f may be spatial variables and in an isentropic medium they may be directionally sensitive. In general, tensor notation would be appropriate for the friction term. Nevertheless, this discussion will use vector notation. However, note that K_p and C_f assume their proper values in the direction of q .

One important feature of this damping law is that for low Reynolds number flows, i.e., $q_d^2 \ll q_d$, the equation reduces to Darcy's Law for flow in porous media:

$$-\frac{1}{\rho} \nabla (p + \gamma z) = \frac{v q_d}{K_p}.$$

A useful consequence of the steady-state damping law expressed in equation (2) is that it facilitates the definition of a friction factor or loss coefficient analogous to pipe flow. Specifically,

$$-\frac{1}{\rho} \nabla (p + \gamma z) = \frac{v q_d}{K_p} + \frac{C_f q_d |q_d|}{K_p^{1/2}} = f_{K_p} \frac{q_d |q_d|}{K_p^{1/2}}. \quad (5)$$

Then,

$$f_{K_p} = \frac{1}{R_{K_p}} + C_f, \quad (6)$$

where

$$R_{K_p} = \frac{|q_d| K_p^{1/2}}{v},$$

a permeability Reynolds number, and f_{K_p} is the media friction factor. Utilizing equations (5) and (6), it is possible to construct a "Moody Diagram" for turbulent flow in porous media. Such a diagram was constructed by Dinoy (1971) and is shown in Figure 1; in the figure, d represents the media grain size and $d/\sqrt{K_p/\epsilon}$ is a relative roughness proposed by Dinoy. This figure substantiates the validity of the proposed damping law for several different materials. Experiments verify that

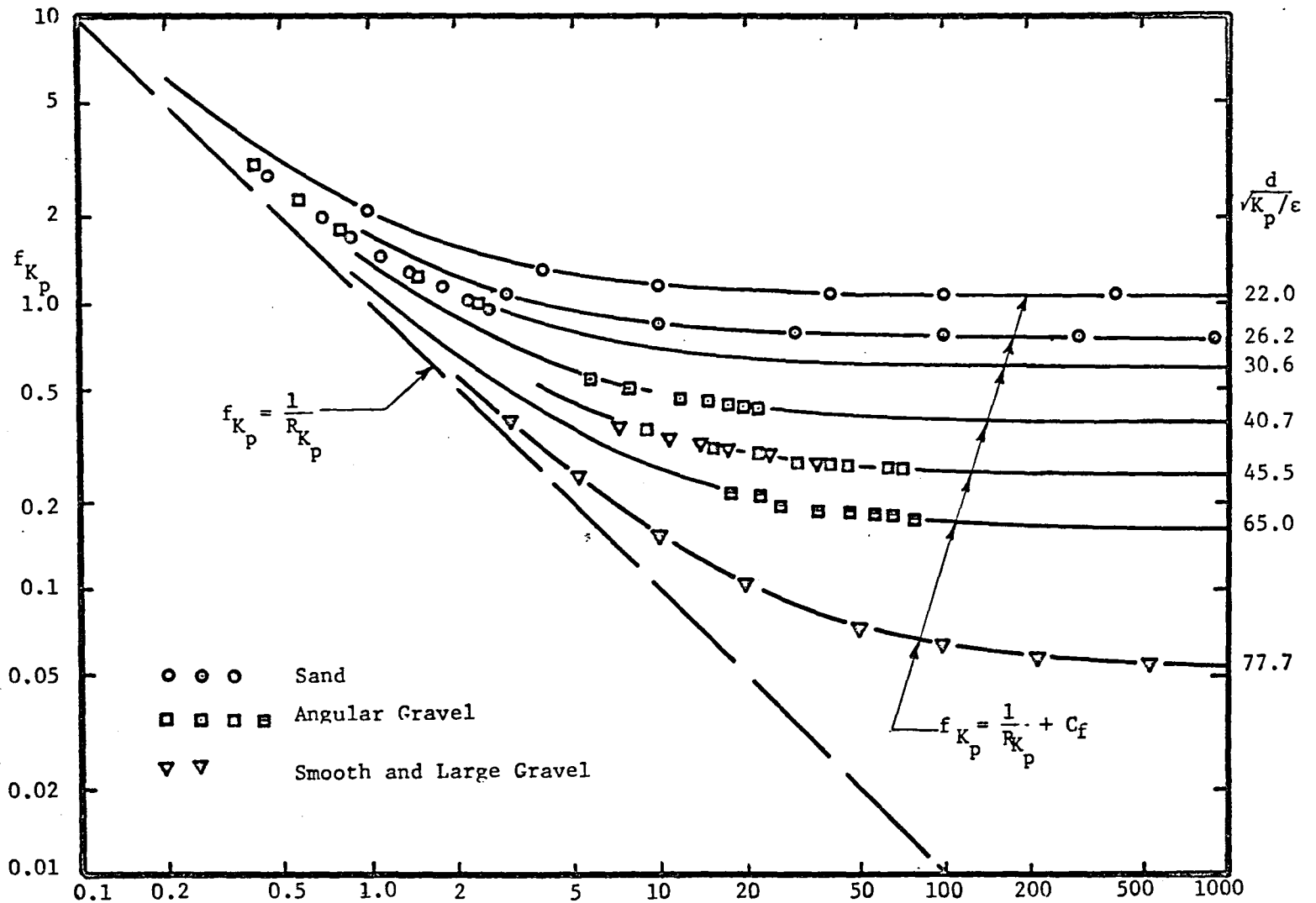


Figure 1. Friction factor versus Reynolds number $R_{K_p} = q\sqrt{K_p}/v$ (Dinoy, 1971).

damping becomes pure Darcian (linear) at low Reynolds numbers and fully turbulent, square-law damping at high Reynolds numbers, again as in pipe flow.

The applicability of the discharge velocity damping law expressed in equation (2) has been established for steady, nonconvective flows. Other investigators have tested this law for unsteady flows. Shuto and Hashimoto (1970) reported, "Resistance coefficients obtained in steady and oscillatory flows show almost no difference." However, their study was limited to periods of oscillation greater than 3.4 seconds. The experiments were performed on various size models of artificial armor-layer materials in a large U-tube-type permeameter. Free oscillations were induced by imposing an instantaneous head difference across the ends of the U-tube. Because of the relatively long periods, the results have important implications for prototype-wave excitation but may not necessarily apply to all small-scale laboratory conditions.

The effect of acceleration in the flow is not well defined. However, Wright (1968) found that converging flows impede turbulence and cause a relative decrease in the resistance coefficient. Diverging flows induce separation from physical boundaries, thereby increasing turbulence and the resistance coefficient. In periodic fluid motions, the flow accelerates and converges during one-half cycle while it decelerates and diverges over the remaining one-half cycle. The two effects are partially compensating so that the total hydraulic resistance during one cycle may approach that indicated by the steady-state resistance coefficient. In the absence of more definitive information, it is assumed in this study that periodic flows cause the same mean resistance to flow during one cycle as that indicated by steady-state resistance tests. Consequently, the permeability, K_p , and turbulent friction coefficient, C_f , obtained by conventional methods in steady-state tests are accepted as adequate descriptions of the medium hydraulic properties and equation (3) becomes the appropriate damping law for oscillatory flow. Substituting equations (3) and (4) into equation (1) yields:

$$S \frac{\partial q}{\partial t} = -\frac{1}{\rho} \nabla (p + \gamma z) - \frac{v \epsilon q}{K_p} - \frac{C_f \epsilon^2}{K_p^{1/2}} q |q|, \quad (7)$$

with

$$\nabla \cdot q = 0.$$

Equation (7) represents a significant improvement over equation (1). The damping term is deterministic because the media properties ϵ , K_p , and C_f may be evaluated *a priori* from standard tests or from empirical expressions (Dinoy, 1971). Although this term is derived from steady-state concepts it is assumed that it accounts for the damping due to the instantaneous velocity occurring at all phases of the wave cycle. Thus, the linear term dominates during that phase in the cycle when velocities

are low and the turbulent term dominates when velocities are high. The number of unknowns has been reduced from four (q , q_s , q_t , and p) to two (q , p), so a unique solution to a properly posed problem is possible. The assumptions which limit the application of this expression are that convective accelerations be small and that the motion be periodic with frequency low enough to maintain the validity of the damping term. Thus, equation (7) applies when the wavelength is long with respect to wave amplitude and media grain size.

Some linearizing is necessary to find an analytical solution to equation (7). Two approaches are evident. The analyst can perturb the equations to seek successive improvements to the linear solution or seek a linear solution which attempts to incorporate the essential features of the nonlinear problem. This study proceeds with the latter approach because it yields the most information at the first-order level. Furthermore, perturbation schemes predict the existence of higher harmonics due to the nonlinear damping term. Few investigators are properly equipped experimentally to reduce multiple harmonics in partial standing wave trains. This data would be necessary for the verification of the perturbation solution.

f. Linearization Technique. The specific technique to be employed is as follows. The total stress tensor in equation (7) is replaced by an equivalent stress term linear in q , i.e.,

$$\frac{v\epsilon q}{K_p} + \frac{C_f \epsilon^2}{K_p^{1/2}} q |q| + f\sigma q, \quad (8)$$

where σ is the angular frequency of the periodic motion and f is a dimensionless friction or damping coefficient. The coefficient, σ , is introduced to make f dimensionless and for subsequent algebraic expediency. To evaluate f in terms of the known damping law it is required that both the linear and nonlinear friction laws account for the same amount of energy dissipation during one wave cycle. This is commonly referred to as Lorentz's condition of equivalent work (Lorentz, 1926).

The stress tensor in the equation of motion, expressed in either form of equation (8), represents a friction force per unit mass acting at a point in the flow field. If this term is multiplied times the mass flux per unit volume flowing in a direction opposed to the friction force, the resulting quantity is the power dissipated per unit volume. If the power dissipation per unit volume is integrated over the volume of the flow field, V , and the wave period, T , the resulting quantity is the total energy consumed by friction in the volume of interest during one wave period. According to Lorentz's hypothesis, this quantity must be the same for all legitimate damping laws describing the same process. In equation form, this constraint is:

$$\int_V \epsilon dV \int_t^{t+T} f\sigma q \cdot \rho q \, dt = \int_V \epsilon dV \int_t^{t+T} \left\{ \frac{v\epsilon q}{K_p} + \frac{C_f \epsilon^2}{K_p^{1/2}} q |q| \right\} \cdot \rho q \, dt.$$

Thus, a unique relationship exists between the media parameters (ϵ , K_p , C_f), the flow-field parameters (v , q) and the friction coefficient, f . With f assumed spatially independent in V , this relationship is:

$$f = \frac{1}{\sigma} \frac{\int_V \int_t^{t+T} \epsilon^2 \left\{ \frac{vq^2}{K_p} + \frac{C_f \epsilon}{K_p^{1/2}} |q|^3 \right\} dt}{\int_V \int_t^{t+T} \epsilon q^2 dt}, \quad (9)$$

where $q^2 = q \cdot q$, the dot product, and f is considered constant within V . The entire flow field may be divided into any number of subvolumes V , each with its own characteristic f and unique equation of motion.

Substituting the linearized damping term equation (8) into equation (7) yields the linearized equation of motion;

$$S \frac{\partial q}{\partial t} = - \frac{1}{\rho} \nabla (p + \gamma z) - f \sigma q, \quad (10)$$

with

$$\nabla \cdot q = 0.$$

g. Potential Flow Field. The equation of motion is linear in both q and p . As a result, a simple harmonic excitation will yield a simple harmonic solution to the equation. The excitation in this study is assumed to be a monochromatic sea surface consistent with equation (10) to equate the frequency of oscillation within the medium to the frequency of the excitation, σ , so that:

$$q(x,y,z,t), p(x,y,z,t) = \{q(x,y,z), p(x,y,z)\} e^{i\sigma t},$$

and

$$\frac{\partial}{\partial t} \{q,p\} = i\sigma \{q,p\}.$$

Substituting into equation (10) yields:

$$(i\sigma S + f\sigma) q = - \frac{1}{\rho} \nabla (p + \gamma z).$$

Performing the curl operation on this equation demonstrates the irrotationality of the seepage velocity field, i.e.:

$$\sigma(iS + f) \nabla \times q = - \frac{1}{\rho} \nabla \times \nabla (p + \gamma z) = 0.$$

The vector identity $\nabla \times \nabla T = 0$ sets the right-hand side of the equation equal to zero, consequently,

$$\nabla \times \mathbf{q} = 0. \quad (11)$$

The above equation is a statement of zero vorticity or irrotationality and is a sufficient condition to establish the existence of a velocity potential, ϕ , wherein (Robertson, 1965)

$$\mathbf{q} = \nabla \phi. \quad (12)$$

Combining equation (11) with the incompressible condition in equation (10) yields Laplace's equation:

$$\nabla \cdot \mathbf{q} = \nabla \cdot \nabla \phi = \nabla^2 \phi = 0. \quad (13)$$

Equation (13) expresses Laplace's equation for the seepage velocity potential. A similar expression may be derived for the discharge velocity. Again, the medium must be homogeneous with respect to porosity. This may be demonstrated by substituting equation (4) into equation (11):

$$\nabla \times \mathbf{q}_d / \epsilon = 0.$$

Clearly, the discharge velocity is irrotational only if the porosity is constant.

Steady-state damping laws are commonly written in terms of the discharge velocity, e.g., equation (5). Unsteady motions, on the other hand, are characterized by an imbalance in friction and pressure forces causing the flow through the pores to accelerate at the rate of change of the seepage velocity. Thus, the acceleration terms in porous media equations of motion are written in terms of the seepage velocity. As a result, the seepage velocity assumes greater physical significance in unsteady flows and in all cases it represents the actual flow-field kinematics more precisely than the discharge velocity. For these reasons, this study uses the seepage velocity potential to describe the flow field.

It may not be immediately apparent why the friction coefficient, f , behaves like a constant. This may be explained if one recognizes that equation (9) and (10) are not coupled equations. Instead, equation (9) is a constraint which specifies a friction coefficient, f , which is acceptable in equation (10). The friction coefficient is implicitly a function of time and space, as expressed in equation (9). However, once f has been evaluated, it assumes the character of a constant in equation (10). Thus, f may account for variable permeability and nonlinear damping without complicating the form of the solution to the equation of motion.

h. The Bernoulli Equation. Equation (13) represents the irrotational, incompressible character of the seepage flow field. To determine the

particular effect of damping and relate that to the pressure distribution, it is necessary to substitute equation (12) into equation (10) to yield:

$$s \frac{\partial}{\partial t} \nabla \phi = - \frac{1}{\rho} \nabla (p + \gamma z) - f \sigma \nabla \phi.$$

Transposing and removing the gradient operator,

$$\nabla \left\{ s \frac{\partial \phi}{\partial t} + \frac{1}{\rho} (p + \gamma z) + f \sigma \phi \right\} = 0.$$

Since ∇ is a spatial operator, the operand can be a function of time only, and

$$s \frac{\partial \phi}{\partial t} + \frac{1}{\rho} (p + \gamma z) + f \sigma \phi = F(t).$$

Changes in fluid motions occur due to stress gradients. Since $F(t)$ is constant throughout the flow field at any time, t , it has no effect on the stress gradients. Therefore, it may be neglected or included in the definition of ϕ without affecting the solution (Ippen, 1966). Then,

$$s \frac{\partial \phi}{\partial t} + \frac{1}{\rho} (p + \gamma z) + f \sigma \phi = 0. \quad (14)$$

This is the linearized unsteady Bernoulli equation for flow in large-scale granular media with quasi-linear damping. Along with Laplace's equation, it describes the flow and pressure field within the interstices of the granular media. To completely specify the problem, it is necessary to resolve the boundary conditions.

3. Boundary Value Problem.

a. Boundary Conditions. The boundary conditions may be visualized with the aid of the definition in Figure 2. The sketch depicts a periodic flow in an unconfined, coarse-granular media. The vertical displacement of the free surface above the stillwater level (SWL) is specified by η . The vertical coordinate, z , is referenced to the SWL and the impervious horizontal bottom is located at depth h below the SWL.

Capillarity and surface tension are negligible phenomena due to the large scale of the pores in the media of interest. Consequently, the fluid pressure at the free surface is atmospheric pressure. Thus, at $z = \eta$, $p = 0$ and the Bernoulli equation reduces to:

$$s \frac{\partial \phi}{\partial t} + \frac{\gamma}{\rho} \eta + f \sigma \phi = 0.$$

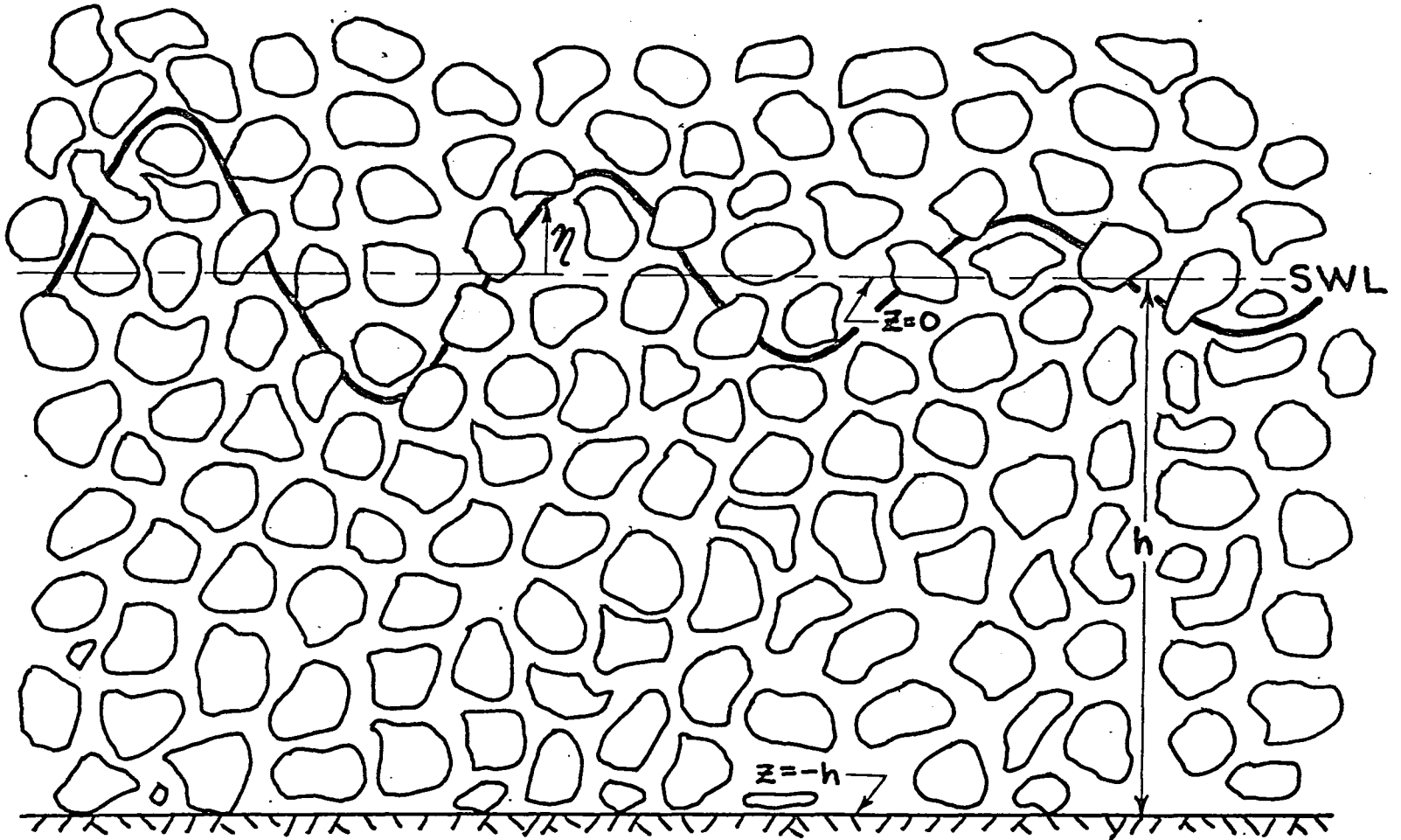


Figure 2. Unconfined periodic flow.

With $\gamma/\rho = g$, the dynamic free-surface condition becomes:

$$\eta = -\frac{1}{g} \left(S \frac{\partial \Phi}{\partial t} + f\sigma\Phi \right)_{z=\eta}.$$

To avoid the difficulties of a transcendental solution it is consistent with small-amplitude waves to apply the surface boundary condition at $z = 0$, thus,

$$\eta = -\frac{1}{g} \left(S \frac{\partial \Phi}{\partial t} + f\sigma\Phi \right)_{z=0}. \quad (15)$$

Equation (15) reduces to a homogeneous boundary condition with the aid of the following observation as shown in Figure 3. The rate at which the water surface rises and falls about the SWL, $d\eta/dt$, is equal to the vertical velocity component in a pore at the free surface. This pore velocity is a seepage velocity and should not be mistaken for a discharge velocity. In equation form this statement reads:

$$\frac{d\eta}{dt} = \frac{\partial \Phi}{\partial z} \Big|_{z=\eta \approx 0}.$$

But,

$$\frac{d\eta}{dt} = \frac{\partial \eta}{\partial t} + \frac{\partial \eta}{\partial x} \frac{dx}{dt}.$$

The convective term is of second order and may be ignored so that:

$$\frac{d\eta}{dt} = \frac{\partial \eta}{\partial t}.$$

and

$$\frac{\partial \eta}{\partial t} = \frac{\partial \Phi}{\partial z} \Big|_{z=0}. \quad (16)$$

Equation (16) is the kinematic free-surface condition and when combined with equation (15) yields:

$$-\frac{1}{g} \left\{ S \frac{\partial^2 \Phi}{\partial t^2} + f\sigma \frac{\partial \Phi}{\partial t} \right\}_{z=0} = \frac{\partial \Phi}{\partial z} \Big|_{z=0},$$

or

$$\left\{ g \frac{\partial \Phi}{\partial z} + f\sigma \frac{\partial \Phi}{\partial t} + S \frac{\partial^2 \Phi}{\partial t^2} \right\}_{z=0} = 0. \quad (17)$$

According to the arguments presented in the development of equation (12), the pressure and velocity fields are expected to have a simple harmonic

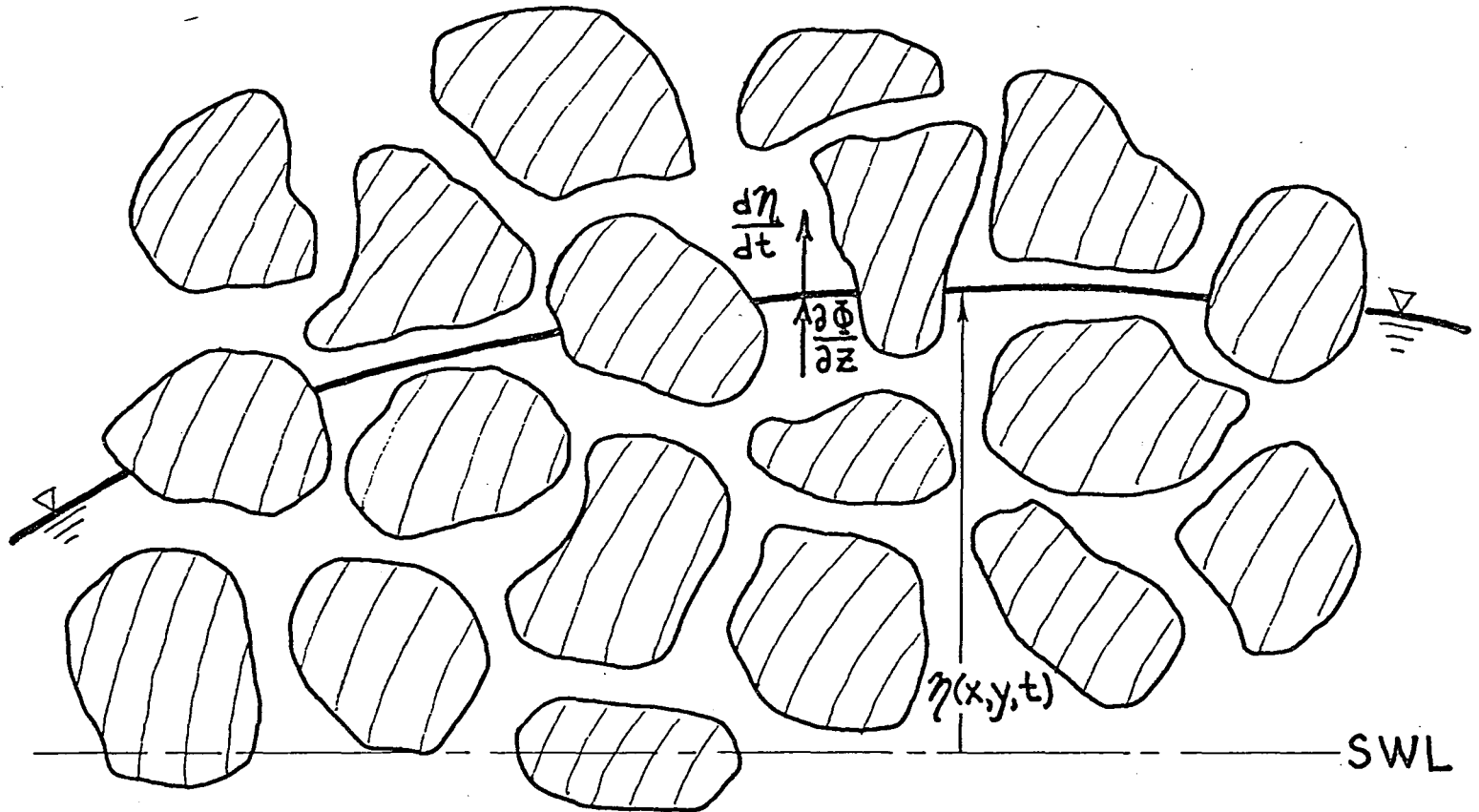


Figure 3. Kinematic free-surface condition.

time dependence. As a result, the velocity potential may be expressed as:

$$\Phi(x,y,z,t) = \phi(x,y,z) \cdot e^{i\sigma t}.$$

Substituting into equation (17) yields the homogeneous free-surface boundary condition:

$$\left\{ g \frac{\partial \phi}{\partial z} + \sigma^2 (if - S) \phi \right\}_{z=0} = 0. \quad (18)$$

Breakwaters are commonly constructed on natural bottoms of very low permeability (sand) or zero permeability (shale, bedrock). It is consistent to regard such a foundation as being impervious. It follows that the vertical velocity component must vanish at $z = -h$, i.e.:

$$\left. \frac{\partial \phi}{\partial z} \right|_{z=-h} = 0. \quad (19)$$

Two independent boundary conditions are sufficient to determine the general form of the solution to a second order partial differential equation. Thus, equations (13), (18), and (19) may be combined to specify the boundary value problem.

Throughout the domain:

$$\nabla^2 \phi = 0, \quad (20)$$

$$z = 0: \quad g \frac{\partial \phi}{\partial z} + \sigma^2 (if - S) \phi = 0, \quad (21)$$

$$z = -h: \quad \frac{\partial \phi}{\partial z} = 0. \quad (22)$$

These are the basic governing equations for damped small-amplitude water waves propagating through a coarse-granular media. Laplace's equation specifies a general irrotational, incompressible flow field while the Bernoulli equation determines the particular effect of damping on the simple harmonic flow.

b. Solution by Separation of Variables. This study seeks a two-dimensional solution to the equations of motion. The longitudinal coordinate is in the direction of wave propagation. Unless the boundary conditions at the sea-breakwater interfaces are written to account for oblique incidence and refraction, direct application of these results is limited to excitation provided by waves of normal or nearly normal incidence.

The homogeneity of the differential equation and the boundary conditions suggests that a variable separation technique will be effective in solving the problem (Robertson, 1965). This may be achieved by replacing the velocity potential with the product of three terms, each of which is a function of only one of the independent variables. Thus,

$$\phi(x, z, t) = X(x) Z(z) T(t),$$

where x is the longitudinal coordinate in a rectangular coordinate system and $T(t)$ is the simple harmonic function, $e^{i\sigma t}$. Laplace's equation may now be written as:

$$\nabla^2 \phi = \frac{\partial^2 \phi}{\partial x^2} + \frac{\partial^2 \phi}{\partial z^2} = X''ZT + XZ''T = 0,$$

or

$$\frac{X''}{X} = -\frac{Z''}{Z}.$$

Since X and Z are independent, the above quotients can only be equal to constants or zero, and two equivalent expressions may be written:

$$\frac{X''}{X} = -K^2,$$

$$\frac{Z''}{Z} = K^2.$$

In the absence of a superimposed current, these equations have the well-known solutions (Robertson, 1965):

$$X = Ae^{iKx} + Be^{-iKx},$$

$$Z = Ce^{Kz} + De^{-Kz}.$$

Applying the bottom boundary condition requires

$$\left. \frac{\partial \phi}{\partial z} \right|_{z=-h} = 0,$$

therefore,

$$\left. \frac{\partial Z}{\partial z} \right|_{z=-h} = 0,$$

$$KCe^{-Kh} - KDe^{Kh} = 0,$$

$$C = De^{2Kh},$$

and

$$Z = D(e^{2Kh + Kz} + e^{-Kz}) = De^{Kh} (e^{K(h+z)} + e^{-K(h+z)}),$$

or

$$Z = 2De^{Kh} \operatorname{ch} K(h+z),$$

where $\operatorname{ch} K(h+z)$ is the hyperbolic cosine of $K(h+z)$. The factor $2De^{Kh}$ may be incorporated into the constants A and B , whence

$$\phi = (Ae^{iKx} + Be^{-iKx}) \operatorname{ch} K(h+z) e^{i\sigma t}, \quad (23)$$

Substituting the above expression into the dynamic free-surface condition yields the constants A and B in terms of the water surface profile,

$$\begin{aligned} \eta &= -\frac{1}{g} (S \frac{\partial \phi}{\partial t} + f\sigma\phi)_{z=0} = -\frac{\sigma}{g} (iS + f) \phi \Big|_{z=0} \\ &= -\frac{\sigma}{g} (iS + f) \operatorname{ch} Kh (Ae^{i(\sigma t + Kx)} + Be^{i(\sigma t - Kx)}). \end{aligned}$$

The x and t dependent factors have been combined to reveal that A represents a waveform propagating in the negative x -direction and B represents a waveform propagating in the positive x -direction. The surface profile, η , may be decomposed into two components with η_1 propagating towards plus infinity and η_2 propagating towards minus infinity. Then the two components may be separated as:

$$\eta_1 = -\frac{\sigma}{g} (iS + f) \operatorname{ch} Kh (Be^{i(\sigma t - Kx)}),$$

and

$$\eta_2 = -\frac{\sigma}{g} (iS + f) \operatorname{ch} Kh (Ae^{i(\sigma t + Kx)}),$$

η_1 attains its maximum, a_1 , when the periodic function $e^{i(\sigma t - Kx)}$ attains its maximum value of unity. Likewise, η_2 attains its maximum, a_2 , when the periodic function $e^{i(\sigma t + Kx)}$ attains its maximum value of unity. Thus,

$$a_1 = -\frac{\sigma}{g} (iS + f) \operatorname{ch} Kh (B),$$

and

$$a_2 = -\frac{\sigma}{g} (iS + f) \operatorname{ch} Kh (A),$$

or

$$B, A = \frac{a_1, a_2}{-\frac{\sigma}{g} (iS + f) \operatorname{ch} Kh},$$

and equation (23) becomes:

$$\Phi = i(a_1 e^{-iKx} + a_2 e^{iKx}) \frac{g}{\sigma(S-if)} \frac{\text{ch } K(h+z)}{\text{ch } Kh} e^{i\sigma t} \quad (24)$$

c. Eigenvalue Problem. Substitution of equation (24) into the combined kinematic and dynamic free-surface condition expressed by equation (21) leads directly to:

$$igK (a_1 e^{-iKx} + a_2 e^{iKx}) \frac{g}{\sigma(S-if)} \frac{\text{sh } Kh}{\text{ch } Kh} e^{i\sigma t} + \sigma^2 (if - S) i (a_1 e^{-iKx} + a_2 e^{iKx}) \frac{g}{\sigma(S-if)} \frac{\text{ch } Kh}{\text{ch } Kh} e^{i\sigma t} = 0,$$

where $\text{sh } Kh$ is the hyperbolic sine of Kh . Transposing and canceling common factors yield:

$$\sigma^2 (S - if) = gK \frac{\text{sh } Kh}{\text{ch } Kh} = gK \text{th } Kh,$$

where $\text{th } Kh$ is the hyperbolic tangent of Kh . This equation specifies acceptable values of K . It is a characteristic equation and has an infinite number of complex roots. Each root may be denoted by a different value of the subscript n so that the equation properly appears as:

$$\sigma^2 (S - if) = gK_n \text{th } K_n h. \quad (25)$$

A boundary value problem consisting of a linear, homogeneous, second order, partial differential equation with two linear, homogeneous boundary conditions is called a Sturm-Liouville problem (Hildebrand, 1965). These problems are also called eigenvalue problems where the solutions to the characteristic equation are the eigenvalues. For each eigenvalue, K_n , there is one eigen function, Φ_n , with its own arbitrary constants a_{1n} , a_{2n} . Each eigen function is a solution to the boundary value problem. The total solution is the sum of all eigen functions. In theory, an infinite number of eigen functions exist, but in practice it is found that only a finite number of eigen functions need be summed to specify a problem to a reasonable degree of accuracy.

Each eigen function may be written:

$$\Phi_n = i(a_{1n} e^{-iK_n x} + a_{2n} e^{iK_n x}) \frac{g}{\sigma(S-if)} \frac{\text{ch } K_n (h+z)}{\text{ch } K_n h} e^{i\sigma t} \quad (26)$$

Alternatively, substituting equation (25) into the above leads to another form for the eigen function:

$$\Phi_n = i(a_{1n} e^{-iK_n x} + a_{2n} e^{iK_n x}) \frac{\sigma}{K_n} \frac{\text{ch } K_n (h+z)}{\text{sh } K_n h} e^{i\sigma t} \quad (27)$$

The total solution to the boundary value problem is:

$$\phi = \sum_{n=1}^{\infty} \phi_n. \quad (28)$$

d. The Dispersion Equation. The behavior of the characteristic equation (25) is worthy of further discussion. In wave propagation problems this equation is often referred to as the dispersion equation because it accounts for the dispersive character of gravity waves, i.e., wave speed is a function of wave frequency. Some insights into the nature of the dispersion equation may be gained by separating the complex eigenvalue, K_n , into real and imaginary parts:

$$K_n = \Gamma_n (1 - i\alpha_n) \quad (29)$$

where α_n may be interpreted as a proportionality factor relating the imaginary to the real part of K_n . Γ symbolizes the real part of a complex wave number. As will be shown, the negative prefix in the imaginary term assures positive solutions to α_n . Substituting equation (29) into equation (25), using the identities:

$$\text{th } \Gamma h (1 - i\alpha) = \frac{\text{th } \Gamma h - \text{th } i\alpha \Gamma h}{1 - \text{th } \Gamma h \text{ th } i\alpha \Gamma h},$$

and

$$\text{th } i\alpha \Gamma h = i \tan \alpha \Gamma h,$$

and equating real and imaginary parts, lead directly to:

$$\frac{S\sigma^2}{g} = \frac{\Gamma}{1 + \text{th}^2 \Gamma h \tan^2 \alpha \Gamma h} \{ \text{th } \Gamma h (1 + \tan^2 \alpha \Gamma h) - \alpha \tan \alpha \Gamma h (1 - \text{th}^2 \Gamma h) \}, \quad (30)$$

and

$$\frac{f\sigma^2}{g} = \frac{\Gamma}{1 + \text{th}^2 \frac{h}{h} \tan^2 \frac{h}{h}} \{ \alpha \text{th } \Gamma h (1 + \tan^2 \alpha \Gamma h) + \tan \alpha \Gamma h (1 - \text{th}^2 \Gamma h) \}, \quad (31)$$

where the subscripts have been dropped from intermediate results to simplify notation. Introducing the identities:

$$1 - \text{th}^2 \Gamma h = \frac{1}{\text{ch}^2 \Gamma h}, \quad 1 + \tan^2 \alpha \Gamma h = \frac{1}{\cos^2 \alpha \Gamma h},$$

$$\sin \alpha \Gamma h \cos \alpha \Gamma h = \frac{1}{2} \sin 2\alpha \Gamma h, \quad \text{sh } \Gamma h \text{ ch } \Gamma h = \frac{1}{2} \text{sh } 2\Gamma h,$$

and regrouping terms in equation (30) yield the result:

$$\frac{S\sigma^2}{g} = \Gamma_n \operatorname{th} \Gamma_n h \frac{1 - \frac{\alpha_n \sin 2\alpha_n \Gamma_n h}{\operatorname{sh} 2\Gamma_n h}}{1 - \frac{\sin^2 \alpha_n \Gamma_n h}{\operatorname{ch}^2 \Gamma_n h}}. \quad (32)$$

Dividing equation (31) by equation (30) and using the above identities lead to the results:

$$\frac{f}{S} = \alpha_n \frac{1 + \frac{\sin 2\alpha_n \Gamma_n h}{\alpha_n \operatorname{sh} 2\Gamma_n h}}{1 - \frac{\alpha_n \sin 2\alpha_n \Gamma_n h}{\operatorname{sh} 2\Gamma_n h}}. \quad (33)$$

Thus, the complex dispersion equation has produced two real equations for the two real unknowns α_n and Γ_n .

An important feature of the dispersion equation pair is the limiting conditions of zero damping, i.e., $f \rightarrow 0$. In this case, with $S = 1.0$, the equations reduce to:

$$\frac{\sigma^2}{g} = \Gamma_1 \operatorname{th} \Gamma_1 h \quad \text{with } \alpha_1 = 0,$$

and

$$\frac{\sigma^2}{g} = -\alpha_n \Gamma_n \tan \alpha_n \Gamma_n h \quad \text{with } \Gamma_n = 0,$$

and

$$\alpha_n \Gamma_n \text{ finite, } n \geq 2.$$

These are simply the linear wave theory dispersion equations. The first one represents the familiar progressive mode while the second one represents the local modes, which are discussed later. It is not surprising that this limiting condition is attained because the theory includes a small-amplitude assumption (negligible convective acceleration), and as the medium takes on the properties of pure seawater, the solution should reduce to linear wave theory.

The roots to the dispersion equation are transcendental; therefore, it is necessary to seek eigenvalues via iteration techniques. To hasten the iteration process, this study has employed a complex Newton-Raphson scheme for rapid convergence (Hildebrand, 1965). The success of this method is dependent on estimating the value of the roots within some unspecified but reasonably close vicinity of the actual solutions. Appendix A provides some useful guidelines for estimating the roots.

Appendix B demonstrates that both positive and negative Γ_n are admissible solutions to the real pair of dispersion equations but the α_n roots are always positive. The importance of this trait becomes evident when the surface profile and wave celerity are analyzed in the following discussions.

e. The Surface Profile. Equations (15), (26), and (29) may be combined to yield the surface profile for a single eigenvalue component:

$$\begin{aligned} \eta_n &= -\frac{\sigma}{g} (iS + f) \phi_n \Big|_{z=0} \\ &= (a_{1n} e^{-iK_n x} + a_{2n} e^{iK_n x}) e^{i\sigma t} \\ &= a_{1n} e^{-\alpha_n \Gamma_n x} e^{i(\sigma t - \Gamma_n x)} + a_{2n} e^{\alpha_n \Gamma_n x} e^{i(\sigma t + \Gamma_n x)}. \end{aligned} \quad (34)$$

This equation depicts each wave component as an exponentially damped sinusoid, decaying in the direction of propagation. Note that including negative values of Γ_n simply interchanges a_{1n} and a_{2n} without altering the problem solution.

It is apparent from the form of the exponentials that Γ_n specifies the spatial periodicity of the function and $\alpha_n \Gamma_n$ specifies the amplitude decay. Consequently, K_n is simply a complex wave number with real and imaginary parts which characterize wavelength and decay distance, respectively.

f. Celerity. The concept of phase velocity or wave celerity is easy to visualize with the expression for the surface profile, equation (34). The phase velocity, C_n , may be interpreted as the rate at which zero crossings propagate in the x, t plane. This is simply the rate at which one must move in x to compensate for a temporal change in t such that the periodic term in equation (34) remains constant. That is:

$$C_n \frac{\partial}{\partial x} e^{i(\sigma t \mp \Gamma_n x)} + \frac{\partial}{\partial t} e^{i(\sigma t \mp \Gamma_n x)} = 0,$$

or

$$C_n = \pm \frac{\sigma}{\Gamma_n}, \quad (35)$$

where the positive sign applies to wave propagation in the positive x -direction, etc. Thus, it is the real part of the wave number, Γ_n , which specifies the propagation rate and it is the imaginary part, $\alpha_n \Gamma_n$, which specifies the decay rate.

g. Depth Dependence. It is useful to substitute equation (29) into equation (27) and look at the form of the velocity potential for a single

eigenvalue propagating in the positive x-direction. With the subscripts omitted to simplify notation, the velocity potential appears as:

$$\phi_n \Big|_{+x} = \frac{i\sigma a_1 e^{-\alpha \Gamma x}}{\Gamma(1 - i\alpha)} \frac{\text{ch } \Gamma(h+z) \cos \alpha \Gamma(h+z) - i \text{sh } \Gamma(h+z) \sin \alpha \Gamma(z+h)}{\text{sh } \Gamma h \cos \alpha \Gamma h - i \text{ch } \Gamma h \sin \alpha \Gamma h} e^{i(\sigma t - \Gamma x)}.$$

This equation contains five complex terms including a_1 , which in general contains the phase as well as the magnitude of the amplitude and is therefore complex. When these terms are expanded and separated they yield 16 real and 16 imaginary terms. Complex notation consolidates 32 terms to a single expression and greatly simplifies subsequent algebraic manipulations. The interesting feature in this equation is the depth-dependent term. In linear wave theory, the depth dependence decays hyperbolically. The above equation shows that with damping, the depth dependence is a summation of four terms, each of which is a trigonometrically modulated hyperbolic decay term. Thus, for large α , the horizontal velocity includes four terms, each of which exhibits a depth dependence (Fig. 4). As the damping properties of the medium go to zero, the velocity potential reduces to that given by linear wave theory.

4. Vertical-Wall Breakwaters.

a. Physical Description. The two-dimensional velocity potential described by equations (26), (27), and (28) applies to media of finite depth and arbitrary longitudinal extent. To specify the potential for a breakwater of finite width, b , consider a crib-style breakwater, located in a monochromatic sea environment (Fig. 5). As an incident wave encounters the breakwater face, part of the wave is reflected back out to sea while some of the wave energy is transmitted to the interior of the breakwater. This transmitted energy excites the appropriate eigen modes which in turn propagate and decay toward the lee face of the breakwater. At the lee face each mode experiences partial transmission out of the breakwater where the energy excites the proper modes in the transmitted wave train. Likewise, a part of each mode is reflected back to the interior and each modal component continues to decay as it propagates towards the front face of the breakwater. Again, at the front face, each modal component experiences partial reflection back to the interior and partial transmission. The energy transmitted to the windward side of the breakwater contributes to each mode in the reflected wave train. This process continues *ad infinitum* as the components which are propagating back and forth within the breakwater become smaller and smaller with each traverse due to exponential damping and partial transmission at each face.

The effect of a continuous incident wave train is to continuously excite new components of each mode as old components decay away. A quasi-steady-state situation is reached so that there is no net accumulation of energy within the breakwater. Then all components of each eigen mode propagating in one direction may be superimposed to yield a single component for each mode. This superposition principle applies equally well to the reflected and transmitted wave trains. The net result

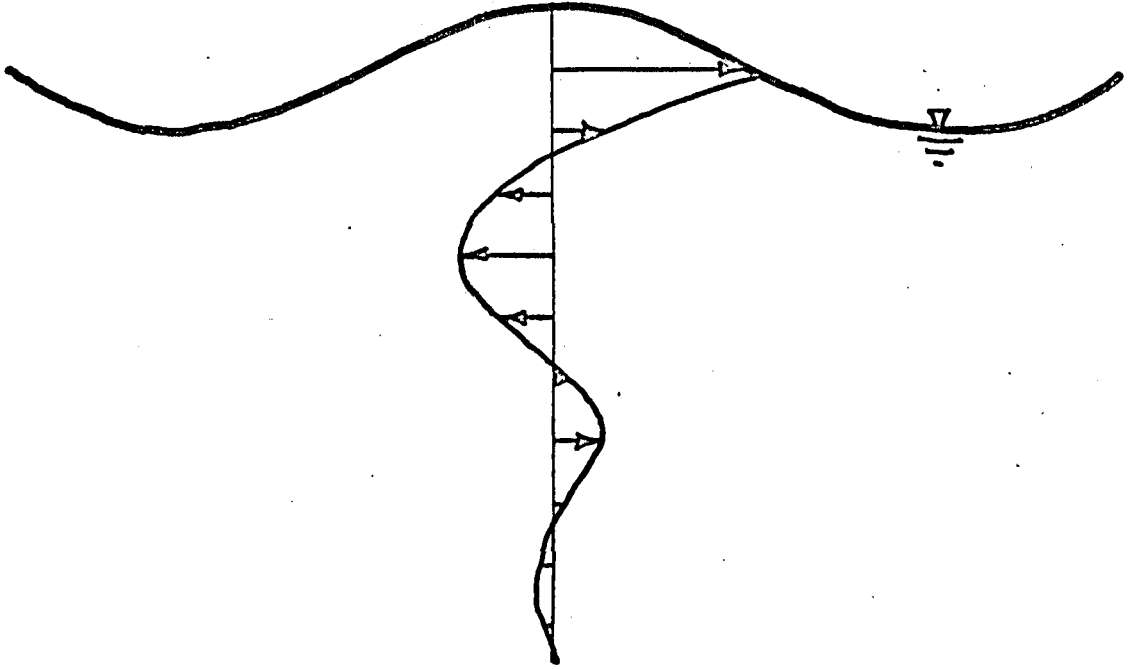


Figure 4. One term in the horizontal velocity distribution.

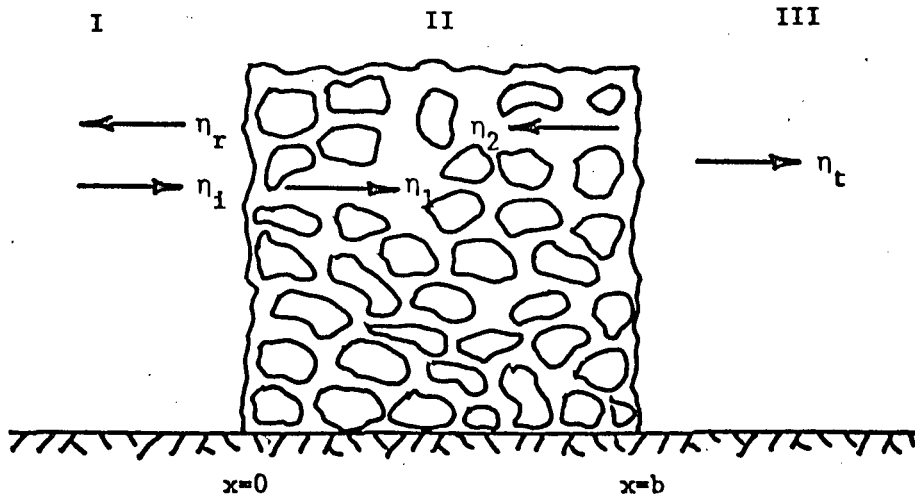


Figure 5. Crib-style breakwater.

of placing a permeable breakwater in a monochromatic wave train of constant wave height is to produce n modes in each of the following: a reflected wave train, a transmitted wave train, and two wave trains propagating in opposite directions in the interior of the breakwater. Since each mode propagates with some unknown amplitude, there are, in general, $4n$ unknowns and $4n$ boundary conditions needed to solve the problem.

b. Flow-Field Specification. The velocity potential defined by equation (27) applies to region II in Figure 5. It is worthwhile to redefine the phase references. The amplitude of waves propagating in the positive x -direction are maximum at $x = 0$; waves propagating in the negative x -direction have maximum amplitudes at $x = b$. Accordingly, a_{1n} and a_{2n} should be referenced to $x = 0$ and $x = b$, respectively. This alters the form of the velocity potential in equation (27) to:

$$\phi_n = i(a_{1n} e^{-iK_n x} + a_{2n} e^{iK_n (x-b)}) \frac{\sigma}{K_n} \frac{\text{ch } K_n (h+z)}{\text{sh } K_n h} e^{i\sigma t} . \quad (36)$$

The total velocity potential in region II is the sum of the eigen functions, that is:

$$\Phi_{II} = \sum_{n=1}^{\infty} \phi_n .$$

The pressure field is given by equation (1),

$$\frac{p_{II}}{\rho} = -\sigma (iS + f) \Phi_{II} - gz .$$

Linear wave theory applies in regions I and III. As revealed earlier in the derivation, the expressions for the velocity potential and dispersion equation in the granular media reduce to linear wave theory for the limiting condition of $S = 1.0$, $f = 0$. However, it is necessary to properly account for the phase and direction of the separate wave trains in each zone.

With $S = 1.0$ and $f = 0$, the dispersion equation reduces to:

$$\sigma^2 = gk_n \text{th } k_n h , \quad (37)$$

where the lower case wave number refers to the regions exterior to the breakwater. The $n = 1$ mode is a real wave number and represents a progressive wave which propagates without decaying. The $n \geq 2$ modes have imaginary wave numbers and represent local standing waves with spatially decaying amplitudes. The local modes are included to satisfy irregularities at the boundaries between two regions, but have no effect far away from the boundaries.

There is, in general, one real solution to equation (37). This is easily found using the Newton-Raphson method with any initial, real estimate to k_1 . The function is odd so that either the negative or positive roots will satisfy the equation. The sign of the root is chosen to correspond to the proper direction of propagation. The imaginary roots are easy to locate by rewriting equation (37) as:

$$\frac{\sigma^2 h}{g} = k_n h \tanh k_n h,$$

$$k_n = -i k'_n,$$

$$\frac{\sigma^2 h}{g} = -k'_n h \tan k'_n h.$$

Now k'_n is real for $n \geq 2$. Solutions to this equation will be found near:

$$k'_n h \sim (n-1) \pi$$

The behavior of the local modes is apparent from the form of the velocity potential, equation (27), which applies exterior to the breakwater if the complex wave number, K_n , is replaced with k_n . This leads to the result:

$$\phi_n = i (a_{1n} e^{-ik_n x} + a_{2n} e^{ik_n x}) \frac{\sigma}{k_n} \frac{\operatorname{ch} k_n (h+z)}{\operatorname{sh} k_n h} e^{i\sigma t}.$$

But $k_n = -ik'_n$, $n \geq 2$, then,

$$\phi_n \Big|_{n \geq 2} = -i (a_{1n} e^{-k'_n x} + a_{2n} e^{k'_n x}) \frac{\sigma}{k'_n} \frac{\cos k'_n (h+z)}{\sin k'_n h} e^{i\sigma t}.$$

Since k'_n is real and positive, the x -dependent expressions show that the local modes decay exponentially in the direction of propagation of the progressive mode. Thus, the local modes in the reflected and transmitted wave trains decay with increasing distance from the boundaries.

In region I (Fig. 5), the total velocity potential is the sum of the incident and reflected wave potentials,

$$\phi_I = \phi_i + \phi_r.$$

The incident wave train is the known forcing function in the problem and has been specified as a monochromatic sea surface. Consequently, only the progressive mode is present, the amplitude is known, and the incident wave velocity potential is:

$$\phi_i = i a_i e^{-ik_1 x} \frac{\sigma}{k_1} \frac{\text{ch } k_1 (h+z)}{\text{sh } k_1 h} e^{i\sigma t}.$$

The reflected wave train, on the other hand, must include all modes to account for local disturbances at the sea-breakwater interface. Thus,

$$\phi_r = \sum_{n=1}^{\infty} \phi_{rn},$$

$$\phi_{rn} = i a_{rn} e^{ik_n x} \frac{\sigma}{k_n} \frac{\text{ch } k_n (h+z)}{\text{sh } k_n h} e^{i\sigma t},$$

where the a_{rn} are reflected wave amplitudes of unknown magnitude and phase. Note that the phase of the oscillations in region I has been referenced to the windward breakwater face, $x = 0$. The pressure field falls directly out of equation (14) with $S = 1.0$, $f = 0$,

$$\frac{p_I}{\rho} = -i\sigma\phi_I - gz.$$

In region III the velocity potential is simply that represented by the transmitted wave train,

$$\phi_{III} = \phi_t.$$

The transmitted wave train is composed of a progressive mode and an infinite series of local modes,

$$\phi_t = \sum_{n=1}^{\infty} \phi_{tn}.$$

The phase of the oscillations is referenced to the leeward breakwater face, $x = b$, and therefore appear as:

$$\phi_{tn} = i a_{tn} e^{-ik_n (x-b)} \frac{\sigma}{k_n} \frac{\text{ch } k_n (h+z)}{\text{sh } k_n h} e^{i\sigma t}.$$

As in region I, the pressure field is:

$$\frac{p_{III}}{\rho} = -i\sigma\phi_{III} - gz.$$

c. Interfacial Boundary Conditions. These results conclude the specification of the velocity and pressure fields in each of the three regions of interest. Although the structure of the expressions describing these fields has been determined, each expression contains unknown

amplitudes which remain to be evaluated. Before proceeding with this evaluation, it is useful to summarize the solution in each region.

Region I:

$$\begin{aligned}\phi_I &= \phi_i + \sum_{n=1}^{\infty} \phi_{rn}, \\ \phi_i &= i a_i e^{-ik_1 x} \frac{\sigma}{k_1} \frac{\text{ch } k_1 (h+z)}{\text{sh } k_1 h} e^{i\sigma t}, \\ \phi_{rn} &= i a_{rn} e^{ik_n x} \frac{\sigma}{k_n} \frac{\text{ch } k_n (h+z)}{\text{sh } k_n h} e^{i\sigma t}, \\ \frac{P_I}{\rho} &= -i\sigma\phi_I - gz, \\ \sigma^2 &= gk_n \text{th } k_n h\end{aligned}\quad (38)$$

Region II:

$$\begin{aligned}\phi_{II} &= \sum_{n=1}^{\infty} \phi_n, \\ \phi_n &= i(a_{1n} e^{-iK_n x} + a_{2n} e^{iK_n (x-b)}) \frac{\sigma}{K_n} \frac{\text{ch } K_n (h+z)}{\text{sh } k_n h} e^{i\sigma t}, \\ \frac{P_{II}}{\rho} &= -(iS + f) \phi_{II} - gz, \\ \sigma^2 (S - if) &= gK_n \text{th } K_n h.\end{aligned}\quad (39)$$

Region III:

$$\begin{aligned}\phi_{III} &= \sum_{n=1}^{\infty} \phi_{tn}, \\ \phi_{tn} &= i a_{tn} e^{-ik_n (x-b)} \frac{\sigma}{k_n} \frac{\text{ch } k_n (h+z)}{\text{sh } k_n h} e^{i\sigma t}, \\ \frac{P_{III}}{\rho} &= -i\sigma\phi_{III} - gz, \\ \sigma^2 &= gk_n \text{th } k_n h.\end{aligned}\quad (40)$$

These equations contain $4n$ unknowns, i.e., n unknowns for each of the amplitude series a_{rn} , a_{ln} , a_{2n} , and a_{tn} . To evaluate these unknowns, $4n$ additional boundary conditions are needed. Since the solutions in adjacent regions must be continuous at the interface between regions, it is apparent that the appropriate boundary conditions are continuity of pressure and horizontal mass flux at $x = 0$ and $x = b$. If these conditions are applied at n points along each interface, then there will be sufficient equations to specify the unknown amplitudes.

At the sea-breakwater interface, the flow must contract or expand as it enters or exits a particular pore. Incompressible flow mass conservation requires that a constriction in the flow field be accompanied by an acceleration such that the product of the velocity and the projected flow area remain constant. Thus, at $x = 0$:

$$u_I dA_I = u_{II} dA_{II},$$

or

$$u_I = u_{II} \frac{dA_{II}}{dA_I} = u_{II} \epsilon.$$

Although the porosity, ϵ , is defined as the ratio of pore volume to total volume, it is also equal to the average ratio of cross-sectional pore area to total area. Similarly, at $x = b$:

$$u_{II} \epsilon = u_{III}.$$

Note that continuity of horizontal mass flux is equivalent to continuity of the discharge velocity. The interfacial boundary condition may now be written as:

$$\underline{x = 0} \quad u_I = \epsilon u_{II},$$

$$P_I = P_{II}.$$

$$\underline{x = b} \quad \epsilon u_{II} = u_{III},$$

$$P_{II} = P_{III}.$$

But $u = \partial\phi/\partial x$, and the pressure terms are elementary functions of the velocity potential, as summarized in equations (38), (39), and (40). Consequently, the interfacial boundary conditions become:

$$\underline{x = 0} \quad \frac{\partial\phi_I}{\partial x} = \epsilon \frac{\partial\phi_{II}}{\partial x}, \quad (41)$$

$$\phi_I = (S - 1f) \phi_{II}. \quad (42)$$

$$\underline{x = b} \quad \varepsilon \frac{\partial \phi_{II}}{\partial x} = \frac{\partial \phi_{III}}{\partial x}, \quad (43)$$

$$(S - if) \phi_{II} = \phi_{III}. \quad (44)$$

Substituting the velocity potentials from equations (38), (39), and (40) into equations (41) to (44) lead directly to:

$$\begin{aligned} & \sum_{n=1}^{\infty} \frac{\text{ch } k_n (h + z)}{\text{sh } k_n h} a_{rn} + \sum_{n=1}^{\infty} \varepsilon \frac{\text{ch } K_n (h + z)}{\text{sh } K_n h} (a_{1n} - a_{2n} e^{-iK_n b}) \\ &= \frac{\text{ch } k_1 (h + z)}{\text{sh } k_1 h} a_i. \end{aligned} \quad (45)$$

$$\begin{aligned} & - \sum_{n=1}^{\infty} \frac{1}{k_n} \frac{\text{ch } k_n (h + z)}{\text{sh } k_n h} a_{rn} \\ & + (S - if) \sum_{n=1}^{\infty} \frac{1}{K_n} \frac{\text{ch } K_n (h + z)}{\text{sh } K_n h} (a_{1n} + a_{2n} e^{-iK_n b}) \\ &= \frac{1}{k_1} \frac{\text{ch } k_1 (h + z)}{\text{sh } k_1 h} a_i. \end{aligned} \quad (46)$$

$$\sum_{n=1}^{\infty} \varepsilon \frac{\text{ch } K_n (h + z)}{\text{sh } K_n h} (a_{2n} - a_{1n} e^{-iK_n b}) + \sum_{n=1}^{\infty} \frac{\text{ch } k_n (h + z)}{\text{sh } k_n h} a_{tn} = 0. \quad (47)$$

$$\begin{aligned} & (S - if) \sum_{n=1}^{\infty} \frac{1}{K_n} \frac{\text{ch } K_n (h + z)}{\text{sh } K_n h} (a_{1n} e^{-iK_n b} + a_{2n}) \\ & - \sum_{n=1}^{\infty} \frac{1}{k_n} \frac{\text{ch } k_n (h + z)}{\text{sh } k_n h} a_{tn} = 0. \end{aligned} \quad (48)$$

In the limit, these four equations must be satisfied at all z if one is to solve for the amplitudes of an infinite number of eigen functions. This will be shown to be unnecessary, as satisfactory results may be found for a finite upper limit on n . Therefore, each equation must be satisfied at n different depths, z , to obtain a solution. Solutions typically converge for n less than 10. Consequently, the

problem reduces to solving a $4n$ by $4n$ complex matrix for $4n$ complex amplitudes. Packaged subroutines such as SIMQ (International Business Machines, 1968) which will solve large complex matrix problems very efficiently.

d. Orthogonality. Although it is possible to proceed directly with a solution to this large matrix, considerable simplification may be gained by using the orthogonal properties of the eigen functions. The z -dependent terms are orthogonal because they are solutions to a linear second-order homogeneous differential equation with linear first-order homogeneous boundary conditions (Hildebrand, 1965). Orthogonality is the characteristic that the integral of the product of two eigen functions vanishes over the interval specified for the boundary conditions, that is,

$$\int_{-h}^0 \phi_m \phi_n dz = 0, m \neq n$$

This property may be used to eliminate the depth dependence and reduce the order of the matrix problem. To accomplish this, multiply equations (45) to (48) through by $\text{ch } K_m(h+z)$ and integrate over the full depth. The following identities are useful:

$$\int_{-h}^0 \text{ch } K_m(h+z) \text{ch } K_n(h+z) dz = 0, m \neq n$$

$$= \frac{\text{sh } K_m h \text{ch } K_m h + K_m h}{2K_m}, n = m,$$

$$\int_{-h}^0 \text{ch } K_m(h+z) \text{ch } k_n(h+z) dz = \frac{\sigma^2 \text{ch } K_m h \text{ch } k_n h}{g (K_m^2 - k_n^2)} (S-if-1).$$

If the porosity is constant throughout the full depth, then the above operations may be performed on equations (45) to (48) to yield:

$$\sum_{n=1}^{\infty} \frac{a_{rn}}{\text{sh } k_n h} \frac{\sigma^2 \text{ch } K_m h \text{ch } k_n h}{g (K_m^2 - k_n^2)} (S-if-1)$$

$$+ \epsilon \frac{(a_{1m} - a_{2m} e^{-iK_m b})}{\text{sh } K_m h} \frac{(\text{sh } K_m h \text{ch } K_m h + K_m h)}{2K_m}$$

$$= \frac{a_i}{\text{sh } k_1 h} \frac{\sigma^2 \text{ch } K_m h \text{ch } k_1 h}{g (K_m^2 - k_1^2)} (S-if-1). \quad (49)$$

$$\begin{aligned}
& - \sum_{n=1}^{\infty} \frac{a_{rn}}{k_n \operatorname{sh} k_n h} \frac{\sigma^2}{g} \frac{\operatorname{ch} K_m h \operatorname{ch} k_n h}{K_m^2 - k_n^2} (S-if-1) \\
& + (S-if) \frac{(a_{1m} + a_{2m} e^{-iK_m b}) (\operatorname{sh} K_m h \operatorname{ch} K_m h + K_m h)}{k_1 \operatorname{sh} k_1 h} \frac{1}{2K_m} \\
& = \frac{a_i}{k_1 \operatorname{sh} k_1 h} \frac{\sigma^2}{g} \frac{\operatorname{ch} K_m h \operatorname{ch} k_1 h}{K_m^2 - k_1^2} (S-if-1). \tag{50}
\end{aligned}$$

$$\begin{aligned}
& \varepsilon \frac{(a_{2m} - a_{1m} e^{-iK_m b}) (\operatorname{sh} K_m h \operatorname{ch} K_m h + K_m h)}{\operatorname{sh} K_m h} \frac{1}{2K_m} \\
& + \sum_{n=1}^{\infty} \frac{a_{tn}}{\operatorname{sh} k_n h} \frac{\sigma^2}{g} \frac{\operatorname{ch} K_m h \operatorname{ch} k_n h}{K_m^2 - k_n^2} (S-if-1) = 0. \tag{51}
\end{aligned}$$

$$\begin{aligned}
& (S-if) \frac{(a_{1m} e^{-iK_m b} + a_{2m}) (\operatorname{sh} K_m h \operatorname{ch} K_m h + K_m h)}{K_1 K_m \operatorname{sh} K_m h} \frac{1}{2K_m} \\
& - \sum_{n=1}^{\infty} \frac{a_{tn}}{k_n \operatorname{sh} k_n h} \frac{\sigma^2}{g} \frac{\operatorname{ch} K_m h \operatorname{ch} k_n h}{K_m^2 - k_n^2} (S-if-1) = 0. \tag{52}
\end{aligned}$$

Substitute

$$a_i \frac{\sigma^2}{g} \frac{\operatorname{ch} k_n h}{\operatorname{sh} k_n h} = k_n,$$

into each of the above, divide through by

$$\frac{(S-if-1)K_1}{K_m^2 - K_1^2} \operatorname{ch} K_m h,$$

and introduce the following notation for the dimensionless amplitudes:

$$C_{rn}, C_{1n}, C_{2n}, C_{tn} = \frac{a_{rn}}{a_i}, \frac{a_{1n}}{a_i}, \frac{a_{2n}}{a_i}, \frac{a_{tn}}{a_i}. \tag{53}$$

These steps lead directly to the result:

$$\sum_{n=1}^{\infty} C_{rn} \frac{k_n}{k_1} \frac{K_m^2 - k_1^2}{K_m^2 - k_n^2} + \frac{\epsilon}{(S-if-1)} (C_{1m} - C_{2m} e^{-iK_m b})$$

$$\frac{(K_m^2 - k_1^2)}{2k_1 K_m} \left(1 + \frac{K_m h}{\text{sh } K_m h \text{ ch } K_m h}\right) = 1.0. \quad (54)$$

$$-\sum_{n=1}^{\infty} C_{rn} \frac{(K_m^2 - k_1^2)}{(K_m^2 - k_n^2)} + \frac{(S-if)}{(S-if-1)} (C_{1m} + C_{2m} e^{-iK_m b})$$

$$\frac{(K_m^2 - k_1^2)}{2K_m^2} \left(1 + \frac{K_m h}{\text{sh } K_m h \text{ ch } K_m h}\right) = 1.0. \quad (55)$$

$$\frac{\epsilon}{(S-if-1)} (C_{2m} - C_{1m} e^{-iK_m b}) \frac{(K_m^2 - k_1^2)}{2k_1 K_m} \left(1 + \frac{K_m h}{\text{sh } K_m h \text{ ch } K_m h}\right)$$

$$+ \sum_{n=1}^{\infty} C_{tn} \frac{k_n}{k_1} \frac{K_m^2 - k_1^2}{K_m^2 - k_n^2} = 0. \quad (56)$$

$$\frac{S-if}{S-if-1} (C_{1m} e^{-iK_m b} + C_{2m}) \frac{K_m^2 - k_1^2}{2K_m^2} \left(1 + \frac{K_m h}{\text{sh } K_m h \text{ ch } K_m h}\right)$$

$$- \sum_{n=1}^{\infty} C_{tn} \frac{K_m^2 - k_1^2}{K_m^2 - k_n^2} = 0. \quad (57)$$

This form of the equations reveals that the condition of orthogonality permits the extraction of one mode from the series solution in region II, (C_{1m} , C_{2m}) in terms of the full series in regions I and III

$$\left(\sum_n C_{rn}, C_{tn}\right).$$

Then, using standard algebraic methods for solutions to simultaneous equations, C_{1m} and C_{2m} may be eliminated from any two of the four equations to isolate C_{rn} , C_{tn} series as:

$$\sum_{n=1}^{\infty} C_{rn} \frac{K_m^2 - k_1^2}{K_m^2 - k_n^2} \left(\frac{k_n}{k_1} + \frac{\epsilon}{S-if} \frac{K_m}{k_1} \right) + e^{-iK_m b}$$

$$\sum_{n=1}^{\infty} C_{tn} \frac{K_m^2 - k_1^2}{K_m^2 - k_n^2} \left(\frac{k_n}{k_1} - \frac{\epsilon}{S-if} \frac{K_m}{k_1} \right) = 1.0 - \frac{\epsilon}{S-if} \frac{K_m}{k_1}. \quad (58)$$

$$\sum_{n=1}^{\infty} C_{rn} \frac{K_m^2 - k_1^2}{K_m^2 - k_n^2} \left(\frac{k_n}{k_1} - \frac{\epsilon}{S-if} \frac{K_m}{k_1} \right) + e^{iK_m b}$$

$$\sum_{n=1}^{\infty} C_{tn} \frac{K_m^2 - k_1^2}{K_m^2 - k_n^2} \left(\frac{k_n}{k_1} + \frac{\epsilon}{S-if} \frac{K_m}{k_1} \right) = 1.0 + \frac{\epsilon}{S-if} \frac{K_m}{k_1}. \quad (59)$$

The remaining two equations yield C_{1m} and C_{2m} as functions of the C_{rn} , C_{tn} series:

$$C_{1m} = \frac{S-if-1}{\epsilon} \frac{k_1 K_m}{K_m^2 - k_1^2} \frac{\text{sh } K_m h \text{ ch } K_m h}{\text{sh } K_m h \text{ ch } K_m h + K_m h}$$

$$\left\{ 1.0 + \frac{\epsilon}{S-if} \frac{K_m}{k_1} - \sum_{n=1}^{\infty} C_{rn} \frac{K_m^2 - k_1^2}{K_m^2 - k_n^2} \left(\frac{k_n}{k_1} - \frac{\epsilon}{S-if} \frac{K_m}{k_1} \right) \right\}. \quad (60)$$

$$C_{2m} = \frac{S-if-1}{\epsilon} \frac{k_1 K_m}{K_m^2 - k_1^2} \frac{s \text{ sh } K_m h \text{ ch } K_m h}{\text{sh } K_m h \text{ ch } K_m h + K_m h}$$

$$\left\{ - \sum_{n=1}^{\infty} C_{tn} \frac{K_m^2 - k_1^2}{K_m^2 - k_n^2} \left(\frac{k_n}{k_1} - \frac{\epsilon}{S-if} \frac{K_m}{k_1} \right) \right\}. \quad (61)$$

Equations (58) to (61) represent a significant simplification with respect to the original form of equations (45) to (48). Specifically, the reflected and transmitted components may be solved from equations (58) and (59) independent of the components inside the breakwater. However, the latter two components will be necessary for the application of Lorentz's (1926) condition of equivalent work. They may be solved directly from equations (60) and (61) in terms of the previously determined C_{rn} , C_{tn} . Thus, a $4n$ by $4n$ matrix has been reduced to a $2n$ by $2n$ matrix plus two linear vector equations. This condensation represents a considerable saving in the computation effort.

The actual computation requires that a $2n$ by $2n$ matrix be formed by rewriting equations (58) and (59) n times for n different values of K_m . This matrix is solved using a method such as SIMQ and yields the reflection and transmission coefficient series C_{rn} and C_{tn} , respectively. Then the two dimensionless amplitude series inside the breakwater, C_{1n} and C_{2n} , are solved by direct substitution of C_{rn} and C_{tn} into equations (60) and (61), respectively.

It is apparent from the terms appearing in these last four equations that the solution ultimately depends on: (a) the structural properties of the breakwater width and depth, b and h ; (b) the media properties of porosity and damping, ϵ and f ; and (c) the wave properties as described by the wave numbers inside and outside the breakwater, K_n and k_n . However, the dispersion equation (37) establishes the dependence of k_n for $n > 1$ on k_1 and h as:

$$\frac{\sigma^2 h}{g} = k_1 h \text{ th } k_1 h = k_n h \text{ th } k_n h.$$

Thus, given k_1 and h , all other k_n 's may be found. Likewise, the dispersion equation inside the breakwater, equation (25), establishes the dependence of K_n on k_1 , h and f as:

$$\frac{\sigma^2 h}{g} (S-if) = K_n h \text{ th } K_n h = k_1 h \text{ th } k_1 h (S-if).$$

Therefore, k_1 along with h and f completely specify all of the wave numbers k_n and K_n . Then the independent parameters are h , b , ϵ , f , and k_1 . Nondimensionalizing h , b , and k_1 reduces the number of parameters by one to the dimensionless form b/h , ϵ , f , and $k_1 h$.

A detailed discussion of the solution behavior is discussed later. Presently, the very important condition of long-wave excitation is considered. The relatively simple form of the resulting solution will reveal the general character of the breakwater response.

e. The Long-Wave Problem. The long-wave problem is characterized by a wavelength which exceeds the water depth by a factor of 20, so that:

$$k_1 h \approx 0.3,$$

$$K_1 h \approx 0.3 (1 - i).$$

For this limiting condition, the value of the hyperbolic tangent in the dispersion equation is suitably described by the value of the argument itself, that is:

$$\frac{\sigma^2 h}{g} = k_n h \operatorname{th} k_n h \approx (k_n h)^2,$$

and

$$\frac{\sigma^2 h}{g} (S - if) = K_n h \operatorname{th} K_n h \approx (K_n h)^2.$$

Each equation has two roots of equal magnitude but opposite sign. The sign is chosen to correspond to the direction of propagation so that in actuality only one mode specifies the complete solution to the long-wave problem. This result should be anticipated. A fundamental characteristic of long waves is that the horizontal velocity and dynamic pressure components are independent of depth. Thus, if the boundary conditions are satisfied at one point in a vertical plane, they are satisfied at all points. Consequently, the absence of local irregularities at the interface between two solution domains precludes the existence of multiple modes both physically and mathematically.

With the upper limit on n being equal to unity, the subscript may be dropped from the long-wave solution, and the dispersion equations become:

$$\begin{aligned} k^2 h^2 &= \frac{\sigma^2 h}{g}, \\ K^2 h^2 &= \frac{\sigma^2 h}{g} (S - if). \end{aligned} \quad (62)$$

Substituting $Kh = \Gamma h(1 - i\alpha)$ into equation (62) and separating real and imaginary parts yield:

$$\Gamma^2 h^2 = \frac{1}{2} \frac{\sigma^2 h}{g} S (1 + \sqrt{1 + f^2/S^2}),$$

and

$$\alpha = \frac{\sqrt{1 + f^2/S^2} - 1}{f/S}. \quad (63)$$

Note that the effect of the damping coefficient, f , is to increase the long-wave number inside the breakwater relative to its value outside. This causes the wavelength to shorten, a result which is anticipated. In general, friction inhibits wave propagation; therefore, the celerity and wavelength should be decreased as indicated by equation (63).

Two other identities are useful for the long-wave solution:

$$\text{sh } Kh \sim Kh,$$

$$\text{ch } Kh \sim 1.0.$$

Introducing the above into equations (58) to (61) leads to the result:

$$C_r \left(1 + \frac{\epsilon}{S-if} \frac{K}{k}\right) + e^{-iKb} C_t \left(1 - \frac{\epsilon}{S-if} \frac{K}{k}\right) = 1 - \frac{\epsilon}{S-if} \frac{K}{k},$$

$$C_r \left(1 - \frac{\epsilon}{S-if} \frac{K}{k}\right) + e^{iKb} C_t \left(1 + \frac{\epsilon}{S-if} \frac{K}{k}\right) = 1 + \frac{\epsilon}{S-if} \frac{K}{k},$$

$$C_1 = \frac{S-if-1}{\epsilon} \frac{kK}{K^2-k^2} \frac{1}{2} \left\{1.0 + \frac{\epsilon}{S-if} \frac{K}{k} - C_r \left(1 - \frac{\epsilon}{S-if} \frac{K}{k}\right)\right\},$$

$$C_2 = -\frac{S-if-1}{\epsilon} \frac{kK}{K^2-k^2} \frac{1}{2} C_t \left(1 - \frac{\epsilon}{S-if} \frac{K}{k}\right).$$

Solving these four equations simultaneously produces expressions for the four unknown wave components:

$$C_r = \frac{\left(1 - \frac{\epsilon^2 k^2}{K^2}\right) (e^{iKb} - e^{-iKb})}{\left(1 + \frac{\epsilon k}{K}\right)^2 e^{iKb} - \left(1 - \frac{\epsilon k}{K}\right)^2 e^{-iKb}} = \frac{i\left(1 - \frac{\epsilon^2 k^2}{K^2}\right) \sin Kb}{2 \frac{\epsilon k}{K} \cos Kb + i\left(1 + \frac{\epsilon^2 k^2}{K^2}\right) \sin Kb} \quad (64)$$

$$C_t = \frac{4 \frac{\epsilon k}{K}}{\left(1 + \frac{\epsilon k}{K}\right)^2 e^{iKb} - \left(1 - \frac{\epsilon k}{K}\right)^2 e^{-iKb}} = \frac{2 \frac{\epsilon k}{K}}{2 \frac{\epsilon k}{K} \cos Kb + i\left(1 + \frac{\epsilon^2 k^2}{K^2}\right) \sin Kb} \quad (65)$$

$$C_1 = \frac{2\left(1 + \frac{\epsilon k}{K}\right) e^{iKb}}{\left(1 + \frac{\epsilon k}{K}\right)^2 e^{iKb} - \left(1 - \frac{\epsilon k}{K}\right)^2 e^{-iKb}} = \frac{\left(1 + \frac{\epsilon k}{K}\right) (\cos Kb + i \sin Kb)}{2 \frac{\epsilon k}{K} \cos Kb + i\left(1 + \frac{\epsilon^2 k^2}{K^2}\right) \sin Kb} \quad (66)$$

$$C_2 = \frac{-2\left(1 - \frac{\epsilon k}{K}\right)}{\left(1 + \frac{\epsilon k}{K}\right)^2 e^{iKb} - \left(1 - \frac{\epsilon k}{K}\right)^2 e^{-iKb}} = \frac{\frac{\epsilon k}{K} - 1}{2 \frac{\epsilon k}{K} \cos Kb + i\left(1 + \frac{\epsilon^2 k^2}{K^2}\right) \sin Kb} \quad (67)$$

The breakwater depth and width are of the same order of magnitude so that small Kh implies small Kb . Utilizing equation (62) and the small argument identities:

$$\cos Kb, \sin Kb \rightarrow 1.0, Kb,$$

the reflection and transmission coefficients become:

$$C_r = \frac{S-if-\epsilon^2}{S-if+\epsilon^2 - 12\epsilon \frac{\sigma b}{\sqrt{gh}}}, \quad (68)$$

$$C_t = \frac{1}{1 + \frac{1}{2\epsilon} \frac{\sigma b}{\sqrt{gh}} (S-if+\epsilon^2)}, \quad (69)$$

and the dimensionless amplitudes of the components inside the breakwater are:

$$C_1 = \frac{(1 + \frac{\sqrt{S-if}}{\epsilon})(1 + \frac{i\sigma b}{\sqrt{gh}} \sqrt{S-if})}{2 + \frac{1}{\epsilon} \frac{\sigma b}{\sqrt{gh}} (S-if+\epsilon^2)}, \quad (70)$$

$$C_2 = \frac{1 - \frac{\sqrt{S-if}}{\epsilon}}{2 + \frac{1}{\epsilon} \frac{\sigma b}{\sqrt{gh}} (S-if+\epsilon^2)}. \quad (71)$$

f. Implications of the Long-Wave Solution. These equations represent an exact solution to the permeable breakwater problem for the specific case of an incident wave which is very long with respect to water depth and breakwater width. The simple form of the equations allows one to easily interpret the effect of various independent parameters on the solution. Some pertinent limiting conditions are: (a) as the media takes on the properties of pure seawater, i.e., 100 percent porosity and no damping, transmission becomes complete and no reflection occurs ($f \rightarrow 0$, $\epsilon \rightarrow 1$ with $S = 1$ yields $C_t \rightarrow 1$, $C_r \rightarrow 0$); (b) as the porosity approaches zero, the breakwater assumes the characteristic of a solid vertical wall and no transmission occurs while reflection becomes perfect ($\epsilon \rightarrow 0$ yields $C_t \rightarrow 0$, $C_r \rightarrow 1$); (c) as the damping properties of the media become severe, the transmission drops to zero and the reflection becomes perfect ($f \rightarrow \infty$ yields $C_t \rightarrow 0$, $C_r \rightarrow 1$); (d) as the breakwater becomes very thin, the transmission becomes nearly complete while the reflection becomes negligible ($b \rightarrow 0$ yields $C_t \rightarrow 1$, $C_r \rightarrow 0$); and (e) as the wave period becomes very long, such as a tidal oscillation, the transmission becomes complete and

no reflection occurs ($\sigma \rightarrow 0$ yields $C_t \rightarrow 1$, $C_r \rightarrow 0$). These same trends have been observed in the solution to the general problem for shorter waves as governed by equations (58) and (59).

Equation (69) verifies that increasing the friction coefficient, f , or the product of f with the wave frequency, σ , causes a relative decrease in the long-wave transmission coefficient. This behavior also applies to the short-wave solution. It will be useful to be able to predict the dependence of $f\sigma$ on the wave and breakwater characteristics. Lorentz's (1926) condition of equivalent work, as given by equation (9), specifies this dependence. The friction coefficient characterizes the damping throughout the breakwater so the volume integral in equation (9) may be replaced by a double integral on x and z with the submerged part of the breakwater as limits of integration:

$$f\sigma = \frac{\int_{-h}^0 dz \int_0^b dx \int_t^{t+T} \epsilon^2 \left\{ \frac{v_{q_R}^2}{K_p} + \frac{C_f \epsilon}{K_p^{1/2}} |q_R|^3 \right\} dt}{\int_{-h}^0 dz \int_0^b dx \int_t^{t+T} \epsilon q_R^2 dt}, \quad (72)$$

where q_R is the real part of the complex velocity, q . The numerator includes a term which is proportional to the cube of the velocity whereas the denominator is proportional to the square of the velocity. Consequently, relative increases in the velocity will cause relative increases in $f\sigma$. The velocity inside the breakwater is proportional to the product of the wave amplitude and wave frequency. The amplitude and frequency of the wave components inside the breakwater increase monotonically with increasing amplitude and frequency of the incident wave. Consequently, if the wave frequency is held constant then a relative increase in the incident amplitude will cause a relative increase in $f\sigma$. Likewise, if the amplitude is held constant, then a relative increase in the frequency, i.e., decrease in period and wavelength, will cause an increase in $f\sigma$. Since increasing $f\sigma$ causes a decrease in the transmission coefficient, it may be concluded that the transmission coefficient will decrease for increasing wave steepness or increasing wave number.

Appendix C discusses the numerical evaluation of equation (72) and the simplifications arising for the case of constant permeability.

This completes the formal theoretical solution to the crib-style breakwater problem. It will be useful to review the method by which numerical results are extracted from the theory before discussing example solutions.

g. Numerical Procedures. The formal generation of numerical results from the completed problem solution requires a preliminary evaluation of

the breakwater properties and specification of the incident wave conditions. The necessary breakwater properties are: (a) depth, h , (b) width, b , (c) porosity, ϵ , (d) permeability, K_p , and (e) turbulent damping coefficient, C_f . The depth is a function of the particular site and tidal range. The width is often fixed by economic considerations but can be adjusted to yield the desired breakwater performance. The three media properties are determined using the techniques discussed in Section III, 2.

The incident wave conditions are selected as design criterion using available forecasting techniques. The necessary properties are the dimensionless wave number, k_1h , and the wave steepness (or camber), H_1/L . The wave number and steepness are evaluated from the design wave period and height using conventional linear wave theory methods. It is usually desirable to investigate the behavior for a variety of wave conditions.

The above quantities are inputs or independent variables with respect to the theoretical solution. One decision remains to be made: how many eigen functions should be included in the solution? It will be demonstrated later that five eigen functions are sufficient for $k_1h \leq 3.0$, one is sufficient for $k_1h \leq 0.5$. To initiate the solution, a value for the damping coefficient, \bar{f} , is assumed ($f = 1.0$ is suitable). Then, the appropriate number of eigenvalues are evaluated from equation (25) using a complex Newton-Raphson quick convergence scheme. The eigenvalues, or equivalently the wave numbers, inside and outside the breakwater are used to enumerate the coefficients in the matrix equations (58) and (59). The matrix is solved using an efficient complex Gaussian reduction scheme for the complex reflection and transmission coefficients. These are substituted into the vector equations (60) and (61) to solve for the dimensionless amplitudes inside the breakwater. The seepage velocities are solved by differentiating the velocity potential (eqs. 27 and 28) with respect to x and z and introducing the internal wave amplitudes. The real components of the velocities are extracted and substituted into Lorentz's (1926) condition of equivalent work, (eq. 72), to compute f . If the result is different from the assumed value it is necessary to iterate and return to the step which evaluates the eigenvalues. If the assumed and computed values of f are within 1 percent, the solution is complete. The reflection and transmission coefficients are obtained by taking the absolute value of C_{r1} and C_{t1} , respectively. The iteration scheme typically closes after four to eight cycles.

A FORTRAN program has been written to perform these operations on a digital computer. It is listed and described in Appendix D.

h. Numerical Results. The following numerical results demonstrate the behavior of the theoretical solution as a function of the dimensionless parameters b/h , ϵ , f , and k_1h . Equations (58) to (61) and an earlier discussion identify these parameters as the quantities which ultimately govern the solution to the various modal amplitudes. Only b/h , ϵ , and k_1h are truly independent. The damping coefficient, f , is implicitly

a function of the media damping properties as well as the breakwater dimensions and internal wave characteristics. A consequence of this dependence is that a change in the media damping properties or the incident wave height is simulated by holding b/h , ϵ , and k_1h constant while varying f . Henceforth, the subscript will be omitted from the incident wave number.

The dependence on f is shown in Figure 6. In this figure, the reflection and transmission coefficients are plotted as a function of the dimensionless wave number kh for a square breakwater which is 40 percent porous. The breakwater shape and porosity are representative values and their effect is investigated in subsequent figures. The reflection coefficient is, by definition, equal to the absolute value of the complex dimensionless progressive mode amplitude in the reflected wave train,

$$C_R = |c_{r1}|.$$

Similarly, the transmission coefficient is equal to the absolute value of the complex dimensionless progressive mode amplitude in the transmitted wave train,

$$C_T = |c_{t1}|.$$

The long-wave solutions are also presented in Figure 6. The reflection and transmission coefficients are found by taking the absolute values of equations (68) and (69). The solutions are:

$$C_R = \left\{ \frac{(S - \epsilon^2)^2 + f^2}{(S + \epsilon^2)^2 + \left(f + \frac{2\epsilon\sqrt{gh}}{\sigma_b}\right)^2} \right\}^{\frac{1}{2}}, \quad (73)$$

$$C_T = \frac{1}{\left\{ \left(1 + \frac{\sigma_b f^2}{2\epsilon\sqrt{gh}}\right)^2 + \left\{ \frac{\sigma_b(S + \epsilon^2)}{2\epsilon\sqrt{gh}} \right\}^2 \right\}^{\frac{1}{2}}}. \quad (74)$$

The general results substantiate the behavior predicted by the long-wave solution--the transmission coefficient decreases monotonically with increased damping at all wave numbers. The increased damping may be a result of decreasing the media permeability or increasing the incident wave amplitude (steepness). In either case, the response is the same. Accompanying this behavior is an increase in the reflection coefficient. It may be concluded that increased damping results in an increased resistance to wave penetration and an increase in internal wave decay.

This result is somewhat analogous to the open-channel flow response to an abrupt increase in channel roughness. The water surface rises

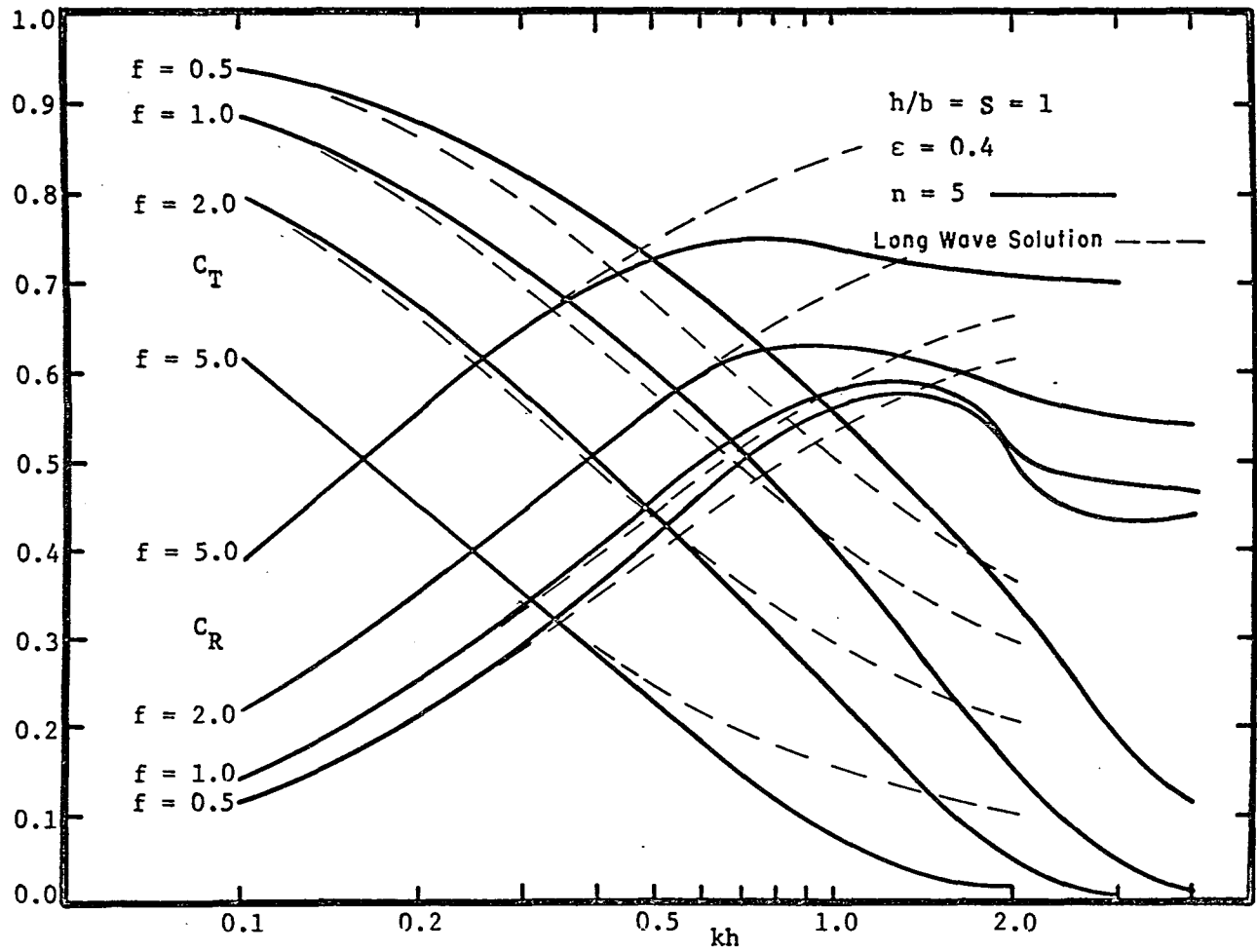


Figure 6. Reflection and transmission coefficient dependence on damping.

upstream to store potential energy in anticipation of the energy losses through the rough section. The breakwater system responds by increasing the potential energy of the partial standing wave and reflecting more energy back out to sea.

Figure 6 also supports the long-wave solution trends for decreasing wavelength, i.e., the reflection coefficient increases and the transmission coefficient decreases. An upper limit is reached near $kh = 1.0$, where the reflection coefficient attains a relative maximum. This appears to be a resonant phenomenon controlled by the η_2 component, (Fig. 5). This component reflects off the leeward breakwater face and propagates back through the interior of the structure and ultimately contributes in part to the reflected wave train. As the wavelength shortens, the relative resistance inside the breakwater increases. This accentuates the media discontinuity at the sea-breakwater interface and causes more direct reflection of the incident wave but decreases the amount of η_2 available to the reflected wave train. Further decreases in the wavelength cause the internal damping to become so severe that virtually nothing is left of the η_2 component to contribute to the reflected wave train. Then the reflection coefficient becomes mainly a surface phenomenon and is controlled by the porosity of the windward breakwater face. Note that as the absolute level of damping is increased ($> f$), the resonant condition moves to even longer wavelengths ($< kh$). This is probably caused by the decrease in wavelength inside the breakwater due to increased friction.

The long-wave solution compares favorably with the general solution up to a wave number of approximately $kh \sim 0.5$. For intermediate wave numbers the long-wave solution tends to slightly underestimate the reflection and transmission coefficients, while for high-wave numbers it overestimates both coefficients. The reasons for this latter behavior are easily understood. The long-wave solution yields a lower frequency oscillation (eq. 62) for a given wave number than the general solution (eq. 25). The low-frequency oscillations are damped less severely as they pass through the breakwater, thus the transmission coefficient is greater. Similarly, the η_2 component propagating back through the breakwater is damped less severely for low-frequency oscillations, and it can contribute more to the reflected wave when it reaches the windward face. Thus, the long-wave solution overestimates the reflection coefficient at high-wave numbers. This also accounts for the resonant phenomenon not appearing in the long-wave reflection coefficient. Further errors are anticipated when the long-wave approximation is substituted into the Lorentz equation calculation for f in actual breakwater forms. Nevertheless, the long-wave approximation provides a rapid solution with acceptable accuracy for $kh < 0.5$.

These same features apply to increasing breakwater widths, as shown in Figure 7. As in Figure 6, the reflection and transmission coefficients are plotted as a function of wave number for a 40 percent porous structure. However, the damping coefficient is held constant and is equal to unity.

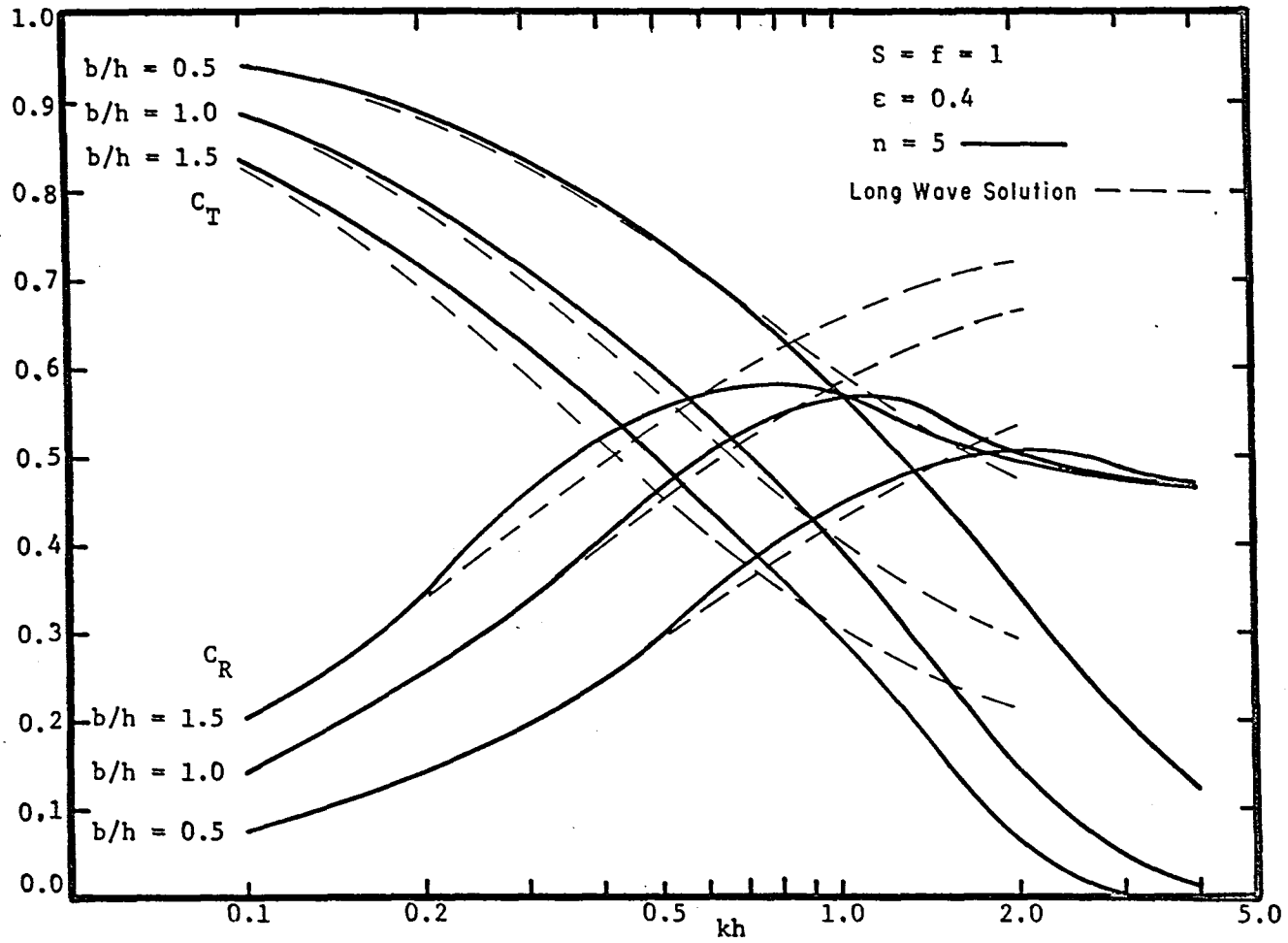


Figure 7. Reflection and transmission coefficient dependence on breakwater width.

In the real case, f is not constant, but this figure still serves to isolate the effect of changing the relative width (or depth). Increasing widths behave like increased damping, and this results in more reflection and less transmission.

The dependence on porosity is shown in Figure 8. Again, the reflection and transmission coefficients are plotted versus wave number. The particular case depicted is a square breakwater with constant damping coefficient equal to unity. Most natural gravel materials have porosities in the range $0.30 < \epsilon < 0.5$. The effect of halving and doubling a mean value of $\epsilon = 0.4$ is given. Decreasing the porosity causes an increase in the reflection coefficient and a decrease in the transmission coefficient at all wave numbers. The reflection coefficient is most sensitive to changes in porosity and this sensitivity increases with the wave number. This behavior is exaggerated for the case of constant f . When the same change in porosity is applied to an actual breakwater form and f is calculated from the media and wave properties, the resulting change in the reflection and transmission coefficients is approximately one-third that shown in Figure 8. The long-wave solution behavior is the same as in Figures 6 and 7. Increasing porosity accentuates the difference between the long wave and general solutions but correlation remains excellent below $kh \approx 0.5$.

The inertial coefficient, S , was introduced earlier to incorporate the effect of added mass in widely spaced pile-array breakwaters. The sensitivity to this coefficient is shown in Figure 9. The added mass concept arises due to unsteady converging and diverging of streamlines around solid bodies. This results in increased resistance to flow and therefore causes an increase in the reflection coefficient and decrease in the transmission coefficient (Fig. 9).

The convergent character of the theoretical eigen-series solution is demonstrated in Figure 10. In this figure, the reflection and transmission coefficients are plotted versus the reciprocal of the number of eigen functions summed in the series solution. The results for three different wave numbers are given for a square breakwater which is 40 percent porous and has a damping coefficient equal to two. The results show that solution converges quickly as the number of eigen functions is increased from one to infinity. For long waves, $kh = 0.1$, one eigen function yields the same solution as the extrapolated value for an infinite series. This concurs with the anticipated result for long waves. Intermediate wave numbers, near $kh = 1.0$, require two or three eigen functions to give the same result as an infinite series. Shorter waves near $kh = 2.0$ converge within 2 percent of their ultimate value when five eigen functions are summed. Summing more than 10 eigen functions introduces roundout errors into the matrix solution unless double precision is used in the computation scheme. Thus, $n = 5$ is used for all waves occurring outside the deepwater range ($kh < \Pi$) to combine acceptable convergence with negligible roundout error.

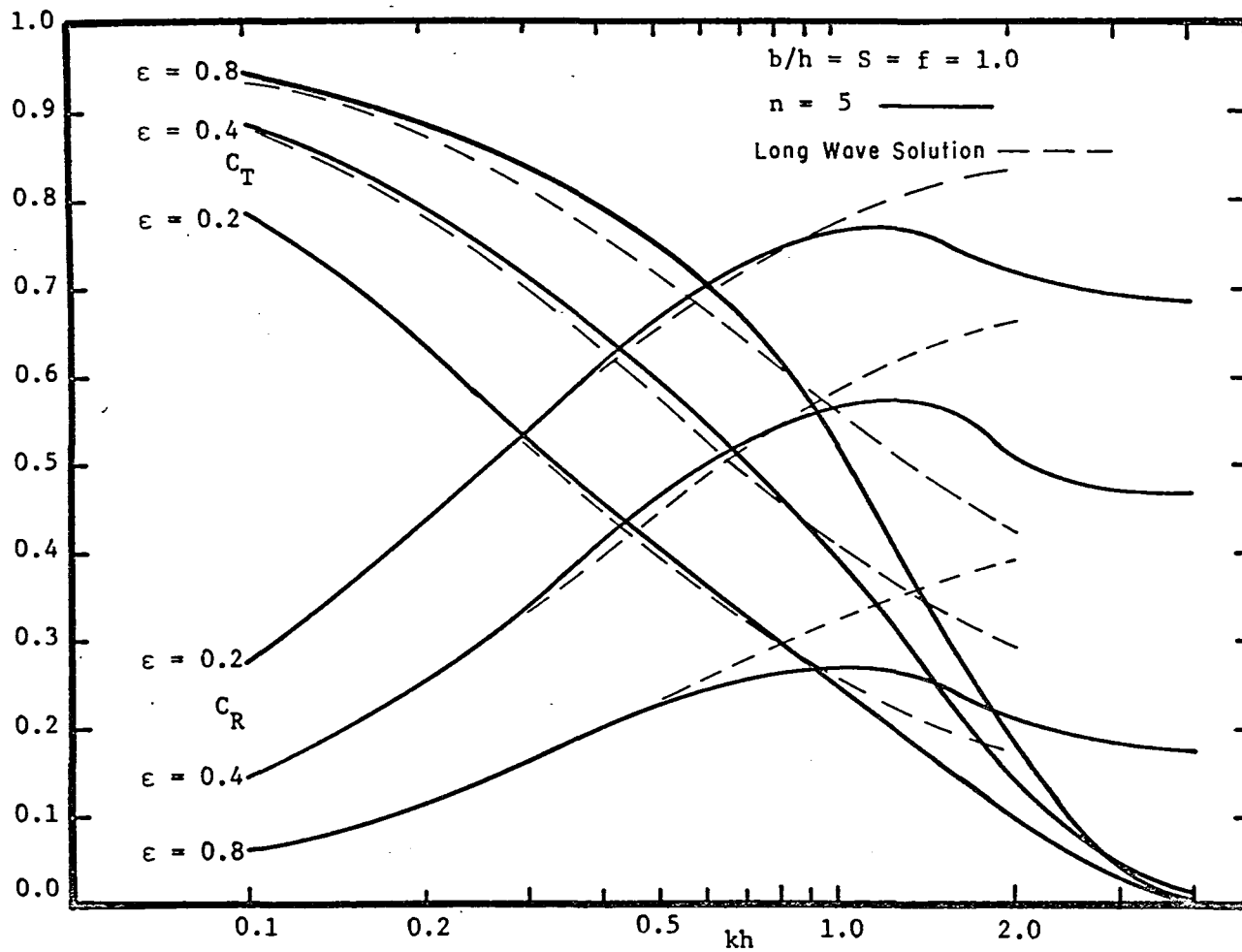


Figure 8. Reflection and transmission coefficient dependence on porosity.

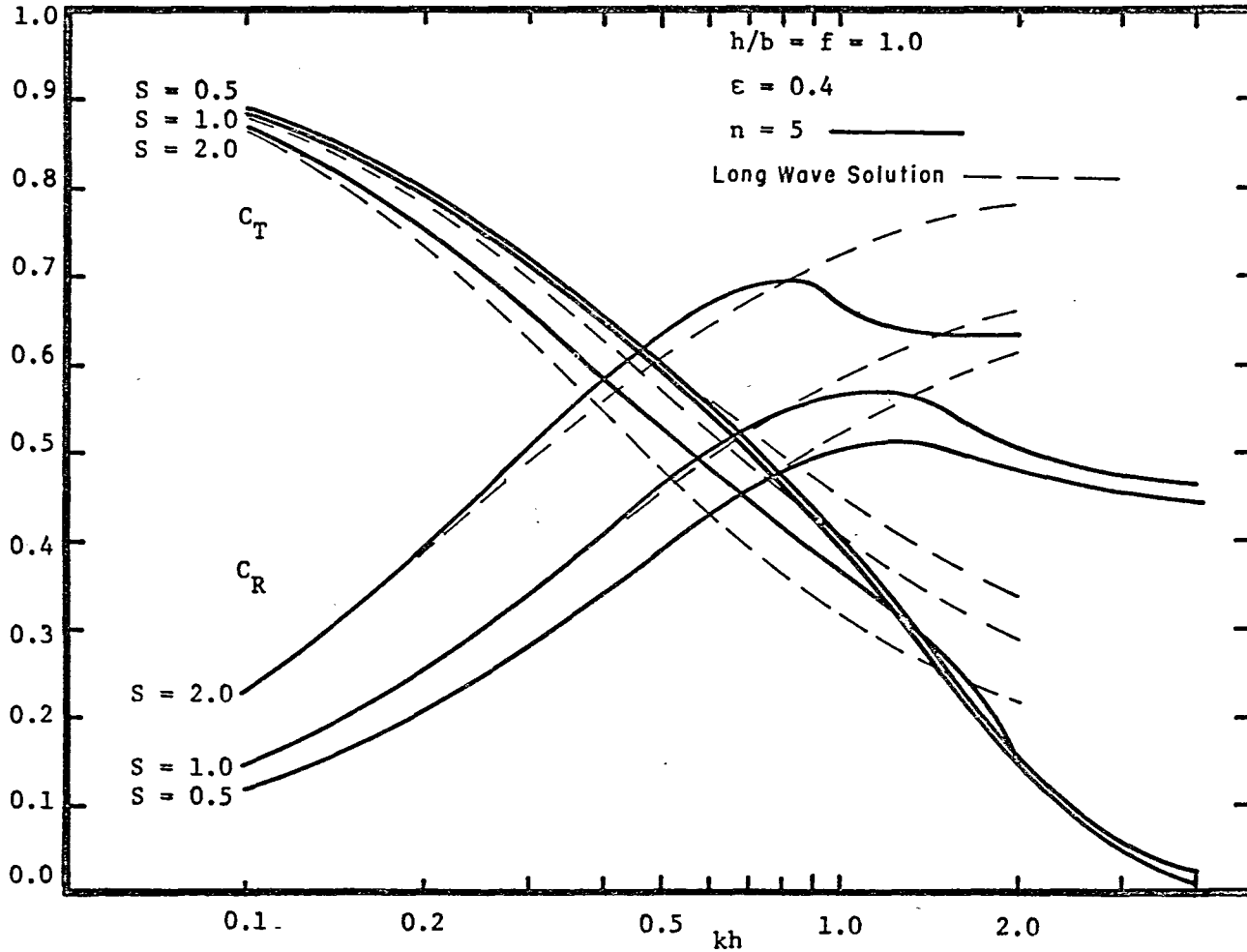


Figure 9. Reflection and transmission coefficient dependence on inertial coefficient.

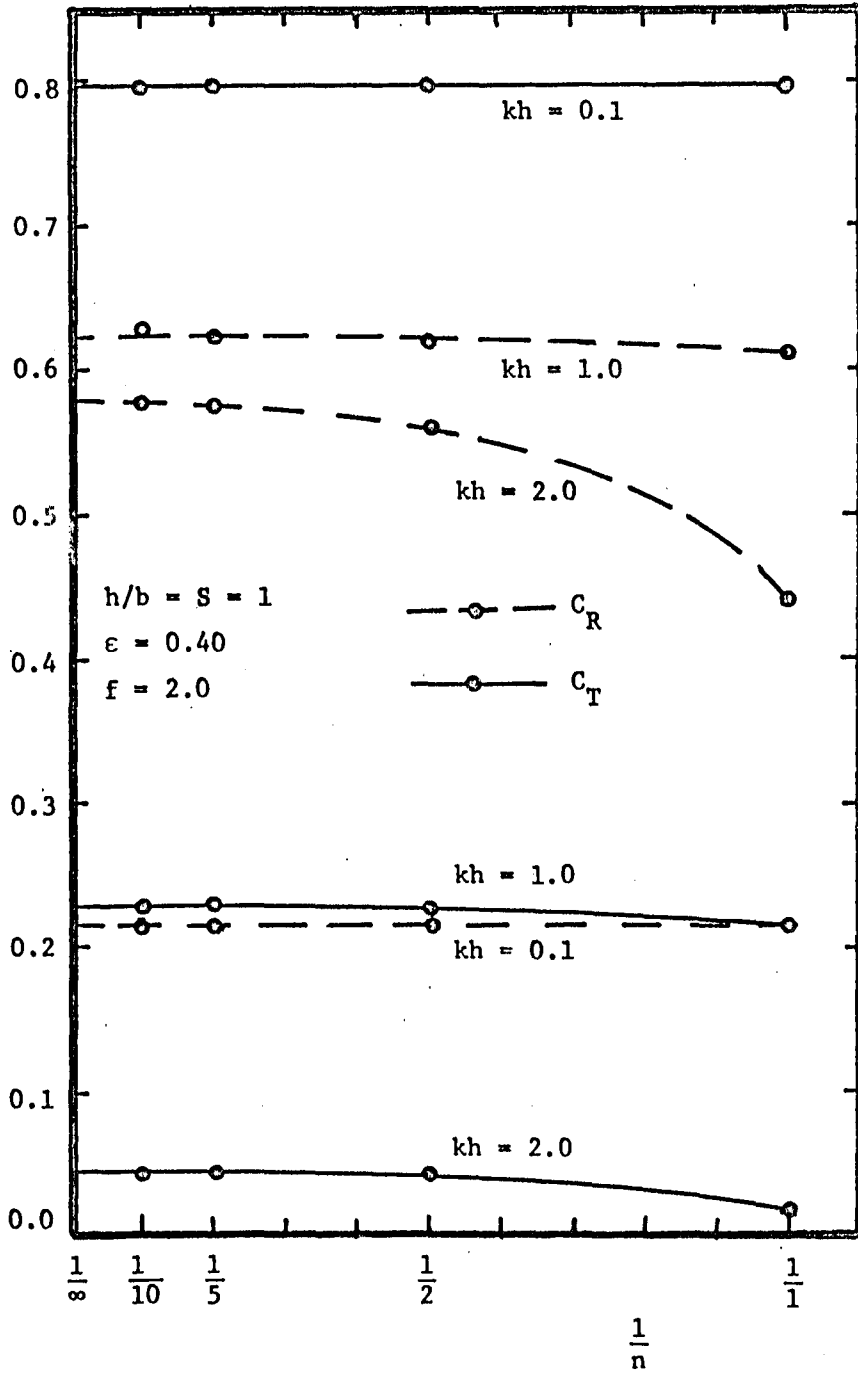


Figure 10. Convergence dependence on number of eigen functions.

This concludes the theoretical development of the crib-style breakwater solution. Comparison between experiment and theory is discussed in Section IV. The application of the theory to sloping-face breakwaters is discussed below.

5. Conventional Breakwater Schemes.

a. A Rigorous Approach. The preceding discussion has been limited to permeable structures of rectangular form. The inclusion of conventional trapezoidal-shaped breakwaters greatly complicates the problem. To illustrate this, consider Figure 11 depicting a hypothetical breakwater scheme. The zones identify distinct regions, each of which has its own characteristic boundary value problem. The effects of heterogeneous layering are assumed to be accounted for by an average linearized friction coefficient in each region. The boundary value problem in region IV is similar to the crib-style breakwater problem discussed previously. An eigen-series solution satisfies this problem with n modes propagating in both the positive and negative longitudinal directions. The solutions in regions I and VII can be assumed to be given by linear wave theory. This introduces n -reflected and n -transmitted modes. The general forms of the solutions in regions II, III, V, and VI are not known. The diagonal interface between adjacent regions produces nonhomogeneous boundary conditions and couples the solution in a very complicated fashion. For the present discussion it will be assumed that a periodic series solution applies in these regions and that n terms in each series, propagating in both directions, will specify the solution adequately. The boundary conditions of continuity of pressure and mass flux applied at the interface between each of the seven regions produce $12n$ equations which ideally could be solved for the $12n$ unknown amplitudes and series constants. It follows that the trapezoidal-shaped breakwater produces three times as many unknowns as the rectangular-shaped breakwater problem and the effort required to solve the equation matrix alone is proportional to the matrix size raised to the third power.

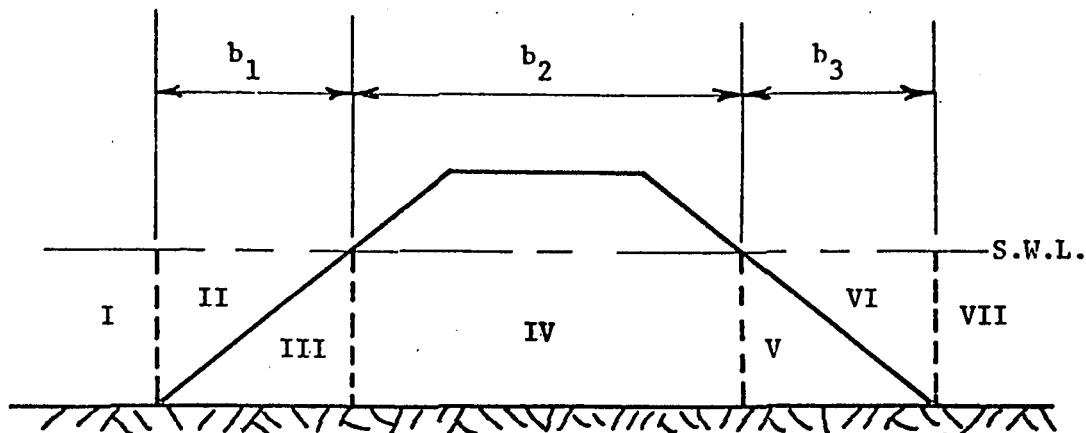


Figure 11. Trapezoidal breakwater.

The problem is made more difficult by the complexity of wave interaction with rough inclined surfaces. Breakwater faces are typically sloped at 1.5:1 or less and this induces breaking in the incident wave. Previous investigators have been frustrated with the idealized problem of wave breaking on impermeable slopes (Le Méhauté, 1966; Koh, 1966). Existing methods for predicting the energy consumed in breaking on such slopes are semiempirical at best. Consequently, the wave-breaking part of the problem itself is a very ambitious undertaking. When one adds to these complications the effect of heterogeneous layering, the mechanical effort involved in attempting a rigorous analytical solution becomes very great indeed. Even if such a solution were obtained, the complexity and number of simultaneous equations describing the solution would probably mask any attempt to draw general conclusions about the system behavior. However, this last item is the single most important feature of analytical solutions as opposed to numerical solutions. Consequently, it may be beneficial to simplify the approach to the problem to amplify an overall understanding of the basic governing processes.

b. The Equivalent Rectangular Breakwater. One might attempt to simplify the problem by applying the eigen-series solution of region IV to regions III and V. Similarly, the linear wave theory eigen series could be applied to regions II and VI. Then the boundary conditions of normal mass flux and pressure continuity at the sloping interfaces could be solved for the various unknown amplitudes. Such an approximation does confine the damping process to the appropriate regions but does not satisfy the free surface and impermeable bottom boundary conditions simultaneously.

To satisfy these latter conditions, it might be preferable to extend the solution of region IV midway into regions II, III, V, and VI. This would require that the linear wave theory solution be extended into the outer half of these respective regions. The approach is approximate because it applies the damped solution to regions II' and VI' (Fig. 12) and ignores the losses due to regions III' and V'. The two approximations should be partially compensating. Furthermore, use of the potential flow solution requires that a constant porosity be assigned to the breakwater. Once these approximations are made, the solutions applied throughout the full depth and the free surface as well as the bottom boundary condition are satisfied.

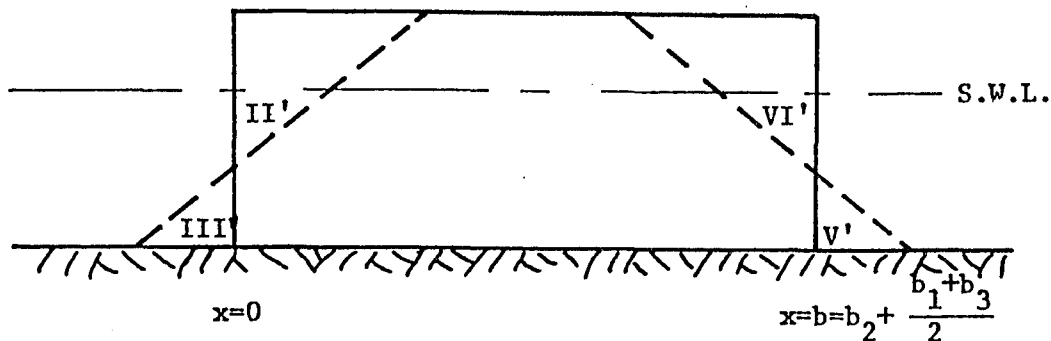


Figure 12. Equivalent rectangular breakwater.

This study uses the second approach to replace regions II through VI (Fig. 11) with an equivalent rectangular breakwater which has the same submerged volume as that of the trapezoidal breakwater. That is, a hypothetical breakwater is formed by bisecting the slopes between regions II and III and between V and VI with vertical planes (see Fig. 12). Within the confine of these planes, the rectangular breakwater has the same internal structure as the trapezoidal breakwater, and the crib-style breakwater solution is used to describe the flow field. Exterior to these planes, linear wave theory is applied to describe the incident, reflected, and transmitted wave trains. The two solutions are matched at the hypothetical interfaces to satisfy continuity of pressure and horizontal mass flux, and thereby solve for the unknown modal amplitudes.

Lorentz's (1926) condition of equivalent work was used to evaluate a linearized damping coefficient, f , which applies throughout the hypothetical rectangular breakwater. However, unlike the condition derived for the crib-style breakwater, the new equivalent work principle attempts to account for the effect of energy dissipation due to waves breaking on the windward slope. This is accomplished by modifying a theory attributed to Miche (1951) which estimated the wave energy losses on impermeable slopes. These losses are added to the frictional losses in the numerator of equation (72) to yield a revised estimate to the damping coefficient, f . In this manner the surface-breaking dissipation is incorporated with the internal-friction dissipation. Finally, that part of the theory which satisfied the interfacial boundary conditions distributes the breaking effect among the various modal components in the reflected and transmitted waves.

c. Modifying Miche's Breaking Criterion. To proceed with this model, it is necessary to evaluate the energy loss due to waves breaking on the windward breakwater slope. Miche's (1951) technique has been shown to give reasonable correlation between experiment and theory for smooth impermeable slopes (Straub, 1956). Through the use of an empirical surface coefficient, δ , his results have been extended somewhat less successfully to rough and permeable slopes.

Miche's breaking criterion was based on the hypothesis that the maximum water surface slope attainable without breaking on a reflecting surface is equal to the slope of the reflecting surface itself. He used linear wave theory to transform the maximum nearshore wave steepness to deep water where it is then possible to define a critical deepwater wave steepness. The result was:

$$\left(\frac{H_o}{L_o}\right)_{crit} = \left(\frac{2\beta}{\Pi}\right)^{\frac{1}{2}} \frac{\sin^2 \beta}{\Pi}, \quad (75)$$

where β is the surface slope, measured from a horizontal reference in radians, and the left-hand side of the equation is the critical deepwater wave steepness. Miche concluded that because $(H_o/L_o)_{crit}$ is the maximum

steepness which remains stable on the slope, any deepwater wave steepness, H_o/L_o , which exceeds this will break and be reflected at the critical steepness. The definition for a reflection coefficient follows directly as:

$$C'_\delta = \frac{(H_o/L_o)_{crit}}{(H_o/L_o)}. \quad (76)$$

Miche (1951) found that the discrepancy between his theory and experimental reflection coefficients for rough and permeable slopes could be corrected by introducing an empirical coefficient, δ , which he called the intrinsic surface-reflection coefficient. This coefficient has been found to depend on wave steepness and wave number as well as surface characteristics (Moraes, 1970). Although no method presently exists for predicting δ , it is common to experimentally evaluate this coefficient in comparing the breaking characteristics of various slopes. The revised reflection coefficient may be written as:

$$C_\delta = \delta C'_\delta, \quad (77)$$

where C'_δ is the predicted reflection coefficient for smooth slopes and C_δ is the corresponding coefficient for rough or permeable slopes.

This study proceeds with the assumption that Miche's technique is an acceptable approximation to the wave-breaking process on a smooth impermeable surface. Furthermore, it is assumed that the effect of the slope of the reflecting surface is separable and that this effect is properly identified by the right-hand side of equation (75). Then δ incorporates the Reynolds effect of surface roughness combined with wave properties. At this point, the theory digresses from Miche's hypothesis that all of the energy which remains after breaking is returned in the form of a reflected wave. Instead, it is assumed that with the proper intrinsic reflection coefficient, Miche's equation may be used to calculate that part of the incident wave energy which remains after breaking and is available for transmission into the permeable breakwater and reflection back out to sea. Thus, Miche's equation is used to model the wave-breaking process rather than wave reflection, and his reflection coefficient may be interpreted as the dimensionless amplitude of a fictitious wave which accounts for that part of the incident wave energy remaining after breaking on the windward slope.

Energy conservation requires that the power lost to breaking equal the difference in energy propagation rates of the incident wave and the fictitious reflected wave. According to linear wave theory the difference in energy propagation rates is (Ippen, 1966):

$$\dot{E}_{loss} = \frac{\gamma a_1^2}{2} C_g (1 - C_\delta^2),$$

where $\dot{\bar{E}}$ is the period-averaged power loss and C_g is the group celerity of the incident wave. The group celerity may be written in one of its many forms as:

$$C_g = \frac{g}{\sigma} \left(\frac{\text{sh } 2kh + 2kh}{2\text{ch}^2 kh} \right).$$

Thus,

$$\dot{\bar{E}}_{\text{loss}} = \frac{\gamma a_i^2}{2} \frac{g}{2\sigma} \left(\frac{\text{sh } 2kh + 2kh}{2\text{ch}^2 kh} \right) (1 - C_\delta^2). \quad (78)$$

Combining equations (76), (77), and (78):

$$C_\delta = \delta \left(\frac{2\beta}{\Pi} \right)^{\frac{1}{2}} \frac{\sin^2 \beta}{\Pi} / (H_o/L_o).$$

Linear wave theory provides a simple transformation for the deepwater wave steepness, H_o/L_o , to the wave steepness at any depth h , H_i/L :

$$\frac{H_o}{L_o} = \frac{H_i}{L} \left(\frac{2kh + \text{sh } 2kh}{2\text{ch}^2 kh} \right)^{\frac{1}{2}} \text{th } kh.$$

In terms of wave parameters at the breakwater site, Miche's (1951) coefficient becomes:

$$C_\delta = \delta \left(\frac{2\beta}{\Pi} \right)^{\frac{1}{2}} \frac{\sin^2 \beta}{\Pi} / \left\{ \frac{H_i}{L} \left(\frac{2kh + \text{sh}^2 kh}{2\text{ch}^2 kh} \right)^{\frac{1}{2}} \text{th } kh \right\}. \quad (79)$$

To evaluate the power lost in breaking, it is necessary to specify the intrinsic reflection coefficient, δ . As discussed previously, this term is expected to be a function of the reflecting surface and wave characteristics. The frictional losses due to flow through the permeable slope are accounted for by the porous media part of the solution. Consequently, δ need only account for pure breaking. The exposed slopes of most practical breakwater designs are typically steeper than 1:2.5 and, because of depth limitations, they are of relatively limited extent. As a result, long waves experience little transformation on the slope while short waves tend to steepen and break. It follows that δ should approach unity for very long waves (no breaking) and approach zero for very short waves (complete breaking). In addition, increasing surface roughness and decreasing slope should accentuate the breaking process. An empirical expression proposed by the author which incorporates this anticipated behavior is:

$$\delta = 1 - e^{-1 / \left(\frac{f_s}{\tan \beta} \frac{\sigma^2 h}{g} \right)}, \quad (80)$$

where f_s is a dimensionless surface-roughness coefficient. Note that:

$$\delta \rightarrow 1 \text{ when } \begin{cases} \frac{\sigma^2 h}{g} \rightarrow 0, \text{ long waves} \\ f_s \rightarrow 0, \text{ smooth slopes} \\ \tan \beta \rightarrow \infty, \text{ vertical slopes} \end{cases}$$

$$\delta \rightarrow 0 \text{ when } \begin{cases} \frac{\sigma^2 h}{g} \rightarrow \infty, \text{ short waves} \\ f_s \rightarrow \infty, \text{ rough slopes} \\ \tan \beta \rightarrow 0, \text{ horizontal slopes} \end{cases}$$

Although equation (80) behaves in a intuitively agreeable manner, it may be argued that not much has been gained because the surface coefficient, f_s , remains to be evaluated. It is true that f_s is an unknown quantity; however, by heuristic arguments its effect has been separated from the surface slope and wavelength. It will be shown by comparison with experimental results that f_s behaves like a geometric property which remains invariant during changes in the system dynamics. Furthermore, f_s assumes a constant value which characterizes the armor-layer material on the breakwater slope.

It is not possible to predict f_s from previous experiments. To the writer's knowledge, no other investigators have attempted to separate surface breaking and internal losses from wave reflection on permeable slopes. Straub (1956) measured the reflection coefficients for various permeable slopes. He evaluated Miche's (1951) intrinsic reflection coefficient by computing the ratio of the measured coefficient with that predicted by equation (76). His results showed that δ decreases with decreasing wavelength and decreasing slope angles. This behavior is incorporated in equation (80). In addition, his results indicated that δ decreases with decreasing wave steepness. This characteristic is accounted for by the porous media model in this study.

To indicate the order of magnitude of f_s , one can invert equation (80) to yield:

$$f_s = \frac{\tan \beta}{\frac{\sigma^2 h}{g} \ln \left(\frac{1}{1-\delta} \right)}. \quad (81)$$

Now Straub's data can be analyzed to find an f_s which incorporates the effect of internal damping. His results include data for a wedge-shaped absorber composed of crushed rock which passes a 3/4-inch screen and which is retained on a 1/4-inch screen. The structure is sloped at 22° and is 46 percent porous. For an offshore wave steepness of 0.04 he determines

intrinsic reflection coefficients $\delta = 0.12, 0.18, \text{ and } 0.25$ corresponding to $\sigma^2 h/g = 2.32, 1.28, \text{ and } 0.844$, respectively. Equation (81) yields $f_s = 1.40, 1.58, \text{ and } 1.68$. The resulting values are within 11 percent of being constant and seem to characterize the absolute roughness of the slope. The values are higher than those anticipated for this study because they include the effect of internal porous media losses.

d. Combining Breaking and Internal Losses. The surface-roughness coefficient is calibrated by comparing experiment with theory for a limited number of conditions. Once evaluated, it can be used to extend results into ranges which have not been explored experimentally. Ideally, this parameter will characterize the absolute roughness of similar slopes in other models or prototype breakwaters.

The method used to incorporate wave breaking into the theory is to combine the breaking and internal losses in Lorentz's (1926) condition of equivalent work. This effectively increases the linear friction coefficient, f , by requiring that the linearized damping law account for the same amount of dissipation during one wave period as that caused by turbulent internal damping and wave breaking. Dividing equation (79) through by ρ and adding the resulting quantity to the numerator of equation (C-3) (App. C) satisfies this requirement:

$$f\sigma = \frac{\int_{-h}^0 dz \int_0^b dx \left[\epsilon^2 \left\{ \frac{v}{K} \frac{1}{2} (Q_R^2 + Q_I^2) + \frac{C_f}{K} \frac{1}{2} \epsilon \frac{4}{3\pi} (Q_R^2 + Q_I^2)^{\frac{3}{2}} \right\} + \frac{\dot{E} \text{ loss}}{\rho} \right]}{\int_{-h}^0 dz \int_0^b dx \left[\epsilon \frac{1}{2} (Q_R^2 + Q_I^2) \right]}, \quad (82)$$

where

$$Q_R = \text{Real} (q/e^{i\sigma t}),$$

$$Q_I = \text{Imaginary} (q/e^{i\sigma t}),$$

and \dot{E} loss is evaluated from equations (78), (79), and (80). Finally, equation (82) is combined with dispersion equation (25), and the interfacial boundary conditions, equations (58) to (61) to completely specify the trapezoidal breakwater problem.

e. Comments on the Sloping-Face Breakwater Solution. The trapezoidal breakwater solution is an extension of the crib-style breakwater solution which includes a consideration for wave breaking. This approach does greatly simplify the problem and yet it reproduces the important features in an intuitively reasonable manner. For example, an approximate homogeneous damping law is assumed to apply throughout the interior of the breakwater so that a relatively simple velocity distribution may be found.

After the velocity field is known, it is run through the actual heterogeneous internal structure of the breakwater and revised until the damping resulting from the simplified structure is the same as that resulting from the actual structure.

The second important feature involves wave breaking. If the slope were impermeable, the breaking losses would simply reduce the reflected wave modal amplitudes. However, waves breaking on permeable slopes reduce the interior and transmitted wave components as well as the reflected wave components. It is unnecessary to prescribe some arbitrary method for distributing these losses among the various components if the internal and breaking losses are combined into a single calculation for the linearized friction coefficient, f . The new f changes the coefficient matrix in the interfacial boundary condition equations and thereby redistributes the effect of the losses among the modal component amplitudes. Adding breaking losses to the equivalent work principle increases the value of f . This in turn increases the value of the damping exponent, α_n , in equation (33) and a larger damping exponent causes the modes propagating through the breakwater interior to decay more quickly. In addition, the rate of exponential decay is maximum where the function itself is maximum, that is:

$$\eta_n = a_n e^{i\{-\Gamma_n(1 - i\alpha_n)x + \sigma t\}},$$

and

$$\frac{d\eta_n}{dx} = -\alpha_n \Gamma_n \eta_n \{\text{decay rate}\} - i \Gamma_n \eta_n \{\text{propagation rate}\},$$

therefore,

$$\left\{ \frac{d\eta_n}{dx} \right\}_{\text{maximum decay rate}} = -\alpha_n \Gamma_n \left\{ \eta_n \right\}_{\text{maximum}},$$

and the η_n are maximum at $x = 0$. Consequently, waves decay most rapidly in the hypothetical rectangular breakwater in the same vicinity where breaking occurs in the actual breakwater.

It may be concluded that the trapezoidal breakwater solution, although relatively simple with respect to the mathematical details, does reproduce the important governing processes in a manner which is similar to the actual physical phenomenon.

f. Numerical Procedures. The nonhomogeneous sloping-face breakwater solution is identical to the crib-style breakwater solution except for some additional requirements on Lorentz's condition of equivalent work. Thus, the procedures discussed earlier apply with the following additions.

The equivalent rectangular breakwater width (according to the definition in this report) is equal to the crest width at the SWL plus half the sum of the horizontal projections of the two slopes extending below the SWL. To apply the orthogonalized form of the interfacial boundary conditions, a constant porosity must be assumed in the rectangular model. This is equal to the depth-averaged porosity at the sea-breakwater interface ($x = 0$). The media properties are prescribed at discrete grid points within the confines of the equivalent rectangle. This is an input to the numerical spatial integration of the numerator in the Lorentz (1926) equation (82). Details are presented in Appendix E. The velocities are evaluated at each grid point and a trapezoidal rule is used to perform the integration. The breaking loss is enumerated via equations (78), (79), and (80). It is necessary to estimate the surface coefficient, f_s , to compute the breaking loss. To indicate the order of magnitude of this coefficient, a value of $f_s = 1/3$ is found to give best correlation between experiment and theory for the armor layer used in this study.

By following these instructions, the effect of nonhomogeneous media and breaking losses can be included in the evaluation of the damping coefficient, f , in equation (82). Substituting this step into the method previously outlined (Sec. II, 4, g) completes the procedure used to solve the conventional breakwater problem.

The gross effect of wave breaking is to increase f at all but the smallest wave numbers. As illustrated in Figure 6, this causes the reflection coefficient to increase and the transmission coefficient to decrease. Comparison with specific experimental results is undertaken in Section IV.

6. Pile-Array Breakwaters.

a. General Description. Pile-array breakwaters are a familiar subset in the general category of permeable breakwaters. They are often constructed to support wharves or offshore structures and their function as breakwaters may be of secondary importance. Loading requirements combined with subocean soil conditions often prohibit dense packing of the pile foundation. Model experiments on pile arrays (Costello, 1952) have demonstrated that they are, in general, relatively transparent to wave activity. Nevertheless, in many applications it is useful to be able to predict what level of protection they afford and how that level might be improved.

b. The Governing Equations. In most applications the piles are driven vertically into the ocean floor with the top of the pile extending above the design wave height elevation. The piles are typically spaced at two or more pile diameters, center to center. In this study it will be assumed that the spacing is great enough to apply Morison's equation to evaluate the wave forces on individual piles. The fluid forces on the pile are equal and opposite to the pile forces imposed on the fluid. Morison's equation prescribes these forces analytically as:

$$\frac{dF}{dz} = C_D \rho D \frac{u|u|}{2} + C_M \rho \frac{\pi D^2}{4} \ddot{u}, \quad (83)$$

where dF_p/dz is the force per unit length exerted on a vertical cylindrical pile of diameter D due to drag and inertial forces. The drag force is characterized by the drag coefficient, C_D (Schlichting, 1968), and the horizontal approach velocity, u . The inertial force is characterized by the virtual mass coefficient, C_M (Robertson, 1965), and the local acceleration in the approach velocity, u .

The seepage velocity concept is used to describe the flow field in the voids between the piles. Thus, equation (1) may be applied with S equal to unity. The total stress tensor of apparent turbulent friction is replaced by the pile force exerted on each unit mass of surrounding fluid so that equation (1) becomes:

$$\frac{\partial q}{\partial t} = -\frac{1}{\rho} \nabla(p + \gamma z) - \hat{i} \frac{dF}{dV} p, \quad (84)$$

with

$$\nabla \cdot q = 0,$$

where \hat{i} is the unit vector in the longitudinal x -direction. The volume derivative of F_p is simply equal to the depth gradient in F_p (eq. 83) divided by the average distribution of horizontal water surface area per pile. Referring to Figure 13,

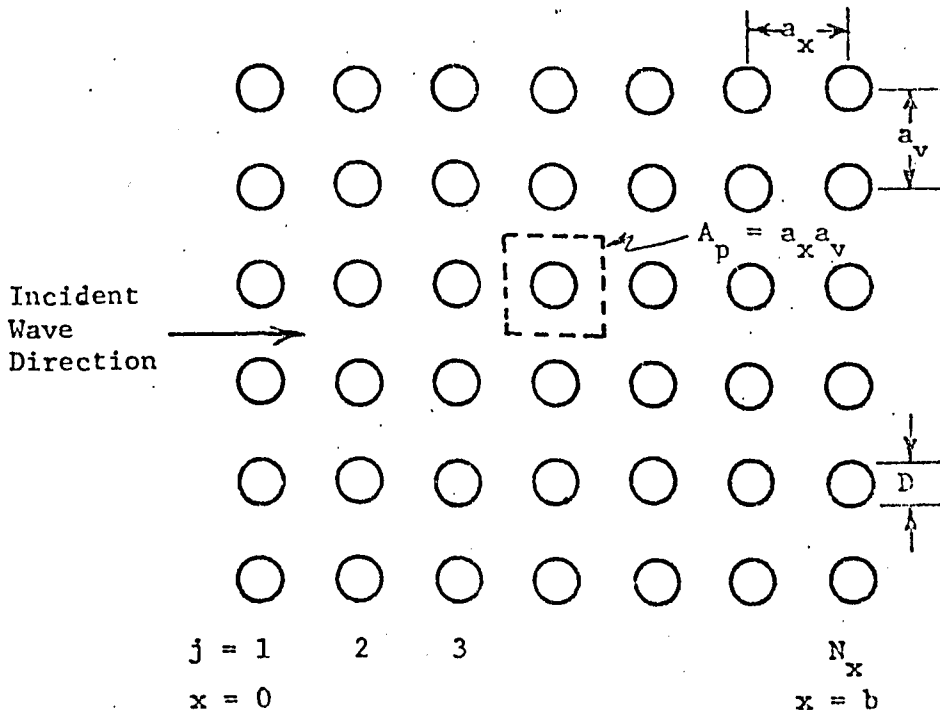


Figure 13. Pile-array pattern.

$$\frac{dF_p}{dV} = \frac{1}{\epsilon A_p} \frac{dF_p}{dz}, \quad (85)$$

where

$$\epsilon = \frac{A_p - \Pi D^2/4}{A_p}, \quad \text{the array porosity.} \quad (86)$$

Combining equations (83) and (85):

$$\frac{1}{\rho} \frac{dF_p}{dV} = \frac{C_D D}{\epsilon A_p} \frac{u|u|}{2} + \frac{C_M}{\epsilon A_p} \frac{\Pi D^2}{4} \dot{u}.$$

But

$$\frac{\Pi D^2/4}{A_p} = 1 - \epsilon,$$

thus,

$$\frac{1}{\rho} \frac{dF_p}{dV} = \frac{D}{\epsilon A_p} C_D \frac{u|u|}{2} + \frac{1-\epsilon}{\epsilon} C_M \dot{u}. \quad (87)$$

Substituting equation (87) into equation (84):

$$\frac{\partial q}{\partial t} = -\frac{1}{\rho} \nabla(p + \gamma z) - \hat{i} \left(\frac{D}{\epsilon A_p} C_D \frac{u|u|}{2} + \frac{1-\epsilon}{\epsilon} C_M \dot{u} \right). \quad (88)$$

When the excitation is provided by a long incident wave, the vertical velocity components become negligible so that:

$$\hat{i} (u, \dot{u}) = q, \frac{\partial q}{\partial t}.$$

Then the inertial force and the local acceleration may be combined on the left-hand side of equation (88) to yield:

$$\hat{i} \left(1 + \frac{1-\epsilon}{\epsilon} C_M \right) \frac{\partial u}{\partial t} = -\frac{1}{\rho} \nabla(p + \gamma z) - \hat{i} \frac{D}{\epsilon A_p} C_D \frac{u|u|}{2}.$$

As an approximation to the intermediate and short-wave condition, it will be assumed that the virtual mass has the same effect on the vertical acceleration component. For the case of horizontal cylinders this would be true. It represents a convenient approximation for the vertical-pile application and permits equation (88) to be expressed as:

$$\left(1 + \frac{1-\epsilon}{\epsilon} C_M \right) \frac{\partial q}{\partial t} = -\frac{1}{\rho} \nabla(p + \gamma z) - \hat{i} \frac{D}{A_p} C_D \frac{u|u|}{2}. \quad (89)$$

The inertial force is a conservative force resulting from unsteady diverging and converging streamlines around solid bodies. It is not a dissipative force like the drag component, and therefore it identifies more closely with acceleration in the approach velocity than with the drag force. The coefficient of the local acceleration term defines the pile-array inertial coefficient S as:

$$S = 1 + \frac{1-\epsilon}{\epsilon} C_M. \quad (90)$$

The drag force is linearized using the technique in Section II, 2, f, i.e., the nonlinear drag force is replaced by:

$$\frac{D}{\epsilon A} C_D \frac{u|u|}{2} \rightarrow f\sigma q. \quad (91)$$

Lorentz's (1926) condition of equivalent work is used to evaluate f such that $f\sigma q$ dissipates the same amount of energy during one wave cycle as the actual nonlinear drag relationship. Equation (91) distributes the losses among the vertical and the horizontal velocity components, even though the drag force is horizontal. This step is mathematically expedient and yet the approximation may be better than completely ignoring the effect of damping on the vertical motion. The physical rationale behind this is that real fluid effects induce losses due to the vertical velocity component interacting with the wakes and eddies produced by the horizontal velocity components. Introducing equations (90) and (91) into equation (89) yields the linearized equation of motion:

$$S \frac{\partial q}{\partial t} = - \frac{1}{\rho} \nabla(p + \gamma z) - f\sigma q, \quad (92)$$

with

$$\nabla \cdot \mathbf{q} = 0.$$

c. Solving the Equation of Motion. Equation (92) is identical to the coarse-granular media equation of motion (eq. 10). One can operate on equation (92) to derive the same boundary value problem for the pile-array breakwater as that derived for the rubble-fill breakwater. Thus, the general eigen-series solution also applies to the pile-array breakwater. Similarly, the interfacial boundary conditions of horizontal mass flux and pressure continuity prescribed for the crib-style rubble-fill breakwater are equally suitable for the pile-array breakwater. Consequently, the orthogonalized boundary conditions represent a valid solution to both problems.

The two breakwater systems differ only in their internal structure. As a result, the character of the flow field retarding forces is unique to each system. However, in terms of the parameters f and S which account for these differences, the general forms of the solutions are the same. It is only necessary to revise the method for evaluating f and S in pile-array breakwaters.

The inertial coefficient is evaluated directly from equation (90). The virtual mass coefficient for circular cylinders aligned perpendicular to the flow is given by potential flow theory as $C_M = 2.0$ (Robertson, 1965). Investigations of wave forces on piles (Ippen, 1966) have related measured forces to predicted wave kinematics and determined virtual mass coefficients varying from 0.93 to 2.30. The variation is due to experimental error, approximations involved in predicting the fluid kinematics from measured wave height and period, and real fluid effects such as wakes, etc. In this study, the theoretical value of $C_M = 2$ is accepted as a reasonable approximation.

The damping coefficient, f , is solved from Lorentz's condition of equivalent work. The expression relating the energy dissipated by the linearized law to the energy dissipated by the conventional drag law is:

$$\int_0^1 dy \int_0^b dx \int_{-h}^0 dz \int_t^{t+T} \epsilon f \sigma q \cdot q dt = \int_0^1 dy \int_0^b dx \int_{-h}^0 dz \int_t^{t+T} \epsilon \frac{D}{\epsilon A_p} C_D \frac{u|u|}{2} \cdot u dt. \quad (93)$$

The two-dimensional problem is being solved so the lateral integration on the left-hand side of the equation is simply replaced by a unit width. The lateral and longitudinal integration on the right-hand side of the equation are combined by evaluating the energy dissipation at each pile in the longitudinal direction, summing and multiplying times the number of piles per unit width in the lateral direction. Thus,

$$\int_0^b dx \int_{-h}^0 dz \int_t^{t+T} \epsilon f \sigma q^2 dt = N_y A_p \sum_{j=1}^{N_x} \int_{-h}^0 dz \int_t^{t+T} \frac{C_D}{A_p} \frac{D}{2} |u_j|^3 dt, \quad (94)$$

where

N_y = number of piles per unit width per row,

A_p = the unit of horizontal surface area in the x, y integration (Fig. 13),

N_x = number of rows of piles longitudinally, and

j = the incremental row number.

The drag coefficient is a function of the approach velocity Reynolds number, and is as unsteady as the local velocity. Circular cylinder drag coefficients have been determined experimentally at various steady-flow Reynolds numbers (Schlichting, 1968). The results are shown in Figure 14. It is assumed that the drag coefficient for unsteady flows is specified by the steady-state value corresponding to the instantaneous approach velocity

Reynolds number. To account for the spatial and temporal variability of C_D in equation (94), an approximate empirical equation is fitted to the data in Figure 14. The resulting equation expressing the relationship between C_D and R_D for subcritical drag is:

$$C_D = \frac{10}{|R_D|} + 1.2, \quad (95)$$

where

$$R_D = uD/\nu.$$

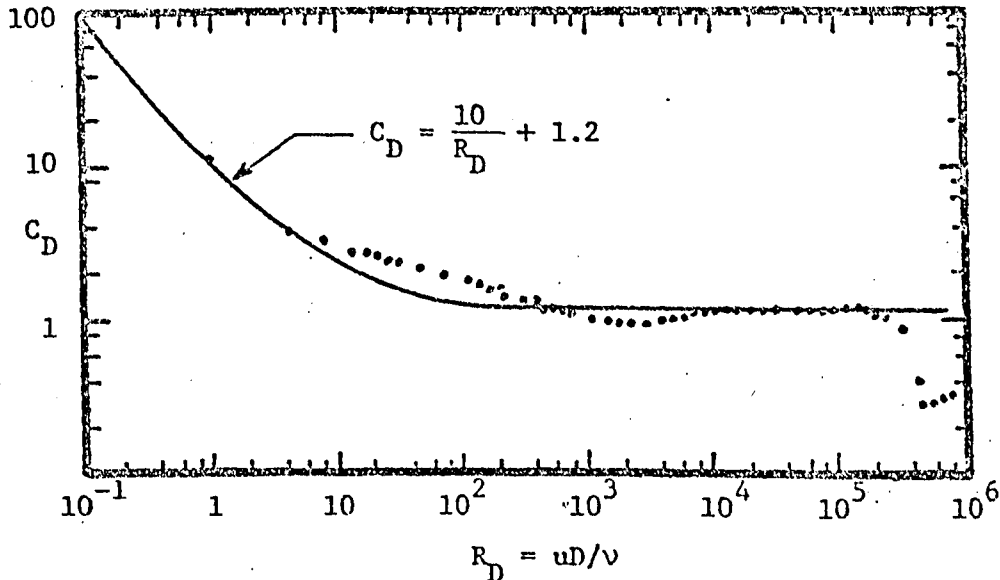


Figure 14. Drag coefficient versus Reynolds number, circular cylinder.

The equation is also plotted in Figure 14. It would be possible to improve the correlation by fitting more complicated equations to the data. However, even this simple relationship represents a significant improvement over an attempt to guess at some appropriate average constant value for C_D . It is interesting to note the similarity between the cylinder drag coefficient and the friction factor for porous media or pipe flow. Laminar, linear drag dominates at low Reynolds numbers and turbulent, square-law drag dominates at high Reynolds numbers.

Substituting equation (95) into equation (94) yields:

$$\int_0^b dx \int_{-h}^0 dz \int_t^{t+T} \epsilon f \sigma q^2 dt = N_y \sum_{j=1}^x \int_{-h}^0 dz \int_t^{t+T} (5\nu u_j^2 + 0.6D|u_j|^3) dt.$$

The temporal integration is performed as in Appendix C with the following result:

$$f\sigma = \frac{\sum_{j=1}^{N_x} \int_{-h}^0 \{ 5v(U_I^2 + U_R^2)_j + 0.6D \frac{8}{3\pi} (U_I^2 + U_R^2)_j^{\frac{3}{2}} \} dz}{\int_0^b dx \int_{-h}^0 \epsilon (Q_R^2 + Q_I^2) dz}, \quad (96)$$

where $U_I, U_R = \text{Imag.}(u), \text{Real}(u)$ and $u = q \cdot \hat{i}$.

The denominator of equation (96) is evaluated analytically as in Appendix C. The numerator is evaluated numerically, using the trapezoidal rule for the depth integration.

d. Numerical Procedures and Results. Equations (90) and (96) combined with dispersion equation (25) and the interfacial boundary conditions (eqs. 58 to 61) specify the solution to the pile-array breakwater problem. The numerical procedure used to solve these equations is identical to that outlined in Section II, 4, g. It is only necessary to revise the Lorentz calculation according to equation (96).

Because of the relatively high porosities in pile-array breakwaters, it can be anticipated from the results of Figure 8 that reflection coefficients will be low and transmission coefficients high. The effect of the virtual mass increasing the inertial coefficient is indicated in Figure 9; the reflection coefficient increases and the transmission coefficient decreases slightly.

One might expect that including the vertical-velocity component in the virtual mass and linearized drag-force calculations limit the application of the results to long-wave conditions. Comparison with available experimental data in Section IV demonstrates that this approximation also yields excellent results for short waves.

III. EXPERIMENTAL APPARATUS AND PROCEDURES

1. Introduction.

Many of the references cited in Sections I and II contain experimental data on wave reflection from and transmission through permeable structures of various composition and form. Only two of these references report of an attempt to evaluate the hydraulic properties of the material composing the experimental models. Recent studies (Dinoy, 1971) indicate that the important media hydraulic-resistance properties are the permeability and the turbulent damping coefficient identified in equation (5). As of this study, none of the published information on wave interaction

with permeable structures has evaluated these latter quantities. As a result, it was necessary to conduct additional experiments to validate the theory proposed by this study.

A description of the experimental program may be conveniently divided into four subtopics: (a) physical and hydraulic properties of the various media used in the models, (b) homogeneous rectangular breakwater models, (c) trapezoidal-layered breakwater models, and (d) wave testing facilities and procedures. Information about the apparatus and technique associated with each of these topics follows.

2. Media Properties.

a. Material Selection. The most straightforward application of the theory is for rubble-mound breakwaters. Hence, natural or crushed gravel becomes a logical choice of materials for breakwater modeling. Three different rock sizes were selected to allow some variation in the homogeneous rectangular model dimensions and to provide a reasonable gradation of material for multilayered structures. Construction-grade gravel was obtained from pits in the greater Boston, Massachusetts, area conforming to commercial sizes of 3/8, 3/4, and 1½ inches. The material is mostly igneous rock with a high percentage of fractured faces. All of the gravel is washed and graded in the laboratory and conforms to the specifications listed in Table 1. Representative samples of the gravel are shown in Figure 15.

Table 1. Media physical properties.

Commercial size (in)	Sieve tolerances		Equivalent mean sphere diameter (in)	Specific gravity	Porosity (pct)
	Retained (in)	Passing (in)			
0.375	0.25	0.50	0.325	2.70	43.0
0.75	0.50	1.0	0.774	2.67	43.9
1.5	1.0	2.0	1.37	2.68	43.4

b. Physical Properties. The gravel is sieved by hand on standardized screens according to the tolerances in Table 1. Only the 2-inch passing dimension of the large gravel was not checked in the laboratory. This latter tolerance was assured by the supplier.

The porosity is obtained by weighing a gravel sample dry and submerged, subtracting the two quantities to yield the weight of water occupying the pores, and dividing the pore water weight by the weight of water occupying the same gross volume as that of the sample. Thus, if the samples are weighed in a container of fixed volume and W_f is the net weight of the container filled with water, W_s is the net weight of the container filled with dry gravel, and W is the net weight of the container filled with gravel and water, the porosity e , is:

$$\epsilon = \frac{W - W_f}{W_s}$$

The porosities in Table 1 apply to permeameter samples measured in place.

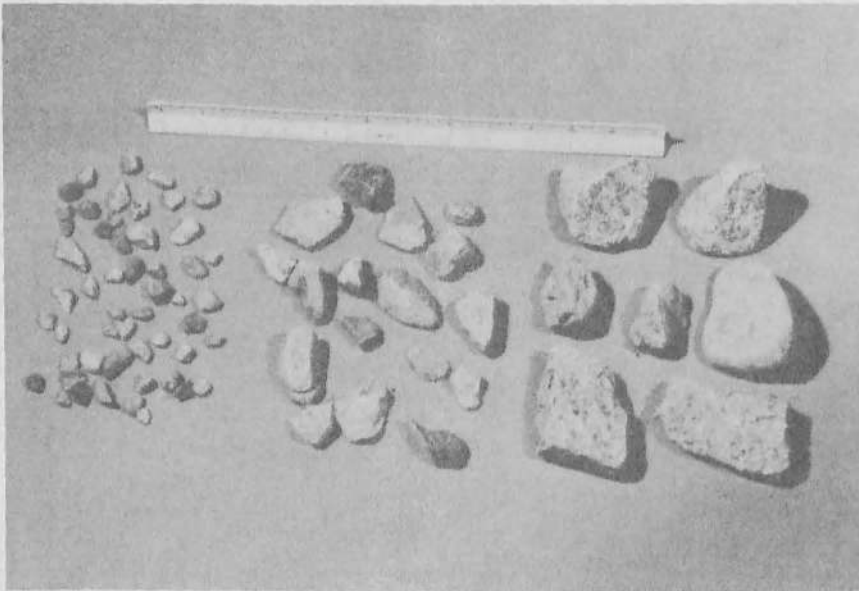


Figure 15. Media samples.

With the porosity known, the specific gravity is determined directly by dividing the dry sample weight by the weight of water occupying the same volume as that of the solids in the sample, i.e.,

$$\text{S.G.} = \frac{W_s}{(1 - \epsilon)W_f}$$

The equivalent sphere diameter is calculated by dividing the volume of solids by the number of particles in the sample and equating this to the volume of a sphere of unknown diameter. This simply requires that the equivalent sphere has the same volume as the mean particle volume. Thus, if γ is the weight density of water, N is the number of particles in the sample, then the equivalent sphere diameter, d , may be solved from:

$$\frac{\pi d^3}{6} = \frac{W_s}{N(\text{S.G.})\gamma}$$

Care is taken to remove air bubbles from the pores before the submerged weight measurements are performed. The dry weights are determined after the sample has air dried for a few days.

c. Hydraulic Properties. The important media hydraulic properties are the permeability, K_p , which governs low Reynolds number damping, and the turbulent damping coefficient, C_f , which governs high Reynolds number damping. These quantities are evaluated experimentally by measuring the pressure gradient through a sample of media as a function of an imposed discharge velocity. Then, K_p and C_f are solved via equation (5) in terms of the measured quantities.

A large permeameter was constructed to facilitate these measurements. The permeameter basically consists of an 8-inch vertical standpipe with a circular weir at the top and a gradual contraction on the bottom (Fig. 16). The device is supported on a 5-inch, 90° elbow with a structural foot. About 4 feet of the standpipe forms the test section wherein the media sample is contained. The sample is restrained at the bottom of the standpipe by a stainless-steel screen which is held fast between the flange gaskets. The gravel is also restrained at the top with a second stainless-steel screen which in turn is held in place by a vertical, threaded compression member. The upper screen keeps the sample consolidated over the full range of flow rates.

The flow proceeds vertically upward through the sample. This direction is most effective for washing air bubbles out of the interstices of the media. The supply line runs through a heat exchanger so that water temperatures are maintained constant within $\pm 1^\circ$ Fahrenheit for any experimental run. The flow rate is measured on a weigh scale and temperature corrections are included in the density as well as viscosity calculations. Pressures are monitored at the four elevations (Fig. 16). Each pressure reading represents a circumferential average of four taps, spaced at 90° around the perimeter of the standpipe.

The experimental data is given in reduced form in Appendix F, i.e., the pressure readings are presented as the average head gradients across the four tap elevations, the flow rates are presented as discharge velocities, and the viscosities are adjusted to reflect temperature corrections. All notations are as previously defined, except for $-\Delta h/\Delta l$, which represents the gradient in the pressure head.

The specific technique used in the data reduction is adopted from Dinoy (1971). Briefly, equation (5) is modified by dividing through by vq_d to obtain:

$$-\frac{1}{vq_d} \frac{1}{\rho} \nabla(p + \gamma z) = \frac{1}{K_p} + \frac{C_f}{vK_p^{1/2}} |q_d|.$$

Letting

$$\frac{1}{\rho g} \nabla(p + \gamma z) = \frac{\Delta h}{\Delta l},$$

the total head gradient, the above equation becomes:

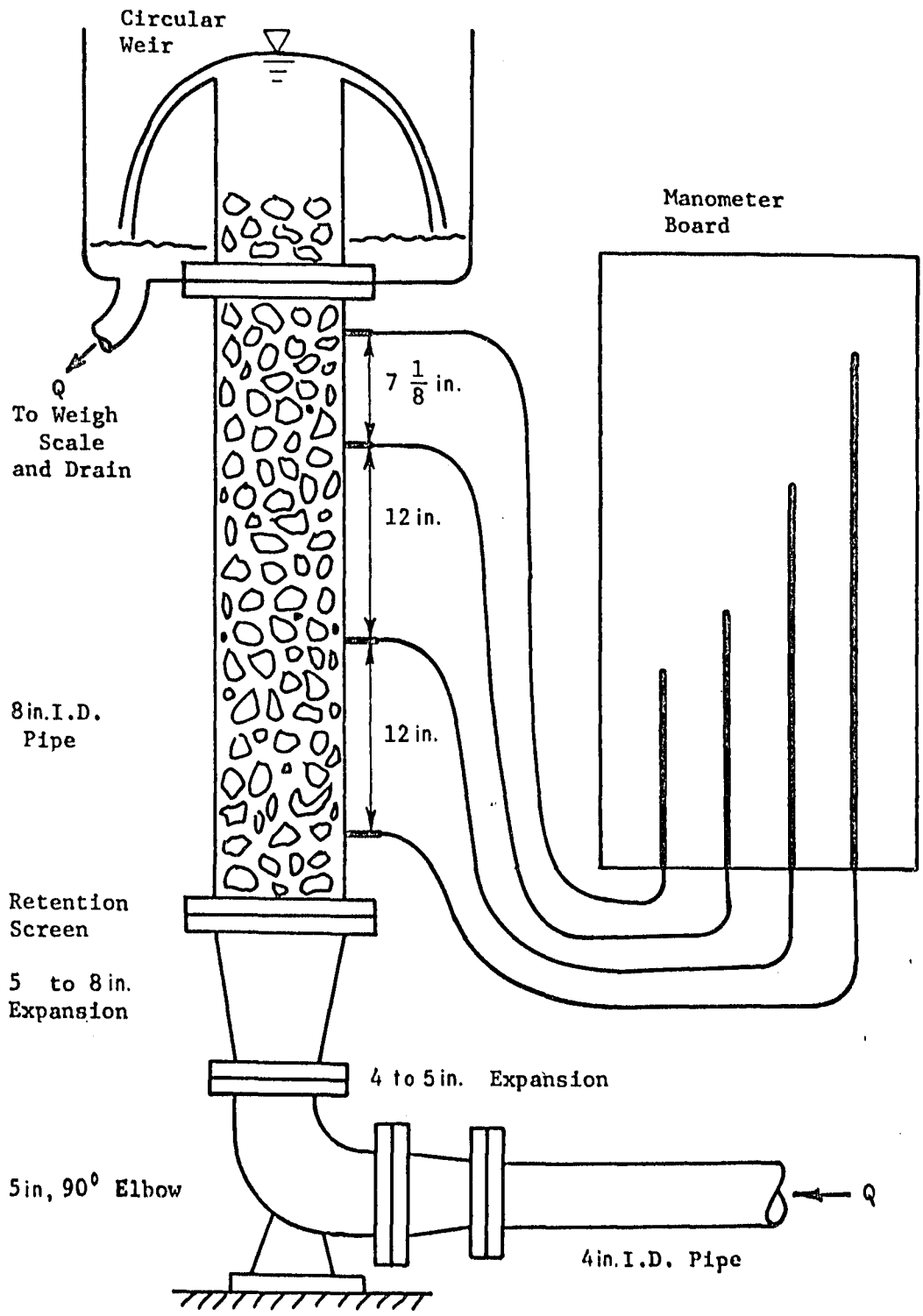


Figure 16. Permeameter.

$$-\frac{1}{v q_d} g \frac{\Delta h}{\Delta l} = \frac{1}{K_p} + \frac{C_f}{K_p^{1/2}} \frac{q_d}{v}$$

Now let the left-hand side of the equation be referred to as K_{po} , the permeability resulting from applying Darcy's Law at any Reynolds number. Then,

$$\frac{1}{K_{po}} = \frac{1}{K_p} + \frac{C_f}{K_p^{1/2}} \frac{q_d}{v},$$

where the absolute value signs have been dropped from q_d because the flow is unidirectional in the permeameter. C_f and K_p are constants for any particular medium; consequently, plotting $1/K_{po}$ versus q_d/v should produce a straight line. The value of the intercept at $q_d/v = 0$ is simply the reciprocal of the true permeability, K_p .

The seventh column in the tabulation of Appendix F evaluates $1/K_{po}$ for the various q_d/v . A least-squares computer program is used to fit a straight line through the data and extrapolate the value of $1/K_p$ at $q_d/v = 0$. The resulting value of K_p is listed at the bottom of the eighth column in each table. Once K_p is known, the permeability Reynolds number may be evaluated directly from:

$$R_{K_p} = \frac{K_p^{1/2} q_d}{v},$$

and the friction factor, f_{K_p} , is solved from equation (5) as:

$$f_{K_p} = \frac{g K_p^{1/2} \frac{\Delta h}{\Delta l}}{2 q_d}.$$

Then equation (6) yields the turbulent damping coefficient:

$$C_f = f_{K_p} - \frac{1}{R_{K_p}}.$$

The last three columns in the tabulation of Appendix F evaluate these quantities in order. The mean value of C_f , listed at the bottom of the last column, is accepted as a representative value for the medium.

There is some scatter in the value of C_f , especially at low Reynolds numbers. This is a result of experimental errors attributed

to the difficulty of discerning small pressure losses at low flow rates. Pressure fluctuations in the supply line compound this difficulty. These same errors weigh heavily on the slope intercept method for evaluating K_p . Nevertheless, the technique is sound and gives good correlation between experiment and theory for the friction factor (Fig. 17). Note that the damping does indeed become pure Darcian at low Reynolds numbers and fully turbulent at high Reynolds numbers.

No corrections have been made for permeameter wall effects. Dudgeon (1967) reports that the resulting errors are 10 percent or less, but does not provide a satisfactory method for making numerical corrections. In this study, the effect is accepted as within the range of experimental and data reduction errors.

A summary of the hydraulic properties are given in Table 2.

Table 2. Media hydraulic properties.

Commercial size	Equivalent sphere diameter	Permeability	Turbulent damping coefficient
(in)	d (in)	K_p (ft ²)	C_f (dimensionless)
0.375	0.325	$3.74 \cdot 10^{-7}$	0.406
0.75	0.774	$1.138 \cdot 10^{-6}$	0.295
1.5	1.37	$8.638 \cdot 10^{-6}$	0.390

3. Homogeneous Rectangular Breakwater.

Model Descriptions. Tests on two different gravel-filled structures are presented in detail. The model dimensions are scaled in accordance with the requirements of a separate study on scale effects (Wilson, 1971). As a result, the model widths, the water depths, and the gravel sizes all bear the same ratio. The physical dimensions of the two models are described in Table 3.

Table 3. Model dimensions.

Gravel size (d)	0.774 in	1.37 in
Breakwater width (b)	12.0 in	21.6 in
height	18.44 in	32.13 in
breadth	29.75 in	29.75 in
weight	373.2 lb	1,126.5 lb
<i>In Situ</i> porosity (ϵ)	0.411	0.437
Water depth (h)	12.0 in	21.6 in

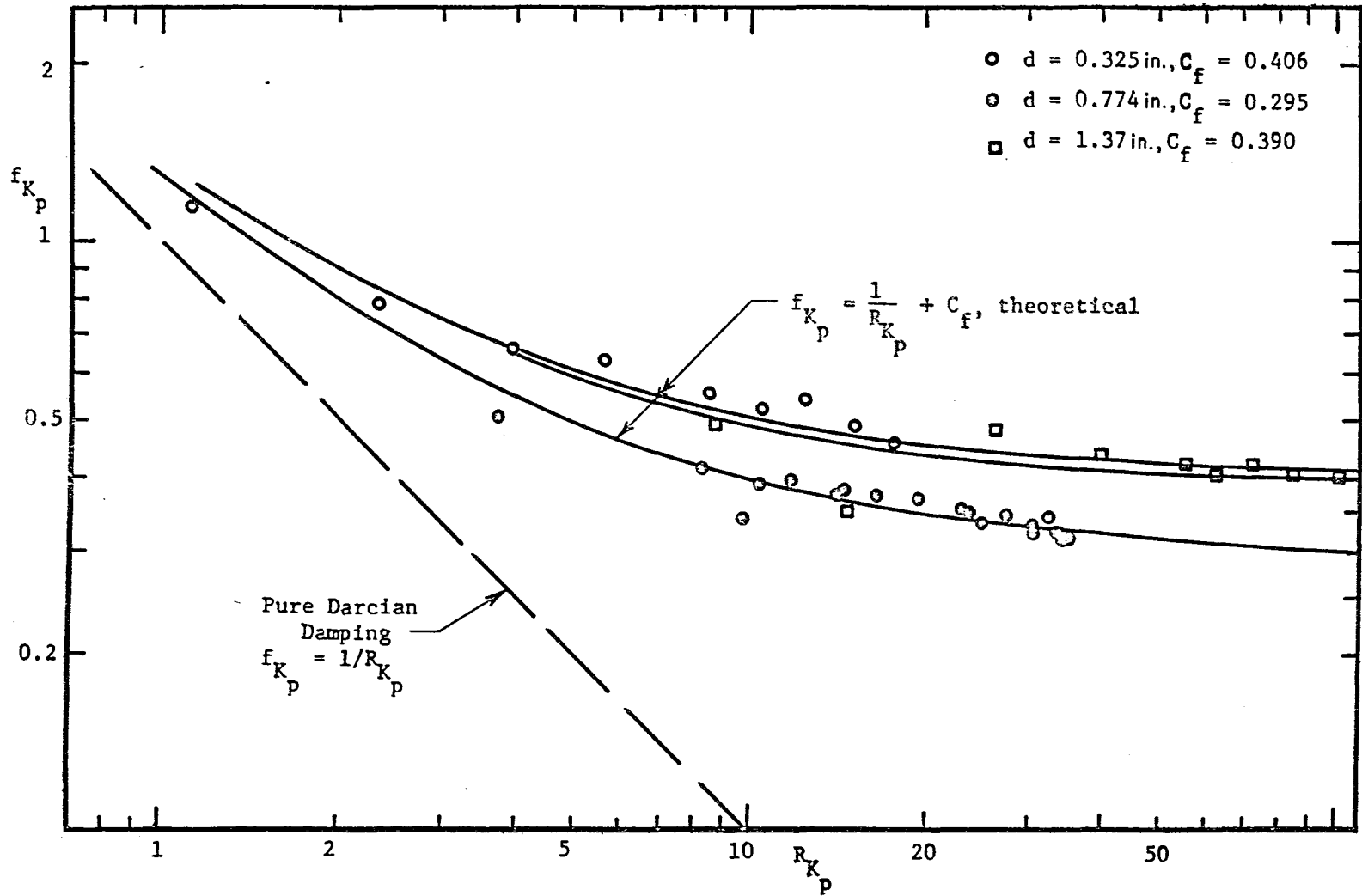


Figure 17. Friction factor versus Reynolds number.

The gravel is contained in wire-screen cribs, shaped as rectangular parallelepipeds. The screen is constructed of 0.05-inch galvanized wire spaced at 0.5 inch on center. The shape and structural integrity of the crib is reinforced with 0.05-inch cross wires spaced at 3 to 4 inches on center between the two vertical breakwater faces. The cribs are filled in the wave tank by pouring small quantities of gravel in a random fashion. However, the gravel level is increased uniformly and care is taken to avoid oversized pores near corners and around cross wires.

The breadth of the models is limited by the 30-inch lateral dimension of the wave tank. Consequently, the wire cribs are 29.75 inches across and 1/8-inch Lucite sheets are used to fill the remaining gap between the wave tank walls and the sides of model. The model heights are sufficient to prevent overtopping by the highest waves. The dry gravel weights, gross crib volumes and previously determined specific gravities (Table 1) are combined to calculate the *in situ* breakwater porosities. The resulting values are quite close to the permeameter sample porosities in Table 1.

The large and small models are placed on 1/4- and 1/8-inch-thick plywood sheets, respectively, to prevent concentrated point loads on the glass bottom wave tank. The wire crib and interlocking gravel combine to make an extremely rigid structure. The rigidity and bulk weight of the models overcome any tendency to flex or slip under the action of even the highest waves. Photos of each model are shown in Figure 18.

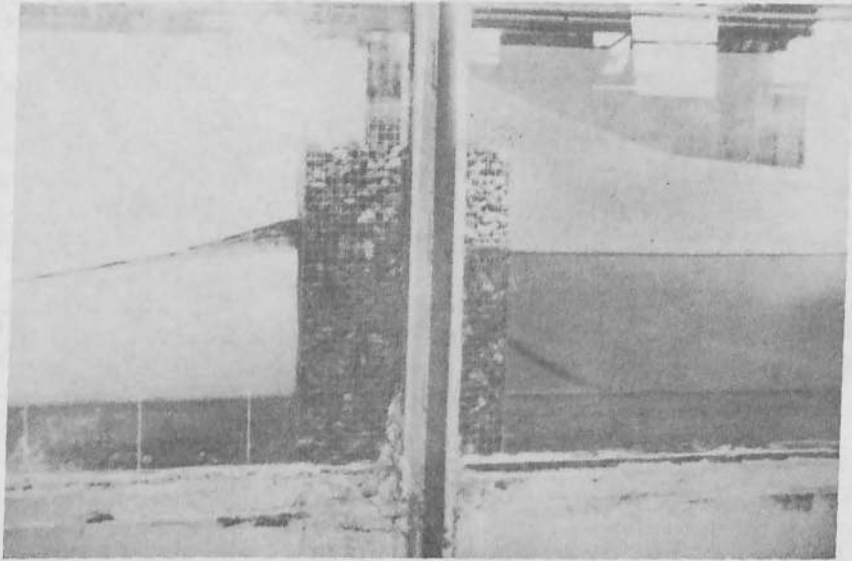
4. Trapezoidal-Layered Breakwater.

Model Description. The sloping-face breakwater design optimizes the laboratory wave-generating capabilities with the size and quantity of available rock. The configuration is of the deepwater variety, wherein the armor layer extends approximately two-thirds of the distance to the toe. The design dimensions are shown in Figure 19.

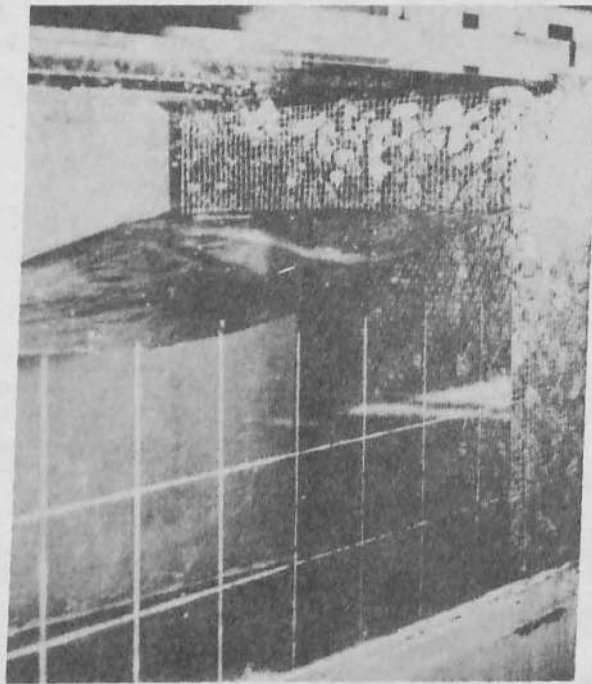
The three-layered structure is composed of the gravel materials whose properties are given in Tables 1 and 2. The 3/8-inch gravel is used for the mat and core. The intermediate layer is constructed of 3/4-inch gravel. The 1½-inch gravel forms the armor layer.

The actual construction is performed by hand. Dry rock is poured in place from a 1-quart container. The layers are screeded and compacted lightly with a 29-inch-long 2 by 4. Each layer is completed before moving on to the next. A 1/8-inch-thick piece of masonite, 30 by 66 inches, is placed underneath the breakwater to prevent concentrated point loadings on the plate glass tank bottom.

In situ porosities are determined from the weight, volume, and specific gravity of each layer. The calculated porosities for 3/8-, 3/4-, and 1½-inch gravel are 0.440, 0.432, and 0.414, respectively. Note that these results are within 2 percent of the porosities determined for the permeameter samples in Table 1.



$b = 12 \text{ in.}$



$b = 21.6 \text{ in.}$

Figure 18. Rectangular homogeneous crib-style breakwater.

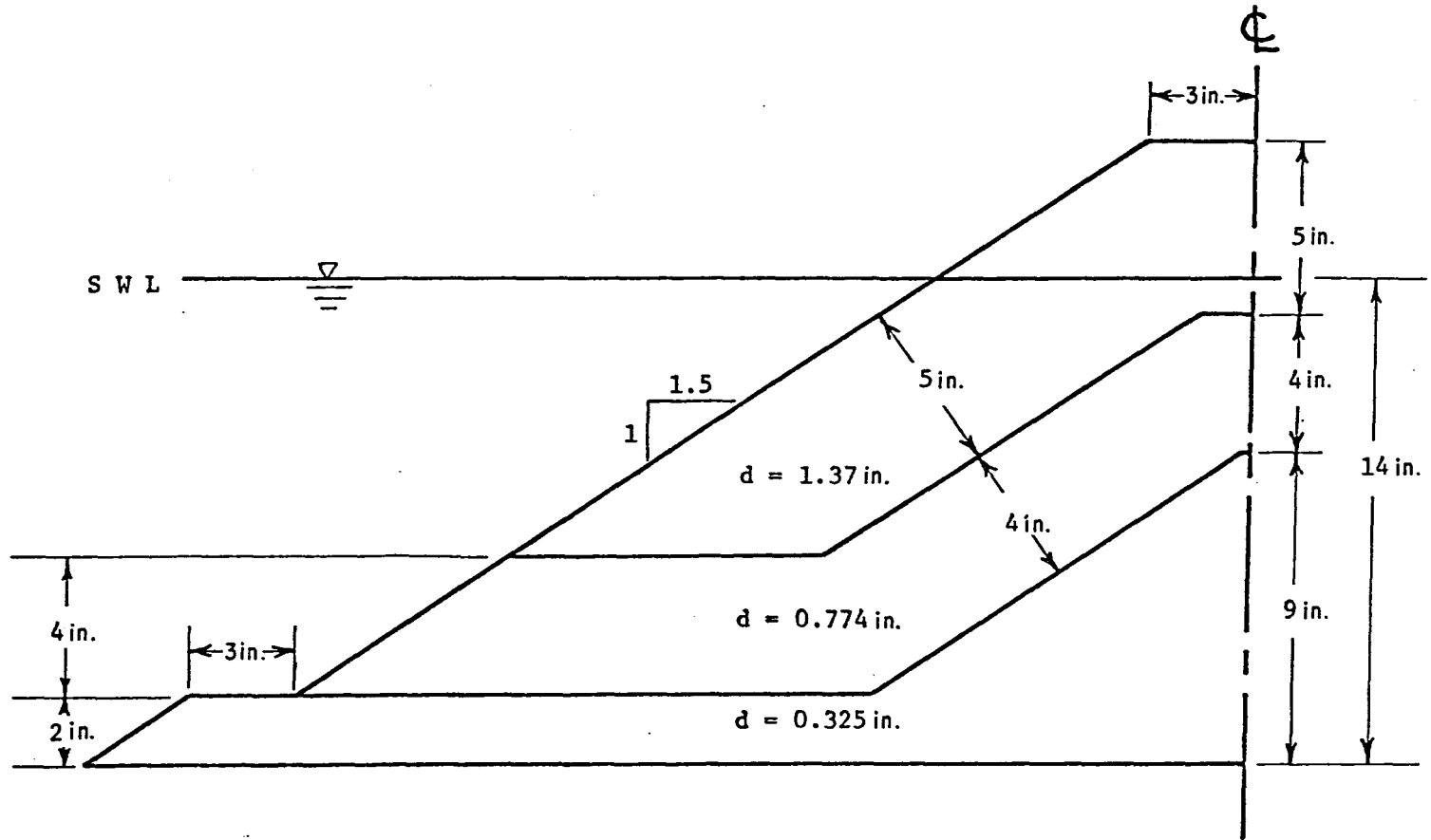


Figure 19. Trapezoidal-layered breakwater.

The exterior face and each layer are sloped at 1.5:1. This is a stable slope for the nonovertopping wave conditions imposed in this study. Photos of the completed breakwater model are shown in Figure 20.

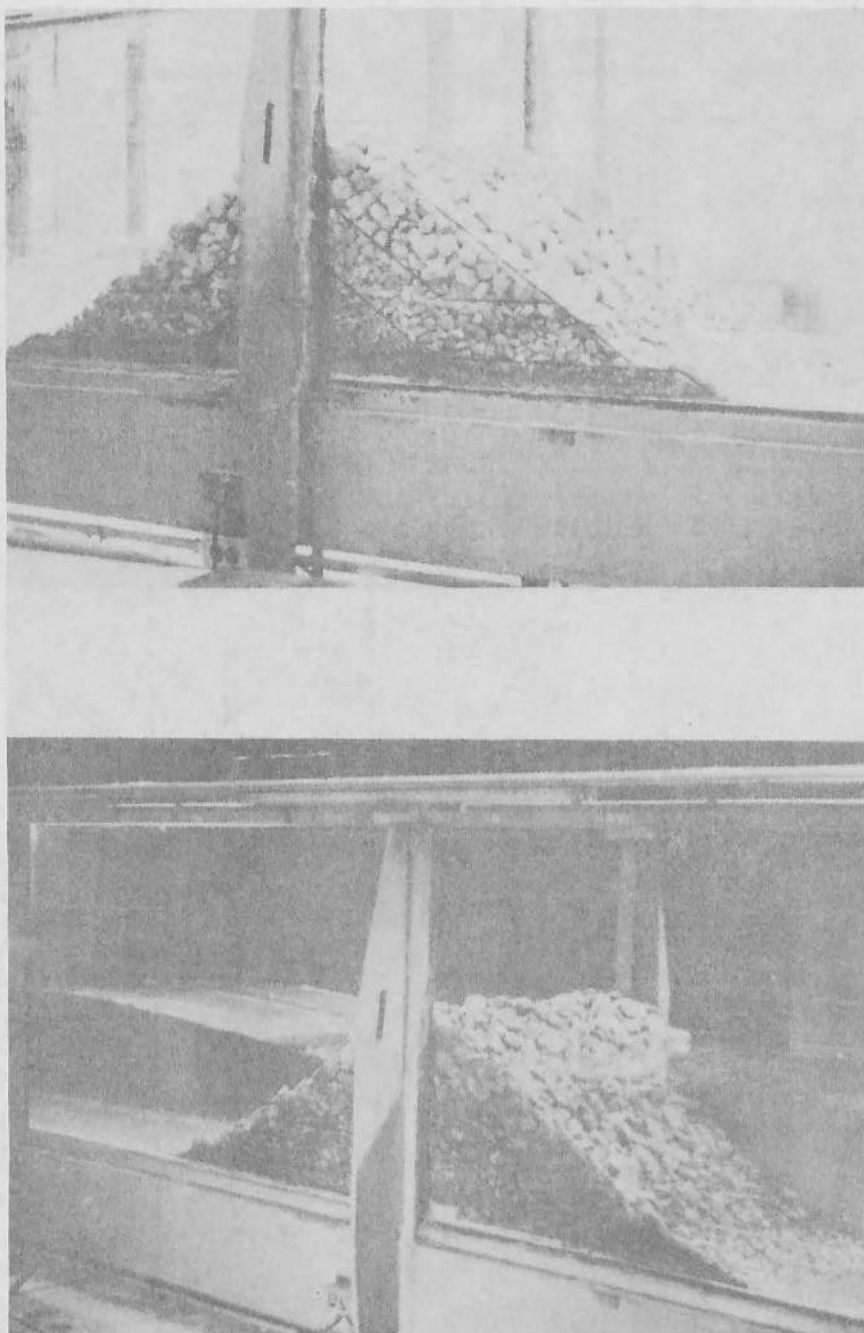


Figure 20. Trapezoidal-layered breakwater model.

5. Wave Testing Facilities and Procedures.

a. General Equipment Description. The wave experiments were conducted at the Ralph M. Parsons Laboratory for Water Resources and Hydrodynamics, Massachusetts Institute of Technology (MIT). The wave tank is of rectangular cross section with glass walls and bottom supported on a structural steel frame. The test section (Fig. 21) extends 90 feet from the wave generator to the crest of the beach and is 30 inches wide by 34 inches deep. The plywood beach is sloped at 1:10 and is covered with 2 inches of rubberized horsehair to reduce wave reflection. A wave filter constructed of parallel sheets of expanded aluminum lath is placed in front of the generator to reduce surface ripples and smooth the overall profile of the incident wave.

The wave generator is of the hinged-flap variety with a continuously variable stoke and frequency. Power is provided by a 1.5-horsepower Master Speedranger variable-speed drive unit. V-belts couple this unit to a pulley and shaft. The shaft is keyed to a 12-inch diameter, ½-inch-thick steel drive wheel. Power is transmitted to the generator plate via a 2-foot-long stainless-steel connecting rod. The rod is pinned to both the drive wheel and the generator plate. The eccentricity of the drive-wheel pin is continuously variable from 0 to 4 inches. The aluminum generator plate is hinged at the bottom and measures 30 by 32 by 3/8 inches. The plate normally oscillates about a mean vertical position. However, to generate long waves of appreciable amplitude it is necessary to operate the plate about a mean angle of approximately 35° to the horizontal. This position effectively increases the submerged surface area of the plate and, for a given angle of rotation, the displaced volume of fluid increases accordingly. In either position, the resulting wave profiles are acceptably uniform beyond the wave filter.

Wave conditions are monitored by two resistance-type wave gages mounted on moving carriages. The gages are constructed from two 1/8-inch-diameter uncoated stainless-steel rods separated by a distance of 1 inch and mounted in insulating acrylic blocks. An input signal to each gage is provided by the oscillator section of a Sanborn Model 350-1100 C pre-amplifier. Each gage acts as an additional variable resistor in a Wheatstone bridge circuit. When the gage is partially immersed in water, the circuit is completed and the flow of current across the wires is proportional to the immersed depth. The signal is returned to the Sanborn instrument, amplified, and recorded on a twin-channel Sanborn oscillograph Model 77-12 B.

b. Procedures. The gages are calibrated statically by immersing each gage in a vertical position to a known depth and recording the immersed depth as a function of the oscillograph pen deflection. The response is linear within 5 percent for all sensitivity ranges used in conjunction with this study. Wiegel (1955) conducted extensive dynamic tests on resistance-type wave gages and concluded that the estimated error of the wave gage and recording system is ± 5 percent.

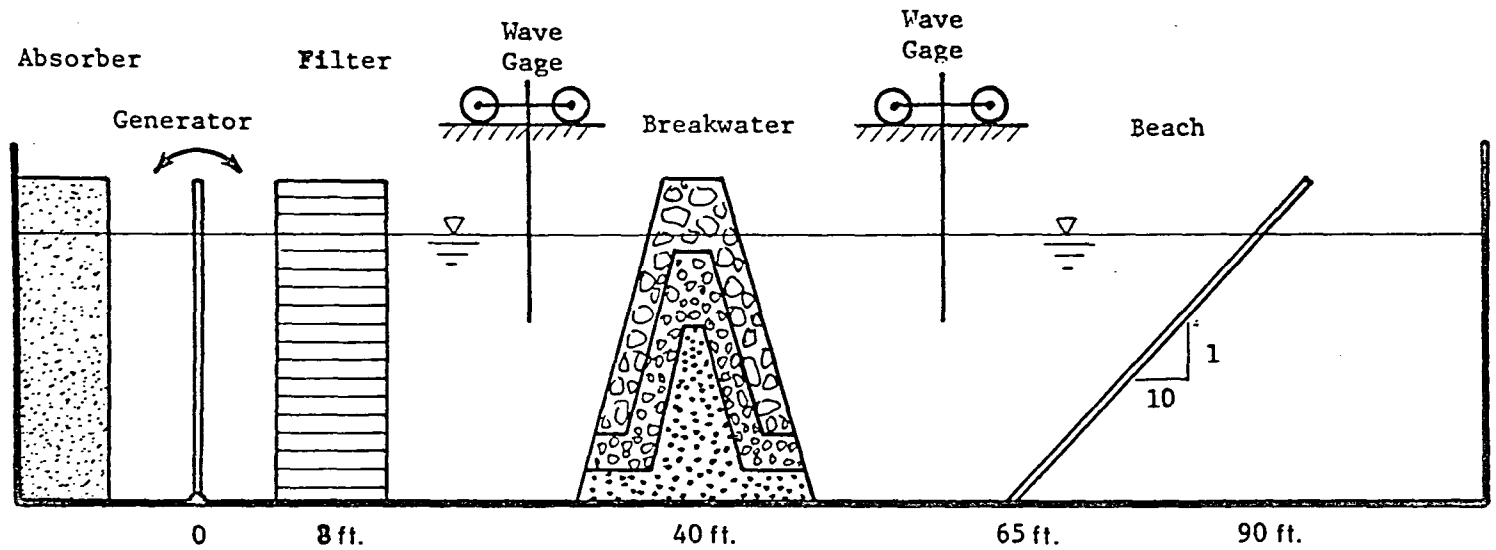


Figure 21. Wave testing facility.

The wave gages are brushed clean with steel wool and wiped with a highly volatile solvent before each day's test. The calibration is checked at the end of each test. Recalibrations have proven to be unnecessary due to the stability of the Sanborn unit.

It has been observed in this study that reflections from permeable breakwaters result in a change in wave amplitude and phase but not frequency. Consequently, the superposition of incident and reflected waves yields a partial standing wave. The standing-wave envelope profile does not propagate relative to a fixed reference system. It merely oscillates in one place. If such a profile is to be measured, a wave gage must be moved perpendicular to the crestline to record the amplitudes of the oscillations at successive positions. Using this method, one will find relative maxima and minima every quarter wavelength in the standing-wave envelope. The maxima occur where the incident and reflected wave crests superimpose to yield a surface elevation equal to the sum of the two amplitudes. At the same point, one-half period later, the troughs superimpose to yield a maximum surface depression. The minima occur where the incident and reflected waves interfere, i.e., the reflected trough subtracts from the incident crest to yield a minimum envelope surface elevation. Likewise, one-half period later, the incident trough subtracts from the reflected crest to yield a minimum envelope surface depression. By moving the wave gage, the investigator is able to locate and record these maxima and minima and the resulting record appears as in Figure 22. Linear wave theory allows one to solve directly for the incident and reflected wave heights because:

$$H_{\max} = (a_i + a_r) + (a_i + a_r) = 2(a_i + a_r),$$

$$H_{\min} = (a_i - a_r) - (a_r - a_i) = 2(a_i - a_r).$$

Hence,

$$H_i = 2a_i = \frac{H_{\max} + H_{\min}}{2} \quad (97)$$

and

$$C_R = \frac{a_r}{a_i} = \frac{H_{\max} - H_{\min}}{H_{\max} + H_{\min}} \quad (98)$$

This same method is used to separate the transmitted wave component from any partial reflections off the beach. The beach reflections are typically of the order 3 to 4 percent, always less than 7 percent, and are therefore usually ignored.

The general technique used in this study for measuring wave envelopes is to record H_{\max} and H_{\min} at several positions along the wave tank

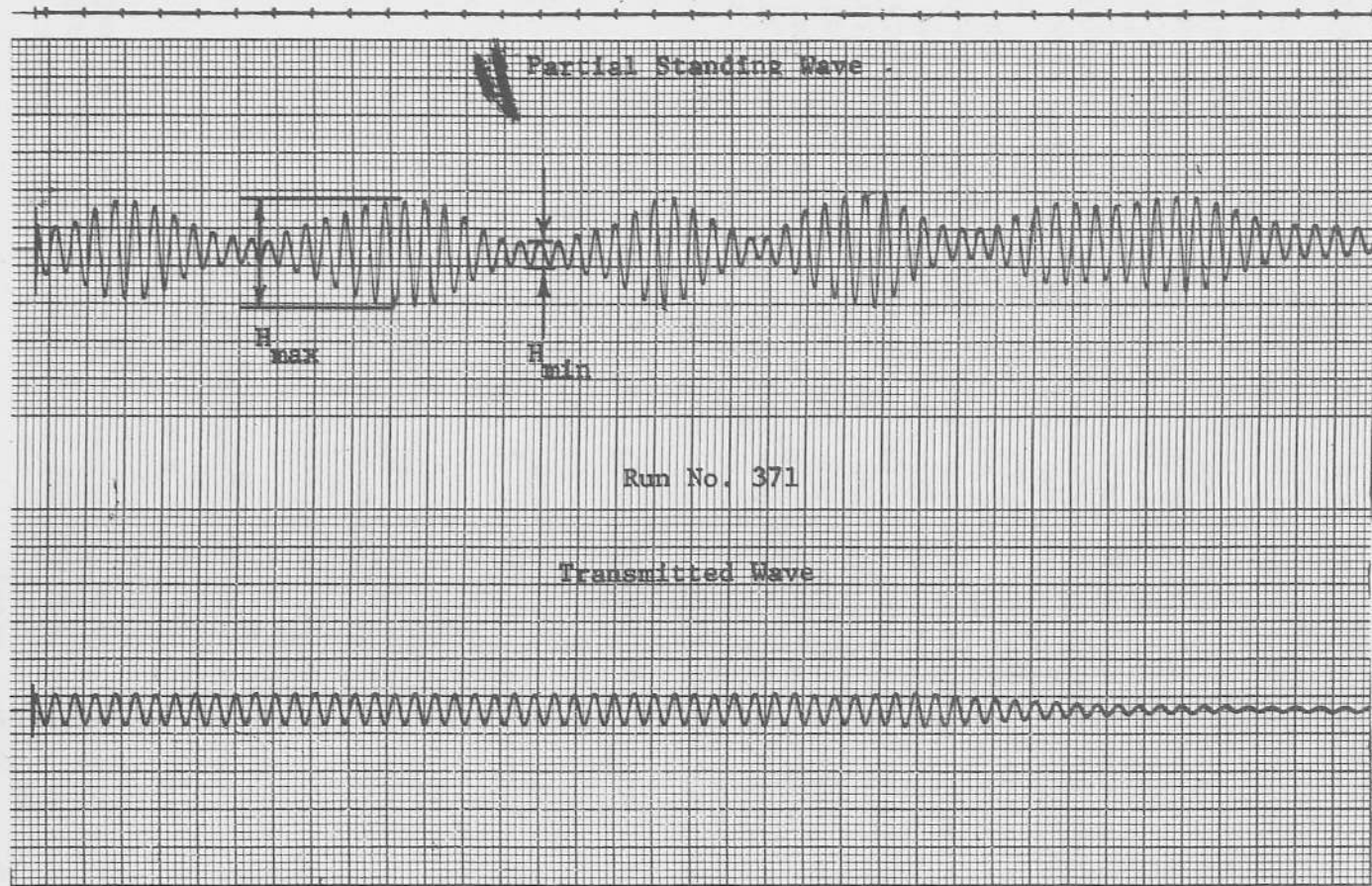


Figure 22. Partial standing wave record.

and use the average values in determining the incident and reflected wave heights. It is the usual practice to avoid the region immediately adjacent to the breakwater where local modes disorder the free surface.

The resistance wave probes are sensitive to any highly conductive material which interferes with the electric field near the probe. This problem manifests itself as an imbalance in the output signal. The difficulty is overcome by laying ground wires along the tank bottom centerline and by additional grounding of the wave filter and breakwater crib.

The test section of the wave tank is moderately short so that waves reflected off the breakwater face return to the wave generator and superimpose with the incident wave before the measurements can be completed. However, with each traverse of the test section the wave amplitude is dampened and reduced as it passes through the wave filter and is further reduced due to partial transmission into the breakwater. Consequently, after propagating back and forth a number of times, the original amplitude of any single wave component is reduced to a negligible level. Then a steady-state situation is attained where the energy fed into the system by the wave generator is equal to that absorbed by the filter and transmitted into the breakwater. When this state has been attained, all wave components propagating towards the breakwater superimpose to yield the incident wave and all wave components propagating towards the wave generator superimpose to yield the reflected wave. The steady state is typically achieved after three or four traverses of the test section, and is readily identified when the partial standing-wave envelope remains uniform. Then the standard techniques discussed above are used to determine the resulting incident, reflected, and transmitted wave amplitudes.

IV. EXPERIMENTAL AND THEORETICAL RESULTS

1. Introduction.

The results of the theory formulated in Section II and the experimental program described in Section III are summarized in this section. The behavior of the predicted and measured results are compared and evaluated. Application of the analysis to prototype conditions is also discussed.

The governing independent dimensionless parameters have been identified as b/h , ϵ , kh , and f . The damping coefficient, f , evaluated via the equivalent work, principle contains the dependence on wave steepness and media properties. For a given breakwater configuration b/h , ϵ and the media properties are fixed. Consequently, the wave steepness, H_i/L , and the dimensionless wave number, kh , constitute the two remaining degrees of freedom which can be varied to evaluate the breakwater performance.

The reflection and transmission coefficients are presented (in figures) as functions of the wave steepness for a range of wave numbers. Experimental and theoretical results are given for four breakwater configurations: two homogeneous crib-style structures, one trapezoidal-layered structure, and one pile-array structure.

2. Homogeneous Crib-Style Breakwaters.

a. Experimental Results. The wave reflection and transmission data are collected using the procedures described in Section III, 5, b. All of the data are tabulated in Wilson (1971). Small- and large-model dimensions are given in Table 3.

Changes in the incident wave height and wavelength in the small-model tests are initiated by setting the drive-wheel pin at discrete eccentricities and varying the generator frequency over a broad bandwidth. This technique leads to a great variety in incident wave numbers and wave steepness, but it precludes presentation of wave data for constant values of the wave number. As a result, the reflection and transmission coefficients are presented as functions of the wave steepness for finite ranges in the wave number. That is, a median value of kh is selected and all data within ± 0.25 of the value are plotted on the same graph.

Figures 23 to 27 present the experimental reflection and transmission coefficients as a function of wave steepness for relatively constant values of the dimensionless wave number (or relative depth). The graphs show that the transmission coefficient is strongly dependent on the incident wave steepness. As predicted by the simple form of the long-wave solution, the transmission coefficient tends to decrease with increasing wave steepness. The reflection coefficient, on the other hand, is relatively insensitive to changes in wave steepness. One would expect the structure to be more impervious to steeper waves due to increased flow resistance in the pores of the granular fill. However, the reflected wave is also partially attenuated due to the roughness of the reflecting surface. This latter effect appears to be sufficient to compensate for the expected increase in the reflection coefficient.

The dependence on wave number becomes apparent when the six figures are compared with each other. In general, there appears to be a decrease in both the reflection and transmission coefficient for shorter wavelengths. This behavior is clearly visible in Figure 28 where the reflection and transmission coefficients are plotted as a function of wave number for a constant wave steepness, $H_i/L = 0.01 \pm 0.002$. A relative maximum in each coefficient appears near $kh \approx 1.0$. This is probably due to a trade-off between increasing wave height and increasing wavelength as kh decreases and H_i/L remains constant. Increasing wavelength makes the breakwater appear to be more transparent (thereby decreasing C_R) while increasing wave height causes the damping to be more severe (thereby decreasing C_T). At high wave numbers, the relative roughness of the windward face reduces the reflection coefficient and the high frequencies promote severe internal damping so that C_T decreases.

Wave conditions in the large-model tests are controlled in the reverse order of the procedure used in the small-model tests. In particular, the generator frequency is set at discrete values while the eccentricity of

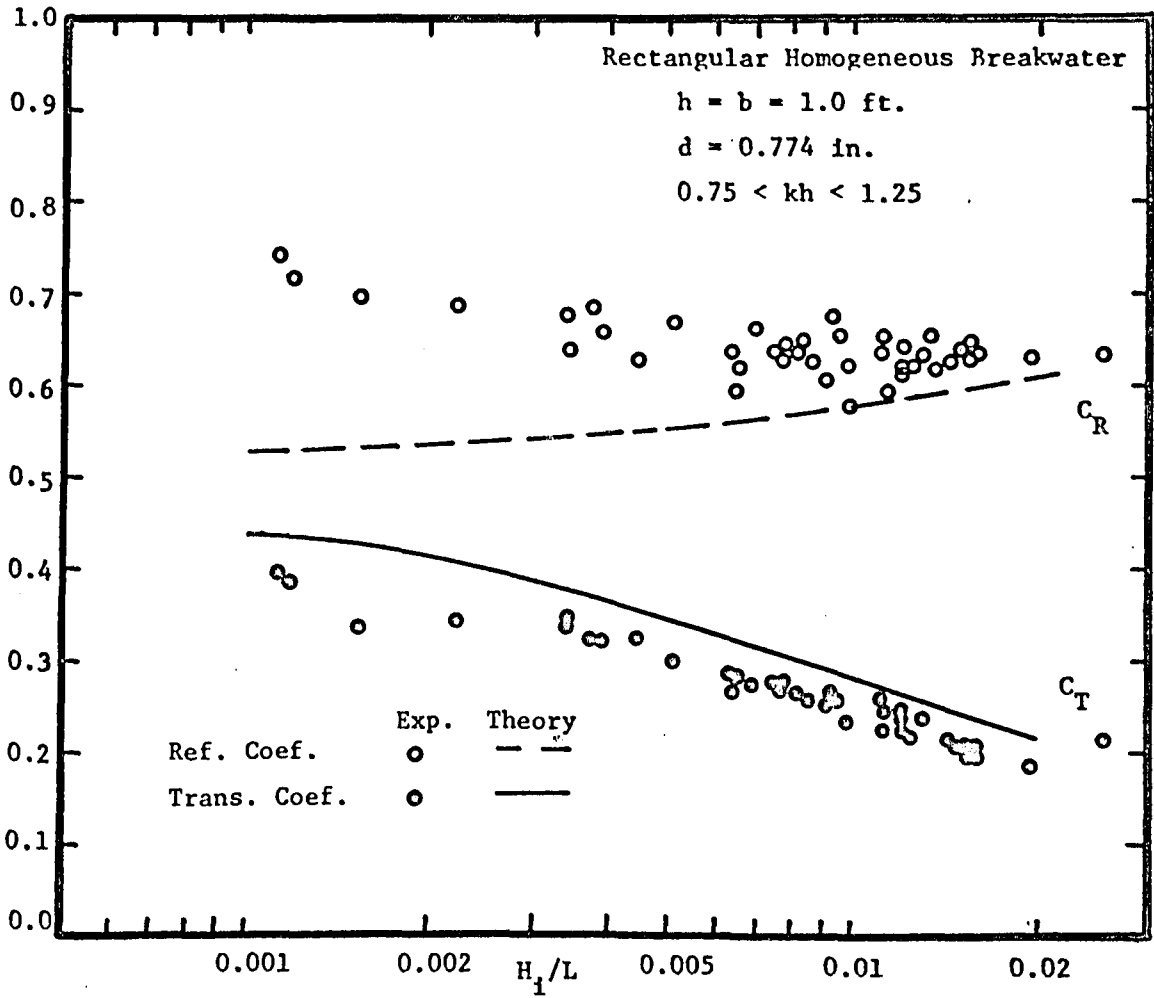


Figure 24. Reflection and transmission coefficient dependence on wave steepness.

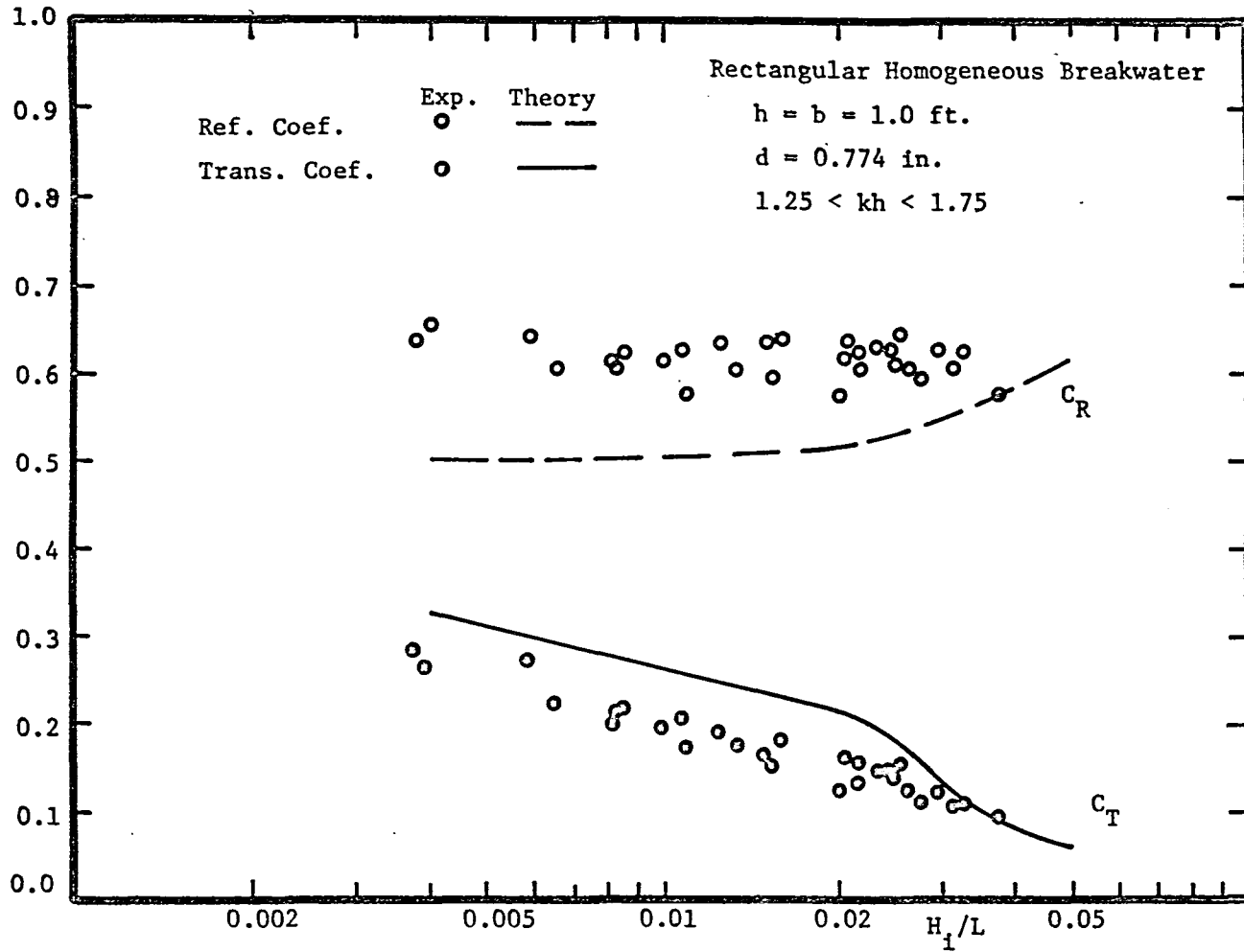


Figure 25. Reflection and transmission coefficient dependence on wave steepness.

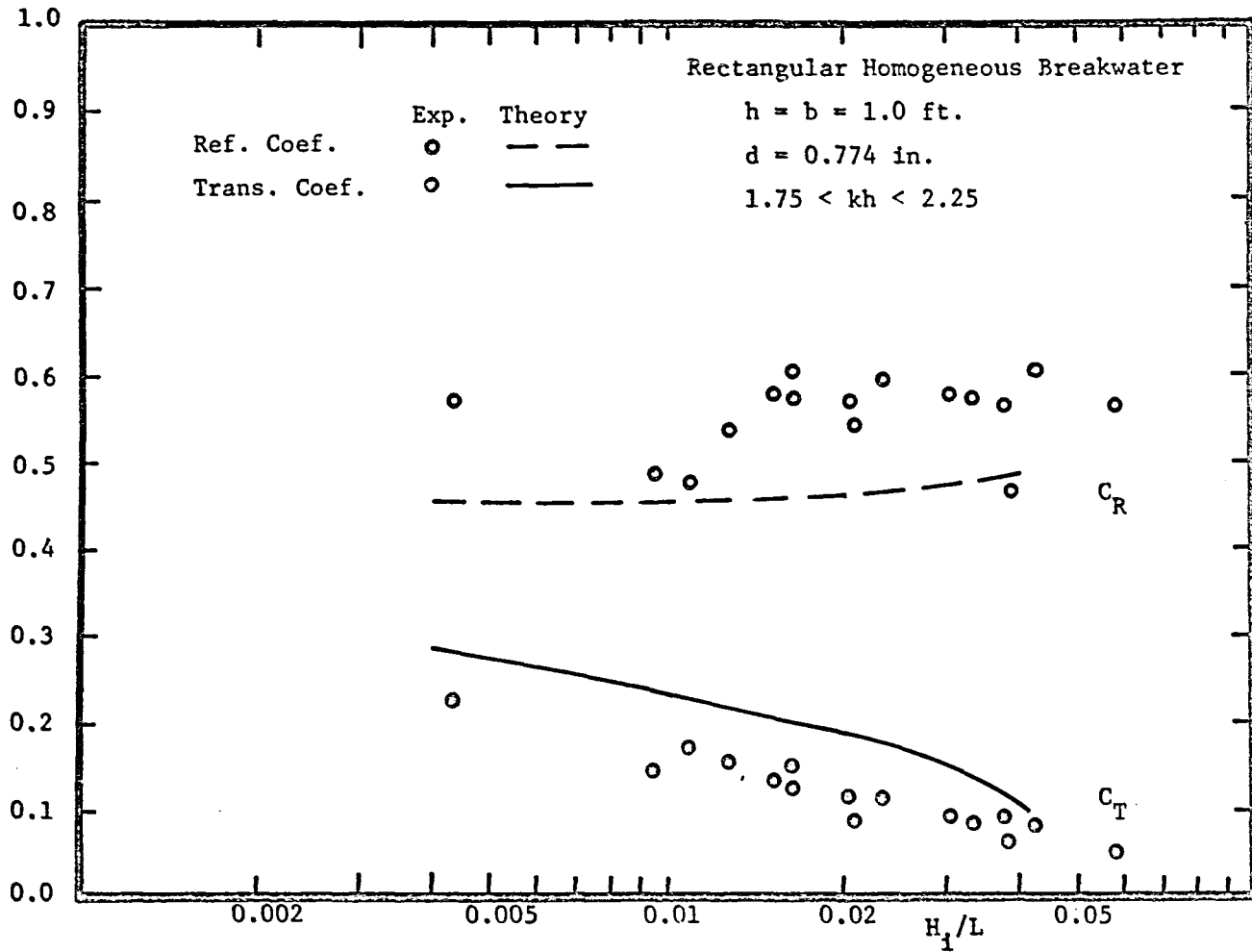


Figure 26. Reflection and transmission coefficient dependence on wave steepness.

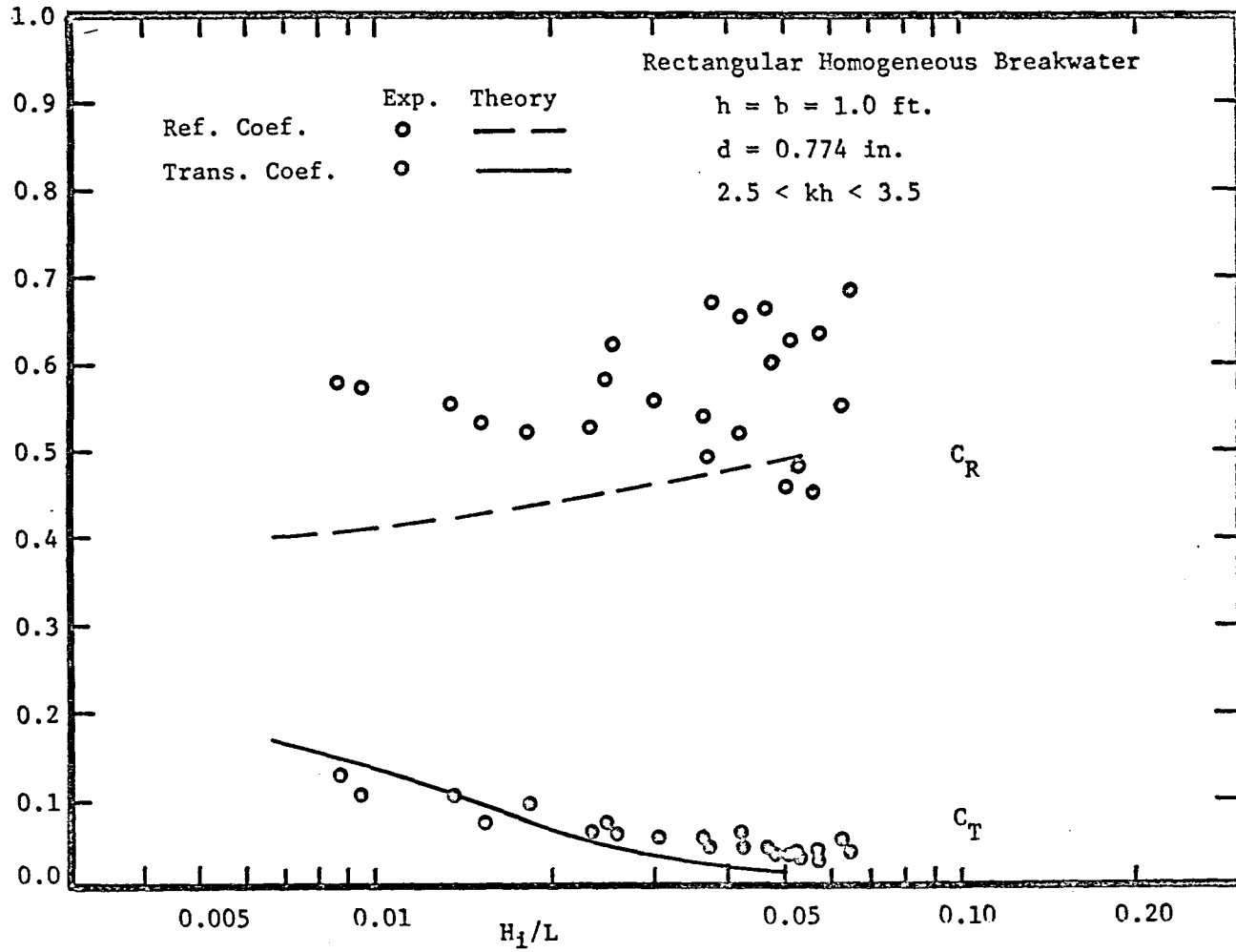


Figure 27. Reflection and transmission coefficient dependence on wave steepness.

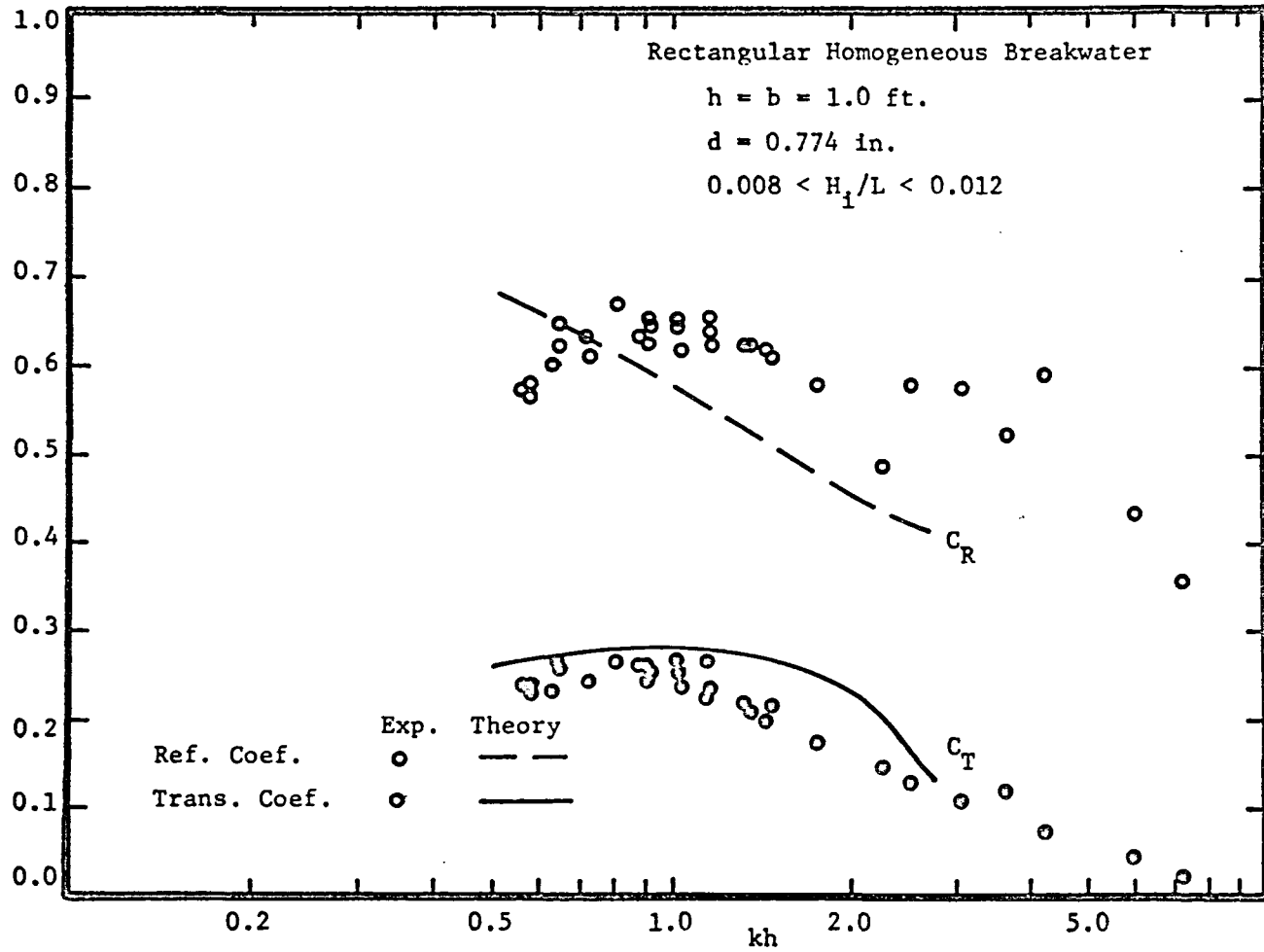


Figure 28. Reflection and transmission coefficient dependence on wave number.

the drive-wheel pin is varied. This produces variable wave steepness for constant values of the wave number, a desirable condition for graphical presentation of the data.

The large-model reflection and transmission coefficients are plotted as a function of wave steepness for five constant wave numbers in Figures 29 to 33. The results exhibit the same basic trends demonstrated in the small-model tests: transmission coefficients decrease with increasing wave steepness and wave number; reflection coefficients are relatively constant with respect to wave steepness but decrease with increasing wave number. Figure 34 shows the effect of changing wave number while maintaining wave steepness at $H_1/L = 0.01$. Again, relative maxima occur near $kh = 1.0$, as in the small model, with decreasing reflection and transmission coefficients for both large and small kh .

b. Comparison of Experimental and Theoretical Results. Theoretical solutions are also plotted in Figures 23 to 34, and are obtained for a five-term eigen series. The spatial integration in the numerator of the Lorentz equation is performed numerically using a 10 by 10 grid to represent the submerged cross section of the breakwater. Appendix E shows the computer program used to evaluate the theoretical solution. Theoretical results are presented for the median kh occurring in each of the small-model figures and for the specified constant kh occurring in each of the large-model figures.

The theoretical behavior is clear--transmission coefficients decrease and reflection coefficients increase with increasing wave steepness. The theory generally overestimates the transmission coefficient at all wave steepnesses and all wave numbers. In addition, the theory underestimates the reflection coefficient at low steepnesses and overestimates the reflection coefficient at high steepnesses. These discrepancies may be due to several factors including: (a) errors made in estimating the permeability, (b) unsteady modification of the steady-state damping law, (c) violation of the assumed macroscopic flow-field scale when particle orbits become smaller than the rubble diameter, and (d) roughness of the breakwater reflecting surface.

Errors caused by inferior estimates of the permeability are a real possibility. The slope intercept method of measuring permeability is very sensitive to inaccurate permeameter pressure readings at low flow rates. If the low flow-rate readings are omitted from the permeability analysis (also omit two high flow-rate readings which deviate from the rest of the data; see App. F, Fig. F), the permeability and friction factor calculations are revised (App. F, Tables F-4, F-5, and F-6). The tabulated values of C_f display a marked decrease in scatter relative to Tables F-1, F-2, and F-3 (App. F). This demonstrates that much of the error is in the low Reynolds number data.

The resulting permeability and friction coefficient values are summarized in Table 4.

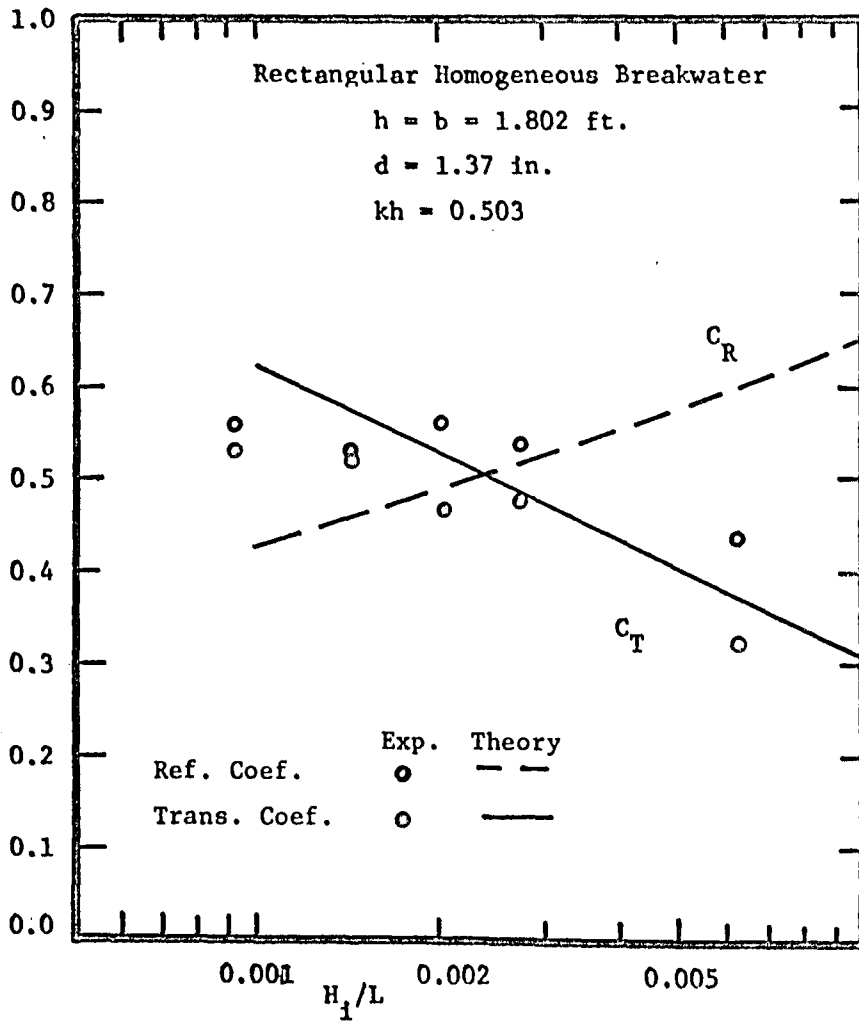


Figure 29. Reflection and transmission coefficient dependence on wave steepness.

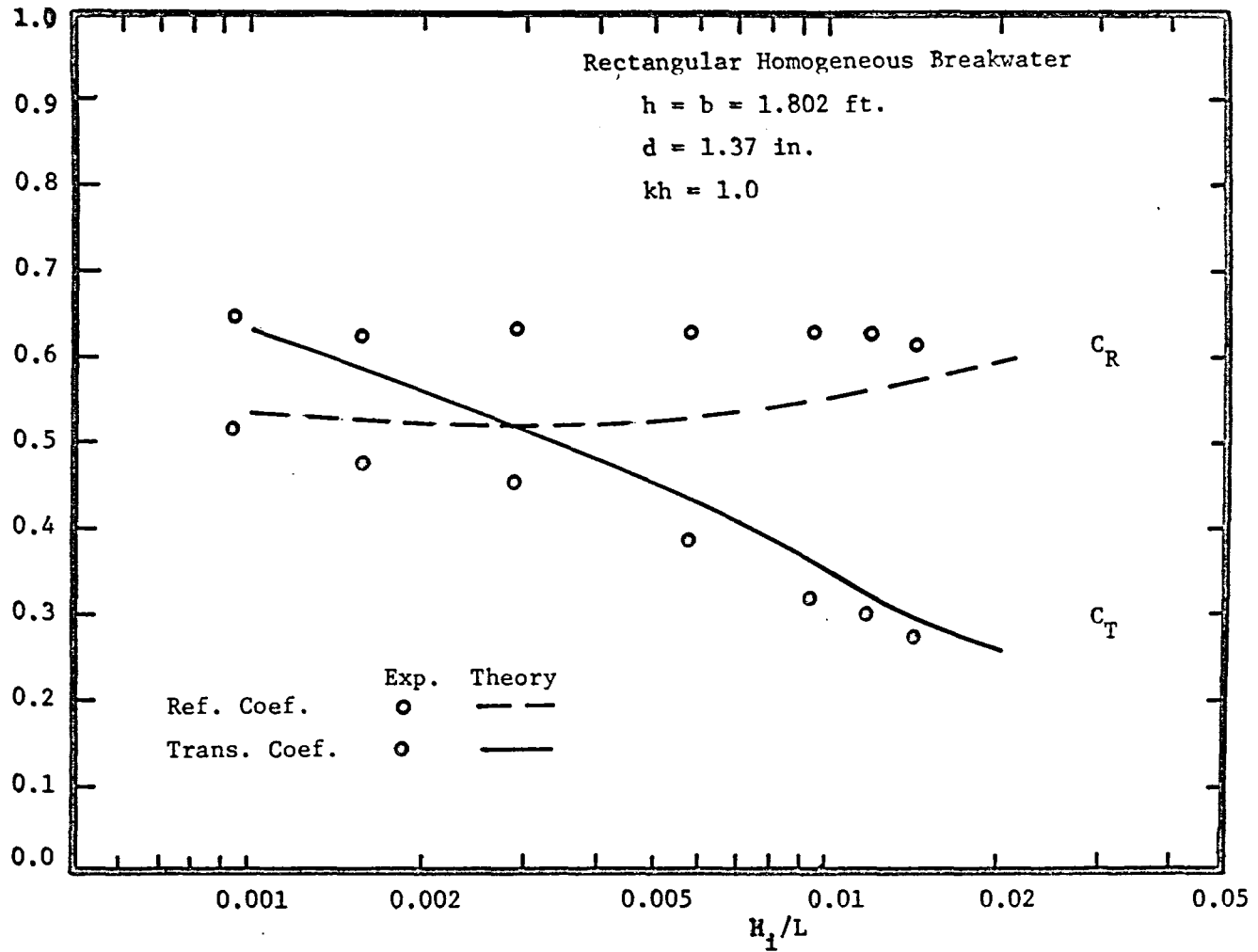


Figure 30. Reflection and transmission coefficient dependence on wave steepness.

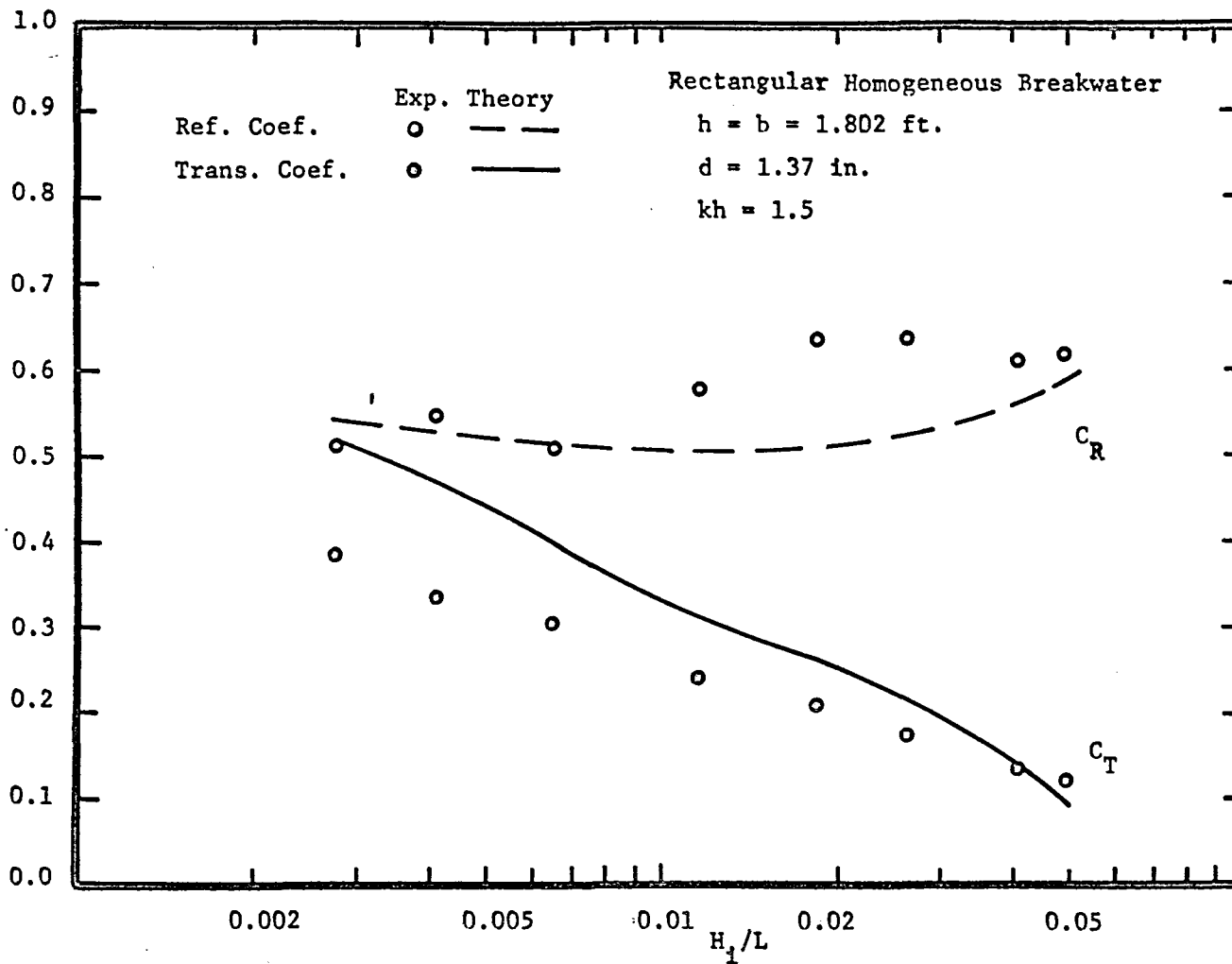


Figure 31. Reflection and transmission coefficient dependence on wave steepness.

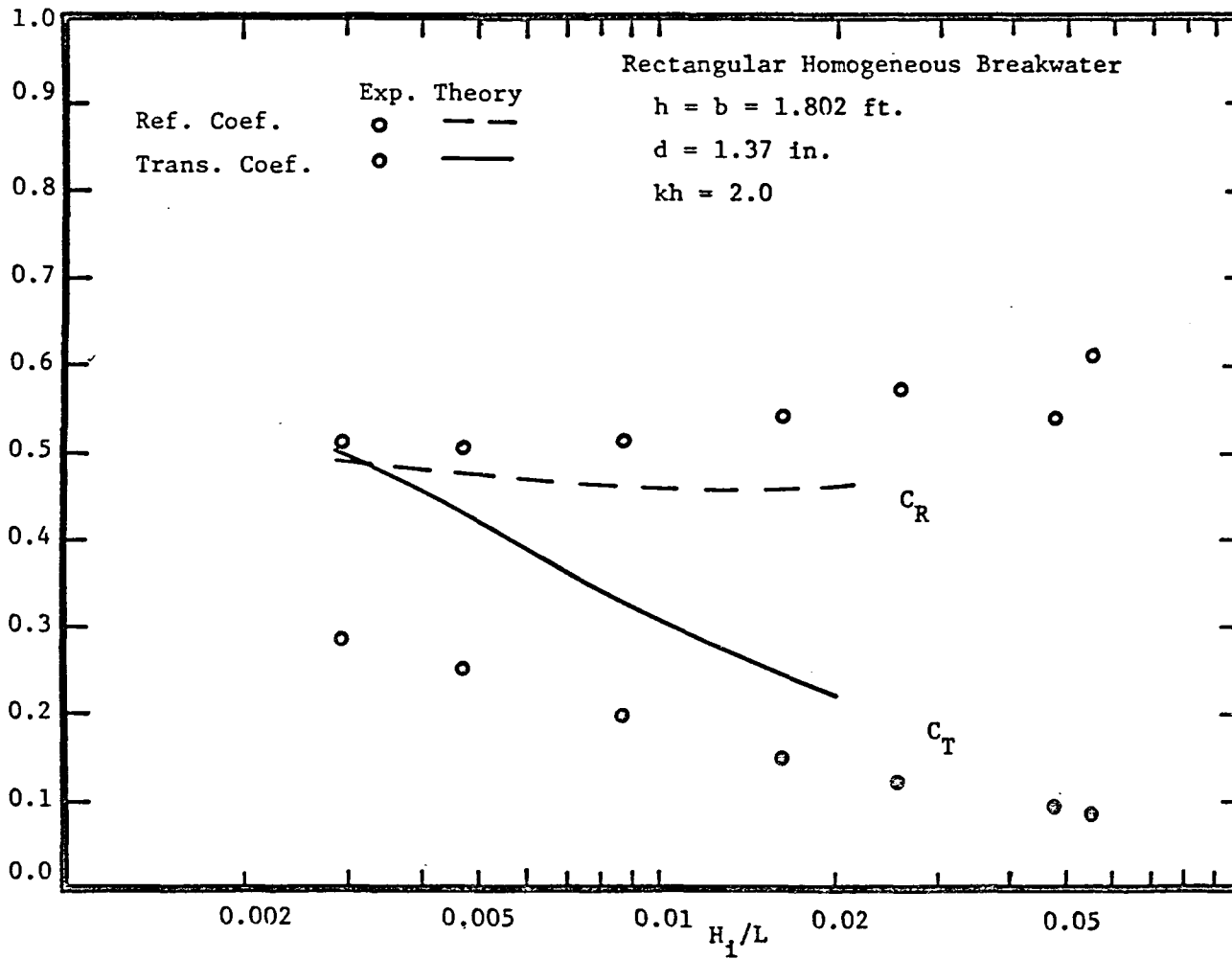


Figure 32. Reflection and transmission coefficient dependence on wave steepness.

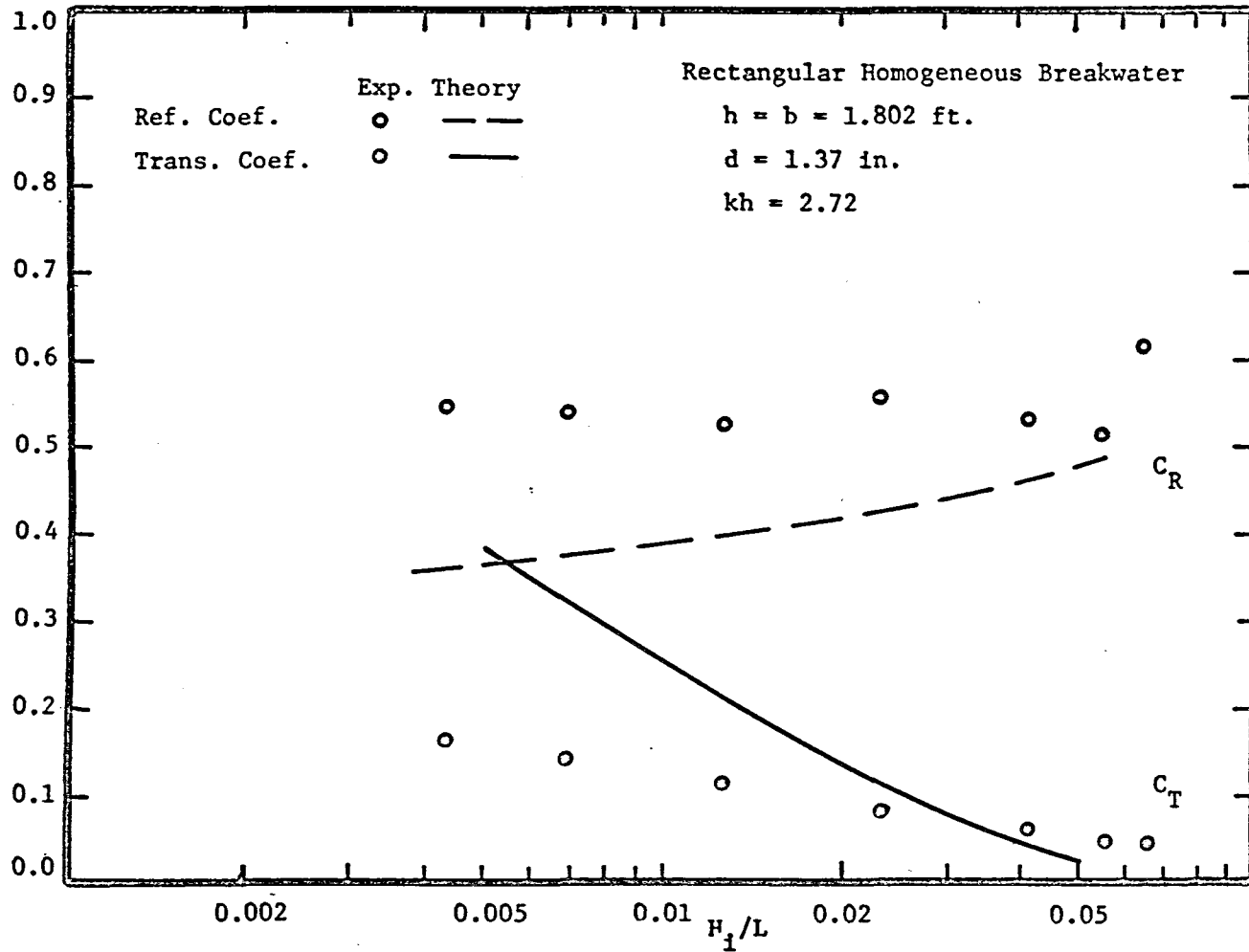


Figure 33. Reflection and transmission coefficient dependence on wave steepness.

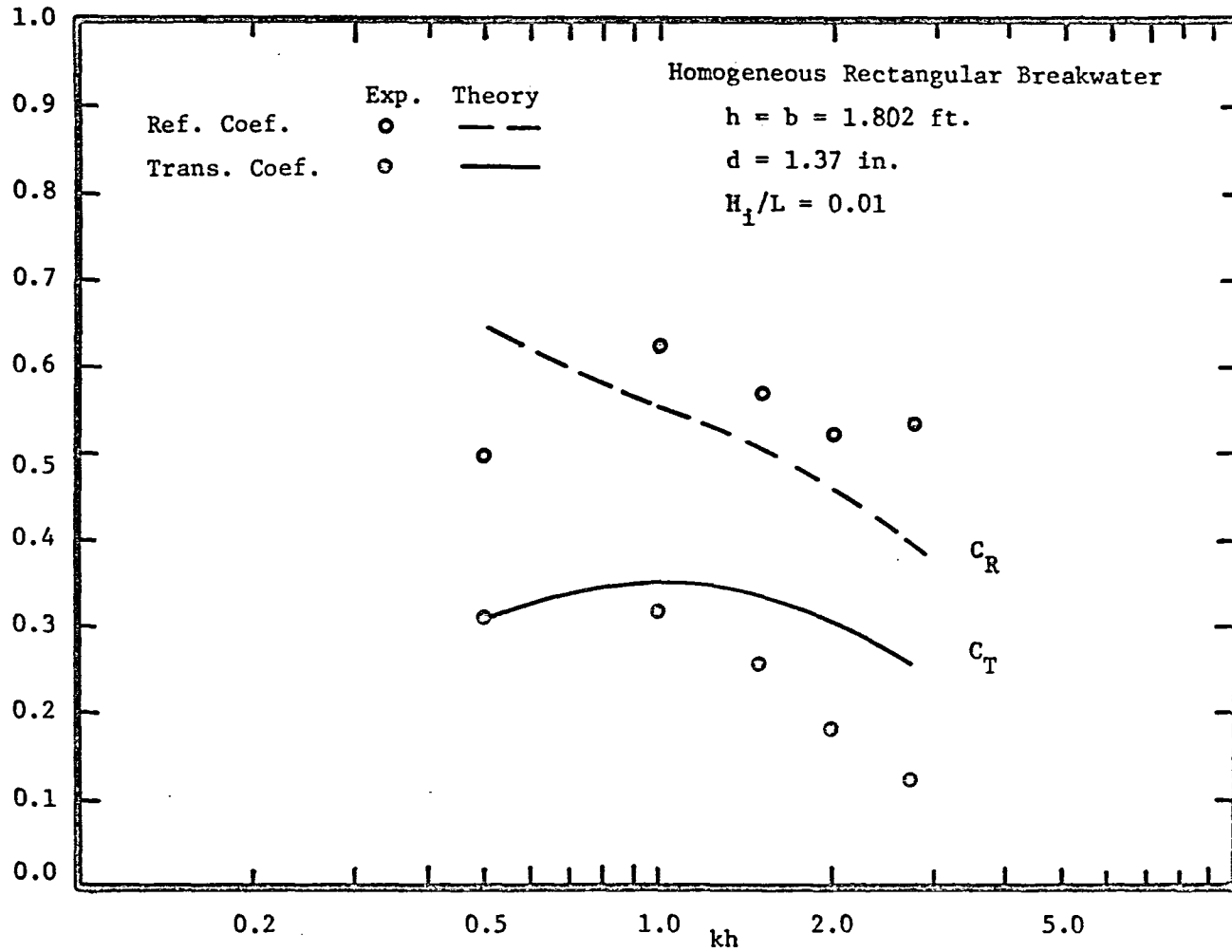


Figure 34. Reflection and transmission coefficient dependence on wave number.

Table 4. Revised media hydraulic properties.

Commercial size	Equivalent sphere diameter	Permeability	Turbulent damping coefficient
(in)	d (in)	K_p (ft ²)	C_f (dimensionless)
0.375	0.325	$2.53 \cdot 10^{-7}$	0.314
0.75	0.774	$7.19 \cdot 10^{-7}$	0.218
1.5	1.37	$3.20 \cdot 10^{-6}$	0.228

By comparing the properties in Table 4 with those in Table 3 it is evident that eliminating the low Reynolds number data decreases the permeability and the turbulent damping coefficient. However, the ratio of $C_f/K_p^{1/2}$ remains relatively constant. According to equation (5), this change in hydraulic properties produces more frictional resistance at low Reynolds numbers (where $1/K_p$ dominates) and the same resistance at high Reynolds numbers (where $C_f/K_p^{1/2}$ dominates). One might anticipate the latter result because the same high Reynolds number data are analyzed in both cases. The net effect of the reduced permeability is an apparent increase in the fluid resistance of the structure; this should cause a relative increase in the reflection coefficient and a decrease in the transmission coefficient.

The revised theoretical solution to the small breakwater problem is shown in Figure 35. Comparison with Figure 28 demonstrates that eliminating the low Reynolds number data from the permeability analysis does tend to improve correlation between experiment and theory. The improvement is relatively small compared to the large change in the permeability. This suggests that even in the small model, the unsteady damping is dominated by the turbulent resistance forces. It also indicates that in future studies it is probably not necessary to collect permeameter data at low Reynolds numbers. The high Reynolds number data are easier to obtain and seem to prescribe the media properties adequately. This certainly would apply for prototype-scale media.

Another source of discrepancy between theory and experiment may be that the steady-state damping law (eq. 3) is not entirely suitable for small models which are excited by relatively high-frequency waves. It may be necessary to add an unsteady inertial force to the resistance law as in the pile-array analysis, represented by equation (88). The net effect of the additional inertial force is to increase the inertial coefficient, S , to a value greater than unity. As shown in Figure 9, increasing S causes a corresponding increase in the reflection coefficient and decrease in the transmission coefficient. This would also tend to improve correlation between theory and experiment in Figures 23 to 34. One cannot predict the magnitude of the inertial coefficient in advance because the virtual mass of densely packed fractured stone is not known.

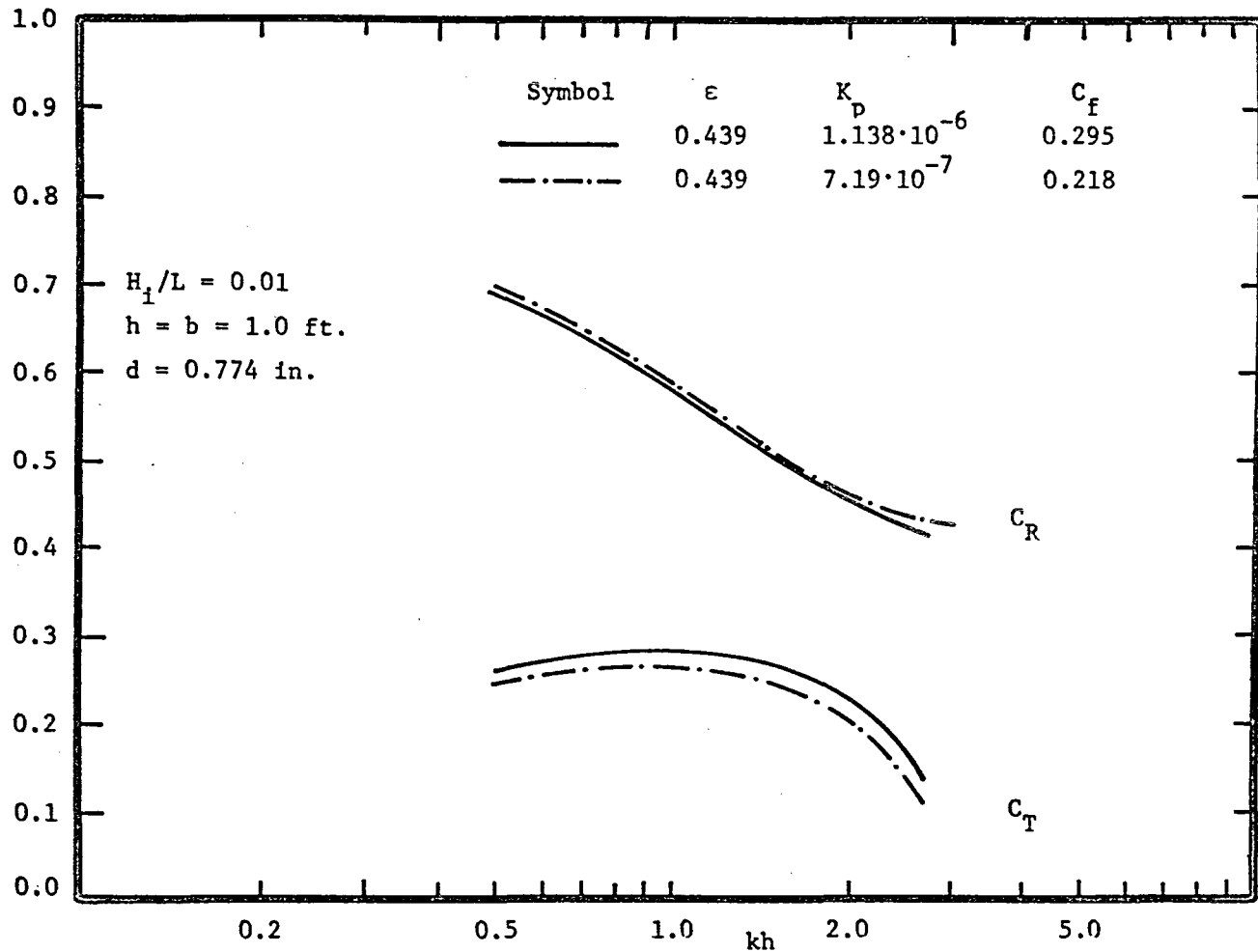


Figure 35. Reflection and transmission coefficient sensitivity to media hydraulic properties.

However, evaluation of S_r may serve as a calibrating link between theory and experiment in future studies.

Theory and experiment also tend to diverge for very small values of the incident wave amplitude. This response is apparent at small H_i/L on the constant kh curves, and at large kh on the constant H_i/L curves. It is hypothesized that this behavior is due to the scale of the fluid motion becoming smaller than the aggregate scale on the breakwater surface. As the wave amplitude becomes very small, the wave field orbit diameters are exceeded by the individual rock diameters on the slope. Then the waves begin interacting with individual pieces of gravel rather than a continuous porous slope. The reflection process is modified as waves are partially reflected directly off particle surfaces. As the relative scale of the particle increases, the direct-reflection processes dominate and the reflection coefficient seeks a limiting value near 50 to 60 percent. This value is equal to the percent of solids of the porous surface.

The theory does not account for this behavior because the seepage velocity concept assumes that fluid particle trajectories are large for media grain size so that interaction with individual units of media can be ignored. When the orbital trajectories are equal or less than the grain diameter, this assumption is violated. Then the flow field begins to function like a series of interconnected cells rather than a continuum.

The ratio of equivalent sphere diameter to water depth in both models is approximately $d/h = 0.064$. For the wave height to exceed the particle diameter, the lower limit on the wave steepness is:

$$H_i/L \sim (d/h)(h/L) \sim kh/100$$

Although this is only an approximate guide, it is apparent in the preceding figures that correlation between theory and experiment generally improve above this limiting steepness.

The fourth factor which influences the disparity between experiment and theory is the damping effect of the rough reflecting surface. As the wave heights increase, the attenuation due to surface roughness also increases. The theory does not account for this effect and therefore tends to overestimate the wave reflection at high steepnesses.

The experimental procedure for determining reflection coefficients assumes that the wave profiles are simple sinusoids. This procedure tends to underestimate the reflection coefficient when finite amplitude effects become significant (Goda, 1968), and may contribute to experimental error for the steep, long-wave measurements.

A scale effect in the transmission coefficient becomes apparent when the small- and large-model results are compared in Figures 28 and 34. This feature is discussed later in this section.

The theoretical results are heavily influenced by the approximation introduced through the Lorentz equivalent work principle. This linearizing technique prevents the theory from predicting the occurrence of high harmonics due to non-Darcian damping. The existence of these harmonics is only weakly evident in the experimental long-wave records. Nevertheless, part of the theoretical error may be attributed to the linear approximation.

In summary, it may be concluded that theory and experiment correlate best when the incident wave height exceeds the rock diameter on the windward breakwater face. The transmission coefficient is the more useful quantity and correlates better with the theory than does the reflection coefficient. The theory tends to slightly overestimate the transmission coefficient but this is a desirable condition for design application.

3. Trapezoidal-Layered Breakwater.

a. Experimental Results. Wave reflection and transmission data are collected using the procedures described previously. The data are tabulated in Appendix G.

The experiments are conducted at a stillwater depth of 14 inches. This water level is relatively high with respect to the elevation of the breakwater core. It is comparable to a high spring tide, a condition which is conducive to large transmission coefficients. The wave height and length are controlled by setting the generator frequency at predetermined constant values and then varying the eccentricity of the drive-wheel pin. This produces variable wave steepness at several constant wave numbers.

Figures 36 to 41 present the reflection and transmission coefficients as functions of incident wave steepness for six values of kh . The transmission coefficients behavior is similar to that observed for the homogeneous rectangular breakwater, i.e., transmission decreases with increasing wave steepness. The reflection coefficient, on the other hand, decreases with increasing wave steepness and wave number. The dependence on wave steepness results from waves breaking on the inclined slope. Observations during the experiments verify that steeper waves break more violently on the rough permeable slope.

The dependence on wave number is delineated in Figures 42 and 43. In contrast to the homogeneous rectangular breakwater results, a relative maximum does not appear in the reflection coefficient. The additional effect of wave breaking seems to reduce the reflection coefficients more abruptly and eliminates the relative maximum near $kh \approx 1.0$. However, a definite relative minimum does appear in the reflection coefficient near $kh \approx 2.5$ in the trapezoidal structure. A similar minimum is weakly apparent in the rectangular structures (Figs. 29 and 34). This behavior is interpreted as caused by the fluid-motion scale decreasing below the aggregate scale on the breakwater surface. When the wave velocity field orbit diameters become smaller than the aggregate diameter, the waves begin interacting with individual pieces of rubble as in the crib-style breakwater. Wave breaking is partially replaced by direct reflection off rubble surfaces, and the reflection coefficient tends to increase.

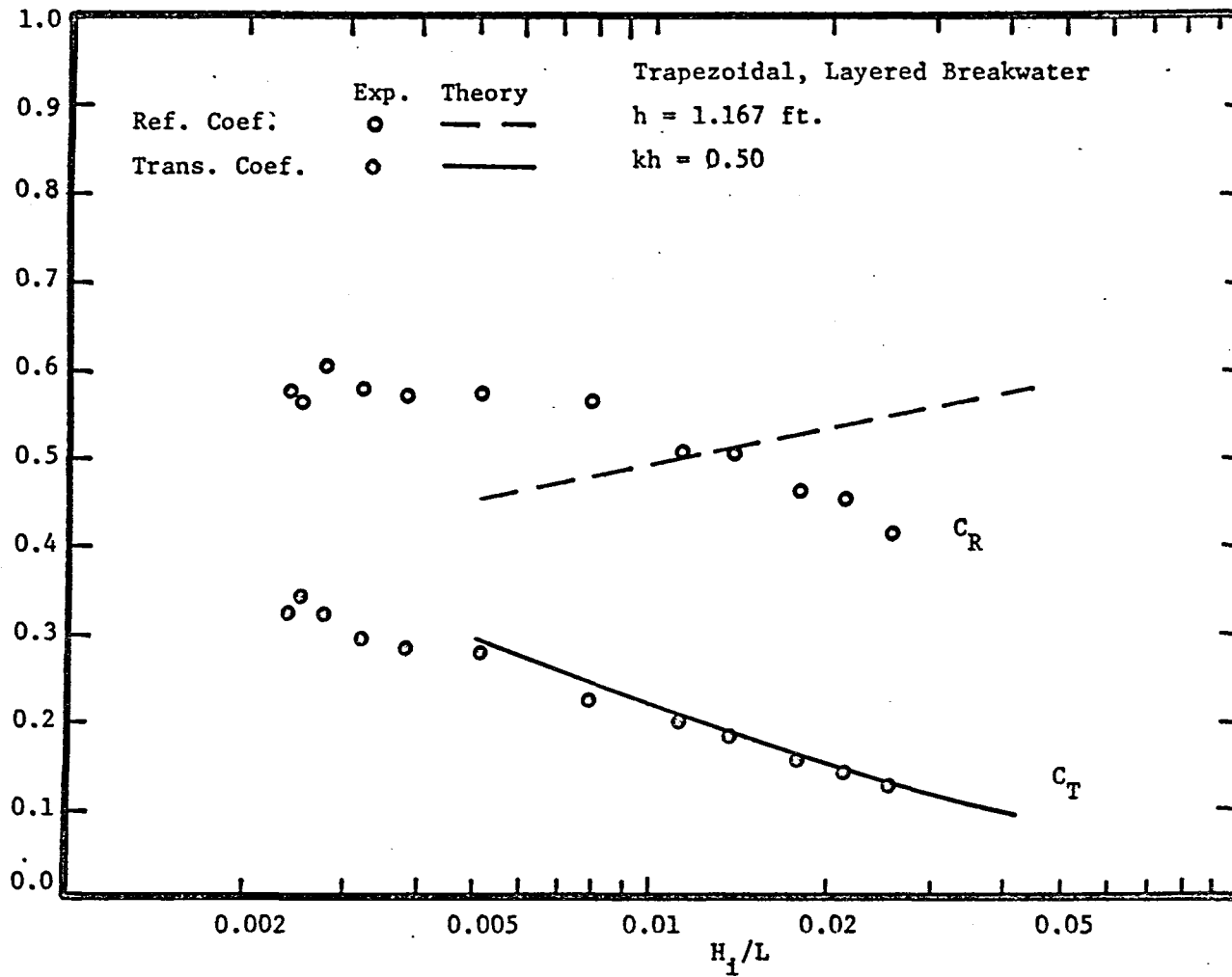


Figure 36. Reflection and transmission coefficient dependence on wave steepness.

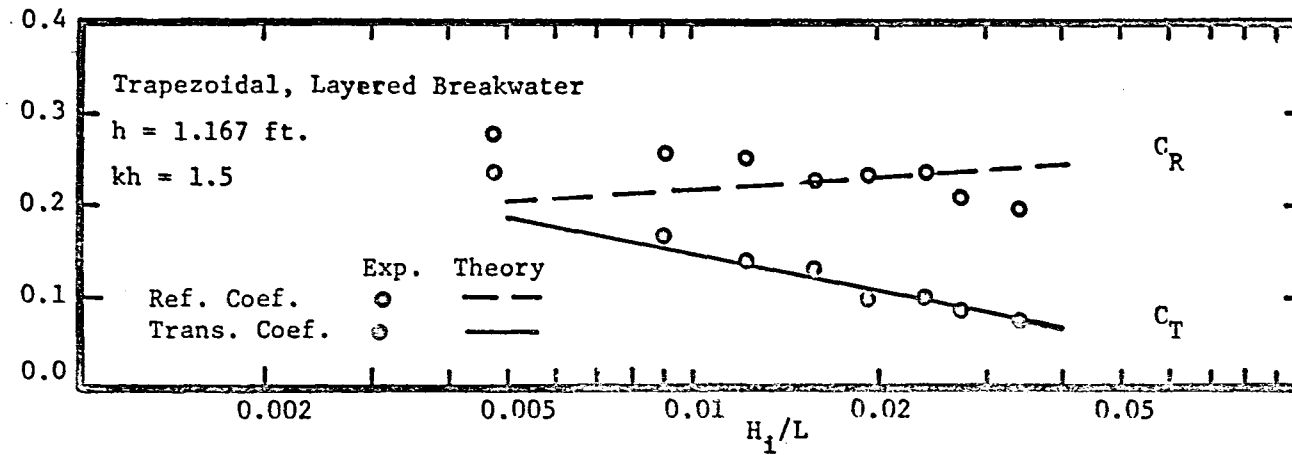


Figure 38. Reflection and transmission coefficient dependence on wave steepness.

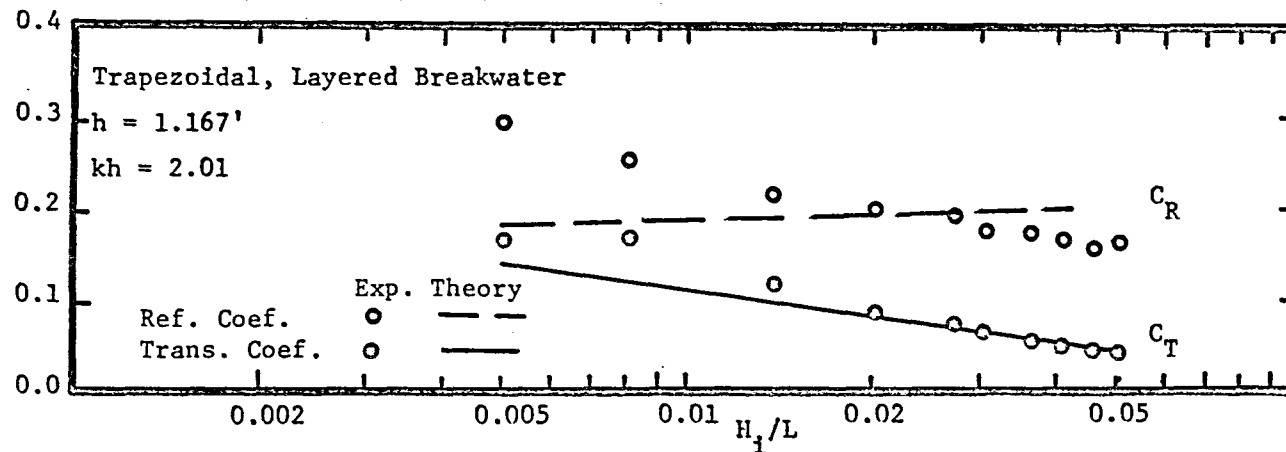


Figure 39. Reflection and transmission coefficient dependence on wave steepness.

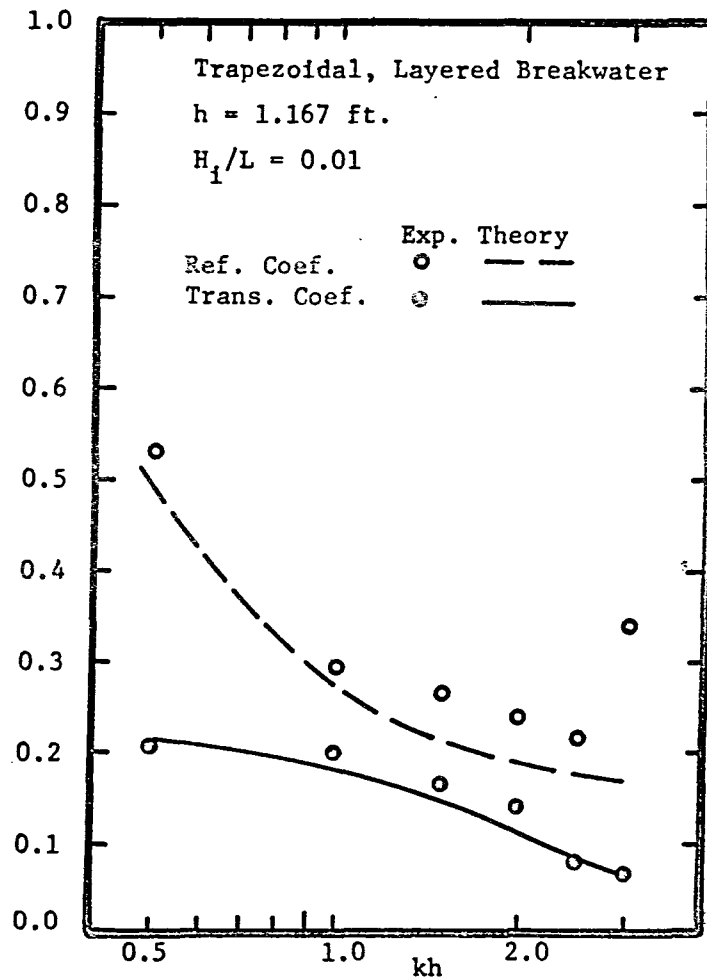


Figure 42. Reflection and transmission coefficient dependence on wave number.

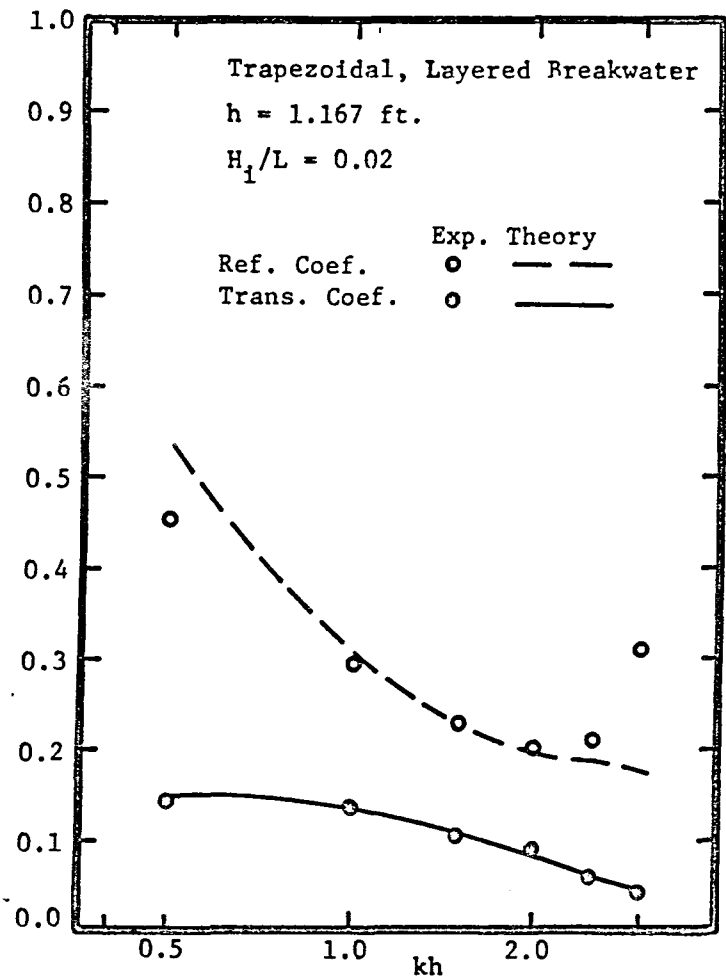


Figure 43. Reflection and transmission coefficient dependence on wave number.

This argument can be substantiated quantitatively. The velocity field orbit diameters are less than or equal to the wave height. For $kh = 2.5$ and $H_1/L = 0.02$, H_1/h is equal to 0.05. The ratio of the mean particle diameter to stillwater depth is equal to $d/h \approx 0.1$. Thus, the scale of the wave motion is approximately one-half the particle diameter when the reflection coefficient begins to increase.

b. Comparison of Experimental and Theoretical Results. The theoretical solution is obtained according to the procedures in Section II, 5, f. A five-term eigen series is chosen to specify the velocity field. The spatial integration in the numerator of the modified Lorentz equation is evaluated numerically using the discretization scheme of Appendix D. The breaking loss is evaluated with the roughness coefficient $f_s = 1/3$. This value is found to give best correlation between theory and experiment.

The theoretical results are presented in Figures 36 to 43. The solution behavior is similar to that of the crib-style breakwater--transmission decreases with increasing wave steepness and number; reflection increases with increasing steepness and decreasing wave number.

The transmission coefficient experimental and theoretical results correlate very well, even better than the crib-style breakwater results. It is likely that this is due to the inclusion of surface losses on the inclined face of the structure, whereas such losses are ignored on the vertical-face structure.

The reflection coefficient does not fare as well. The theory generally underestimates the experimental results at low steepnesses and overestimates the results at high steepnesses. In addition, the theory does not account for the abrupt increase in the reflection coefficient at $kh \approx 2.5$. The low steepness and high-wave number disparity can be attributed at least partially to the wave height becoming small with respect to the media grain diameter; this causes relative increases in the reflection coefficient. The theory does not account for this effect because it assumes the pore sizes to be small with respect to the length scale of the fluid motion. The inertial effect and errors in the permeability measurement may also contribute to any differences between theory and experiment.

The success of the theory is dependent on the evaluation of the surface-roughness coefficient, f_s . This coefficient is not a universal constant, but is a function of the shape of the armor-layer material. The value $f_s = 1/3$ determined in this study, represents an approximate first guess for all rubble slopes which are modeled using this theory. Tetrapods and other artificial armor material can be expected to have their own characteristic value. Further model studies are necessary to evaluate f_s for these materials. The form of the proposed empirical expression for Miche's intrinsic surface-reflection coefficient (eq. 80) has provided favorable results in the application of this study. Further comparison with other experiments is needed to verify its general applicability.

A general assessment of the theory is that it predicts the important features of wave interaction with conventional breakwaters quite well. The transmission coefficient is the quantity of greatest interest and it is evaluated within the range of experimental error. The results seem to justify the assumptions made in the equivalent rectangular breakwater solution. Although the validity of the theory is not established by comparison with a single set of experiments, the available results tend to support the assertion that the important physical processes have been accounted for.

4. Pile-Array Breakwaters.

Costello (1952) conducted two-dimensional model tests on pile-array structures composed of vertical circular cylinders. Experimental data from two of his models are presented herein and compared with the theory in Section II, 6.

The structures are composed of 3/8-inch-diameter piles spaced 1 inch on center in an orthogonal pattern of rows and columns. The resulting porosity is 89 percent. The water depth is maintained at 1.5 feet and the piles extend well above the maximum wave height. The two structures differ only in longitudinal extent; one is 24 rows long, the other is 48 rows long.

Incident and transmitted wave amplitudes are monitored with parallel-wire resistance-type wave gages. No mention or record of reflection measurements is given. The transmission coefficients are measured 3.5 feet shoreward of the test section. The incident wave characteristics are varied between the following limits: $0.01 < H_1/L < 0.12$; $1 \lesssim kh \lesssim 4$.

The transmission coefficients for both models are presented as functions of incident wave steepness in Figure 44. The graph shows that the transmission coefficient decreases with increasing wave steepness and increasing breakwater width. The dependence on wave number is too weak to positively identify.

The theoretical transmission coefficients are also plotted in Figure 44. The solution is obtained according to the procedure in Section II, 6, d. A five-term eigen series is used to describe the velocity field, and all other conditions in the solution are specified by the geometry of the structure.

Theoretical solutions are presented for $kh = 1, 2, \text{ and } 4$ and $0.01 < H_1/L < 0.1$. Correlation between experiment and theory is within the range of experimental error with the exception of the $kh = 2$ curve on the 4-foot-long structure. Costello (1952) does not provide the wave numbers for experimental data points on the long structure. Thus, it should not be inferred that the theory is in error because the experimental data simply may not apply to the $kh = 2$ curve.

A relative maximum occurs in theoretical transmission coefficient between $kh = 1$ and $kh = 4$. This response corresponds to that observed in the crib-style breakwater. However, the overall dependence on wave number is much weaker. The general behavior is similar to that of wave filters, i.e., high transmission and low reflection. The similarity is due to the high porosity in both structures.

The theoretical reflection coefficients are also plotted for $kh = 1$. Note that the reflection coefficient is greater for the short structure at this particular kh . The apparent reason is that the ratio of incident wavelength to the short structure length is 1:4. This causes the η_2 component, which reflects off the leeward face of the structure, to resonate. The behavior is analogous to a resonating tidal basin. The reflection coefficients for $kh = 2$ and 4 are clustered near $0.03 < C_R < 0.08$. Experimental data are not available for comparison.

The favorable correlation between experiment and theory in Figure 44 demonstrates the utility of the theory as applied to pile-array structures. Although the assumptions in the derivation apply rigorously only to long-wave excitation, the results seem to justify application of the theory to intermediate and short-wave excitation as well.

5. Scale Effects and Prototype Application.

A scale effect appears when the large- and small-model results are compared for constant H_i/L but variable kh . Figures 28 and 34 reveal that the reflection coefficients are nearly equal while the transmission coefficients are always greater in the large model. This shows that essentially the same energy is being transmitted into each structure while less is coming out of the small model. A qualitative argument can be made for this behavior on the basis of friction factor-type internal damping. Equation (5) gives the following relationship for the head loss per foot through the small model:

$$\left(\frac{\Delta h}{\Delta \ell}\right)_m = \frac{f_{K_{pm}}}{K_{pm}^{1/2}} \frac{u_m^2}{g}, \quad (99)$$

where $(\Delta h/\Delta \ell)_m$ is the head loss per unit length through a structure composed of rock of permeability K_{pm} , with friction factor $f_{K_{pm}}$ defined as in equation (6), and with u_m properly scaling the internal velocity field. Likewise, in the large model:

$$\left(\frac{\Delta h}{\Delta \ell}\right)_p = \frac{f_{K_{pp}}}{K_{pp}^{1/2}} \frac{u_p^2}{g}.$$

According to Dinoy (1971) and Ward (1964), the square root of the permeability is directly proportional to the hydraulic radius of the media. Thus, $K_{pm}^{1/2}$ scales with the model length scale. Froude modeling is assumed to govern the velocity field so the velocity is scaled proportional to the square root of the length scale. Summarizing:

$$K_{pm}^{1/2}/K_{pp}^{1/2} = L_m/L_p,$$

$$u_m^2/u_p^2 = L_m/L_p,$$

where L_m , L_p denote the length scales of the two models. Then the ratio of the head-loss gradients is simply:

$$\frac{(\Delta h/\Delta l)_m}{(\Delta h/\Delta l)_p} = \frac{f_{K_{pm}}}{f_{K_{pp}}}. \quad (100)$$

The friction factors scale according to equation (6) as:

$$f_{K_p} = \frac{1}{R_{K_p}} + C_f. \quad (101)$$

Table 4 shows that the revised C_f is approximately the same for the 0.774- and 1.37-inch gravel. The original estimate in Table 3 yields a C_f for the 0.774-inch gravel which is approximately 70 percent that of the larger stone. Without asserting which values are correct, it can be stated that the two values are nearly equal. The Reynolds numbers, on the other hand, scale according to the square of the length ratio. Because the small model operates at a considerably lower Reynolds number, it may be assumed that it has a larger characteristic friction factor according to equation (6). Equation (100) indicates that the head-loss gradient is greater in the small model, therefore damping is more severe. Consequently, the transmission coefficient is reduced in the small model.

This result has important implications for scaling experimental direct-transmission measurements because physical models tend to underestimate prototype transmission coefficients. Determining the magnitude of the scale effect in a particular model requires that specific values be assigned to the friction factors. The prototype friction factor may be set equal to C_f because the damping is fully turbulent. The model friction factor is a function of the Reynolds number and in an unsteady, spatially variable flow field the choice of an appropriate Reynolds number is not obvious.

The theoretical solution overcomes this difficulty by solving the prototype problem directly. The prototype solution requires an estimation of the physical and hydraulic properties of the full-scale media. One may determine these properties by performing the tests in Sections III, 2 and III, 3 on samples of small-scale rubble which have approximately the same angularity and packing as that anticipated in the prototype rubble. Then, according to the results of Dinoy (1971) and Ward (1964), the permeability scales directly proportional to the length ratio. The turbulent friction coefficient, C_f , and the porosity are the same in similar materials. The surface-roughness coefficient, f_s , is assumed to be the same in model and prototype. Thus, previously determined values for f_s which characterize common armor-layer materials may be used. With the media properties determined in this manner, the procedures of Section II are applied directly to solve the prototype problem.

V. CONCLUSION

1. Summary.

Rubble-mound breakwaters are designed to protect exposed marine areas from excessive wave activity. Observations of breakwaters interacting with surface waves in laboratory models and in full-scale field applications demonstrate that significant wave energy is transmitted through the interstices of structures commonly regarded as being impervious. The objective of this investigation is the development of a theoretical analysis to account for this phenomenon. The results are intended to be used by coastal engineers to compare the effectiveness of alternative breakwater configurations, independent of repetitive experimental programs.

Three different breakwater designs are considered: (a) crib-style breakwaters with vertical walls and homogeneous fill; (b) conventional trapezoidal-shaped structures with layered fill; and (c) pile-array breakwaters composed of vertical piles placed in symmetric patterns. The two-dimensional problem is studied. Waves are assumed to arrive at normal incidence and end effects are ignored.

The analysis begins with the unsteady equations of motion for unconfined flow through the voids of an arbitrary pervious structure. The resistance forces are specified by known turbulent damping laws for flow through coarse porous media and by drag and inertial forces for flow through pile arrays. In either case, convective accelerations in the macroscopic flow field are neglected and resistance forces are linearized to facilitate an analytical solution. The linearizing technique requires that the assumed first-order resistance law and the known turbulent law dissipate the same amount of energy during one wave period throughout the structure. The procedure explicitly evaluates the damping coefficient in the assumed form of the resistance law without resorting to fitting techniques with experimental data. This yields a potential flow solution which is dependent on wave amplitude as well as frequency, water depth and the structure damping properties.

Linear wave theory is assumed to apply outside the structure. The reflected and transmitted amplitudes are solved in the crib-style breakwater problem and the pile-array problem by requiring continuity or pressure and horizontal mass flux at the sea-breakwater interfaces. The conventional trapezoidal-layered breakwater problem is solved by identifying an equivalent rectangular breakwater which has the same submerged volume as that of the original structure. Breaking losses are accounted for by a semiempirical method which ultimately requires the experimental evaluation of a dimensionless constant. The constant seems to characterize the roughness of the reflecting surface. Breaking and internal losses are combined in the linearized damping law and a modified form of the crib-style breakwater problem is solved.

The complete solution is expressed as an infinite series of eigen functions. The first five terms are found to adequately specify the velocity field for wavelengths longer than deepwater waves. Considerable simplification is gained in the long-wave solution--only one eigen function is retained and depth dependence is eliminated. The long-wave solution has the greatest potential for design application.

2. Evaluation.

In all three breakwater configurations, theory and experiment generally concur that: (a) the transmission coefficient decreases with decreasing wavelength, breakwater porosity and permeability, and increasing wave height and breakwater width, and (b) the reflection coefficient decreases with decreasing breakwater width and wavelength, and increasing breakwater porosity and permeability.

Correlation between theory and experiment is best when the incident wave height exceeds the diameter of the medium. When the wave heights become much smaller than the characteristic medium diameter the breakwater behavior seems to be dominated by wave interaction with individual units of rubble and the theoretical assumption of a continuum no longer applies.

In general, the crib-style breakwater solution slightly overestimates the measured transmission coefficient and underestimates the reflection coefficient. The disparity is thought to be due to unsteady modification of the assumed form of the damping law, errors in determining the permeability and approximations introduced by the linearizing technique. Nevertheless, the predicted transmission coefficients are very useful design estimates.

Correlation between the conventional trapezoidal-shaped breakwater theory and experiment is very favorable. The results are contingent upon proper evaluation of the surface-roughness coefficient. The empirical expression proposed to account for wave breaking has produced gratifying results for one breakwater configuration but further verification is needed. The equivalent rectangular breakwater hypothesis also works well for long, low nonbreaking waves.

Agreement between theory and experiment for the pile-array structure confirms the validity of the analysis when applied to a well-defined, homogeneous vertical-face structure. The results indicate that the general method could be successfully applied to wave filters as well.

3. Future Investigations.

To apply the method proposed by this study to breakwaters of arbitrary shape and composition, further work is needed to verify the breaking loss calculation or to find a suitable substitute. The roughness coefficient should be evaluated for other armor-layer materials and it should be determined if scale effects are inherent in this coefficient.

Three-dimensional effects and oblique incidence also need to be studied. Combining the results with overtopping and diffraction techniques is a logical progression.

Breakwater response to random wave excitation may be of interest. It is to be anticipated that only long, low swell will penetrate the less permeable structures.

Finally, the linearizing technique used in this study precludes the existence of higher harmonics in the theoretical solution. A perturbation solution should be attempted for long-wave excitation to see if the generation of multiple harmonics is important. This may be a useful input to harbor seiching studies.

LITERATURE CITED

- BIÉSEL, F., "Equations de l'écoulement non lent en milieu perméable, application au calcul des filtres a houle," *La Houille Blanche*, No. 2, Mar.-Apr. 1950.
- CALHOUN, R.J., "Field Study of Wave Transmission Through a Rubble-Mound Breakwater," M.S. Thesis, U.S. Navy Postgraduate School, Mar. 1971.
- COSTELLO, R.D., "Damping of Water Waves by Vertical Circular Cylinders," *Transactions, American Geophysical Union*, Vol. 33, No. 4, Aug. 1952, pp. 513-519.
- CROSS, R.H., and SOLLITT, C.K., "Wave Transmission by Overtopping," Hydrodynamics Laboratory Technical Note No. 15, Massachusetts Institute of Technology, Cambridge, Mass., July 1971.
- DINOY, A.A., "Friction Factor and Reynolds Number Relationship in Flow Through Porous Media," M. Engineering Thesis, Asian Institute of Technology, Bangkok, Thailand, 1971.
- DUDGEON, C.R., "Wall Effects in Permeameters," *Journal of the Hydraulics Division*, American Society of Civil Engineers, Vol. 93, No. HY5, Sept. 1967, pp. 137-148.
- GODA, Y., and ABE, Y., "Apparent Coefficient of Partial Reflection of Finite Amplitude Waves," Report of the Port and Harbour Research Institute, Vol. 7, No. 3, Sept. 1968, pp. 3-58.
- GODA, Y., and IPPEN, A.T., "Theoretical and Experimental Investigation of Wave Energy Dissipators Composed of Wire Mesh Screens," Hydrodynamics Laboratory Report No. 60, Massachusetts Institute of Technology, Cambridge, Mass., Aug. 1963.
- HILDEBRAND, F.B., *Advanced Calculus for Applications*, Prentice-Hall, Englewood Cliffs, N.J., 1965, p. 208, 362.
- IJIMA, T., EGUCHI, Y., and KOBAYASHI, A., "Theory and Experiment on Permeable Breakwater and Quay Wall," T.R. No. 3, Coastal Engineering Research Laboratory, Kyushu University, Fukuoka, Japan, Apr. 1971.
- INTERNATIONAL BUSINESS MACHINES, "System 360 Scientific Subroutine Package, (360 A-CM-03X) Version III," Programmer's Manual, IBM Technical Publications Department, White Plains, N.Y., 1968.
- IPPEN, A.T., *Estuary and Coastline Hydrodynamics*, McGraw-Hill, N.Y., 1966, p. 13.
- KAMEL, A.M., "Water Wave Transmission Through and Reflection by Pervious Coastal Structures," Research Report H-69-1, U.S. Army Engineer Waterways Experiment Station, Vicksburg, Miss., Oct. 1969.

- KEULEGAN, G.H., "Gradual Damping of Solitary Waves, *Journal of Research of the National Bureau of Standards*, Reprint, Vol. 40, 1948, pp. 487-498.
- KOH, R.C.Y., and Le MÉHAUTÉ, B.J., "Wave Run-Up, State of the Art," NESCO Report S 245 B, National Engineering Science Company, Pasadena, Calif., Jan. 1966.
- KONDO, H., "An Analytical Approach to Wave Transmission Through Permeable Structures," *Coastal Engineering in Japan*, Vol. 13, 1970, pp. 31-42.
- LEAN, G.H., "A Simplified Theory of Permeable Wave Absorbers," *Journal of Hydraulic Research*, IAHR, Vol. 5, No. 1, 1967, pp. 15-30.
- Le MÉHAUTÉ, B., "Perméabilité Des Dignes En Enrochements Aux Ondes De Gravité Périodiques," Thèses, Université De Grenoble, France, 1957.
- Le MÉHAUTÉ, B., SNOW, G.F., and WEBB, L.M., "Gravity Waves on Bottom Slopes," NESCO Report S 245 A, National Engineering Science Company, Pasadena, Calif., Jan. 1966.
- LORENTZ, H.A., "Report of the State Committee Zuidersee 1918-1926," (Dutch Text), Den Haag, Alg, Landsdrukkerij, 1926.
- MICHE, M., "Pouvoir Réfléchissant des Ouvrages Maritimes Exposes a l'Action de Houle," *Annales des Ponts et Chaussées*, May-June 1951, pp. 285-319.
- MORAES, C.C., "Experiments on Wave Reflexion on Impermeable Slopes," *Proceedings of the 12th Coastal Engineering Conference*, Vol. 1, Sept. 1970, pp. 509-522.
- ROBERTSON, J.M., *Hydrodynamics in Theory and Application*, Prentice-Hall, Englewood Cliffs, N.J., 1965, p. 67, 281.
- ROUSE, H., *Advanced Mechanics of Fluids*, Wiley and Sons, N.Y., 1959, pp. 395-395.
- SAWARAGI, T., and KOICHIRO, I., "Effects of Structural Shape on Wave Run-Up and Damping," *Coastal Engineering in Japan*, Vol. 13, 1970, pp. 55-74.
- SCHLICHTING, H., *Boundary Layer Theory*, 6th ed., McGraw-Hill, N.Y., 1968, p. 529.
- SHUTO, N., and HASHIMOTO, H., "Hydraulic Resistance of Artificial Concrete Blocks," *Proceedings of the 12th Conference on Coastal Engineering*, Washington, D.C., Sept. 1970.
- STRAUB, L.G., and HERBICH, J.B., "Experimental Studies of Wave Filters and Absorbers," Project Report No. 44, St. Anthony Falls Hydraulic Laboratory, University of Minnesota, Minneapolis, Minn., Jan. 1956.

- WARD, J.C., "Turbulent Flow in Porous Median," *Journal of the Hydraulics Division*, American Society of Civil Engineers, Vol. 90, No. HY5, Sept. 1964, pp. 1-12.
- WIEGEL, R.L., "Parallel Wire Resistance Wave Meter," *Proceedings, First Conference on Coastal Engineering Instruments*, Berkeley, Calif., 1955, pp. 39-43.
- WILSON, K.W., "Scale Effect in Rubble-Mound Breakwaters," M.S.C.E. Thesis, Massachusetts Institute of Technology, Cambridge, Mass., 1971.
- WRIGHT, D.E., "Nonlinear Flow Through Granular Media," *Journal of the Hydraulics Division*, American Society of Civil Engineers, Vol. 94, No. HY4, July 1968, pp. 851-972.

APPENDIX A

ESTIMATING THE ROOTS TO THE COMPLEX DISPERSION EQUATION

To estimate the roots to the complex dispersion equation, it is helpful to write the equation in the dimensionless form:

$$\frac{\sigma^2 h}{g} (S - if) = \Gamma_n h (1 - i\alpha_n) \text{th } \Gamma_n h (1 - i\alpha_n).$$

Experience gained through numerous trial solutions to this equation has shown that for a wide range of frequencies and depths it is usually possible to find one solution near:

$$\frac{\sigma^2 h}{g} S \sim \Gamma'_n h \text{th } \Gamma'_n h,$$

and

$$\alpha'_n \sim \frac{f}{S},$$

where the prime denotes the first estimate in the iteration scheme. Γ_m and α_m represent the actual solution to the above estimates and the subscript m assumes the larger of the two values:

$$m = 1,$$

or

$$m = \frac{f \frac{\sigma^2 h}{g} + \frac{\Pi}{4}}{\Pi},$$

where integer math is used in the quotient. If $m > 1$, then in general there will be $m - 1$ solutions in the vicinity of:

$$\left. \begin{aligned} \alpha'_n \Gamma'_n h &\sim (2n - 1) \frac{\Pi}{2} \\ \Gamma'_n h &\sim 0.4n \end{aligned} \right\} n = 1, 2, \dots, m - 1,$$

The remaining solutions will be found near

$$\left. \begin{aligned} \alpha'_n \Gamma'_n h &\sim n\Pi \\ \Gamma'_n h &\sim \Gamma_{n-1} h \left(\frac{n-1}{n}\right) \end{aligned} \right\} n = m + 1, m + 2, \dots$$

These guidelines should be accepted as empirically based estimates rather than hard and fast rules. They are presented here because extracting roots from the dispersion equation can be a frustrating task without some knowledge of the behavior of the solution.

APPENDIX B

GENERAL CHARACTERISTICS OF THE COMPLEX DISPERSION EQUATION

The dispersion equations are transcendental and it is necessary to solve for the roots by iteration. In spite of this difficulty there are several features which can be identified without actually solving the equations. First, because the hyperbolic tangent is an odd function of the argument, the product $\Gamma_n \text{th } \Gamma_n h$ will always be positive. The denominator in equation (32) is also positive because:

$$0 < \sin^2 \alpha \Gamma h < 1,$$

and

$$\text{ch}^2 \Gamma h > 1.$$

The left-hand side of equation (32) is always positive and it follows that the numerator must be positive for any roots to the equation. The sine and hyperbolic sine are both odd functions but their quotient is even in the numerator of equation (32); thus, the entire equation is even with respect to Γ , and if $\Gamma = T$ is a solution to equation (32), then $\Gamma = -T$ is also a solution.

The denominator in equation (33) is identical to the numerator in equation (32) and, according to prior arguments, these quantities are positive and even. It is easy to show that the numerator of equation (33) is also positive, and even by considering the following:

$$|\alpha \text{ sh } 2\Gamma h| \geq |2\alpha \Gamma h|,$$

$$|\sin 2\alpha \Gamma h| \leq |2\alpha \Gamma h|,$$

therefore,

$$\left| \frac{\sin 2\alpha \Gamma h}{\alpha \text{ sh } 2\Gamma h} \right| \leq 1.0,$$

and

$$1 + \frac{\sin 2\alpha \Gamma h}{\alpha \text{ sh } 2\Gamma h} \geq 0.$$

In addition, $\sin 2\alpha \Gamma h$ and $\alpha \text{ sh } 2\Gamma h$ are both odd functions with respect to α and Γ ; thus, their quotient and the entire numerator are even. For f to be a proper damping coefficient, wherein it extracts momentum from fluid motion, it must be positive. By these arguments it has been established that the left-hand side of equation (33) is positive and the quotient on the right-hand side is positive and even. It follows directly that α_n must be positive to be a solution to equation (33).

APPENDIX C

EVALUATING LORENTZ'S CONDITION OF EQUIVALENT WORK

The velocity potentials and resulting velocities described in this study are generally complex. Nonlinear operations performed on complex quantities are not commutative; consequently, it is necessary to secure the real part of a function before undertaking operations such as equation (72). Some simplifications can be made by recognizing the separable properties of the special functions used in this study. For example, the complex velocity, q , may be written as:

$$q = (Q_R + i Q_I) e^{i\sigma t},$$

where

$$Q_R, Q_I = \text{real function } (x, z).$$

Then,

$$q = (Q_R + i Q_I)(\cos \sigma t + i \sin \sigma t),$$

and

$$q_R = \text{real } q = Q_R(\cos \sigma t - \frac{Q_I}{Q_R} \sin \sigma t).$$

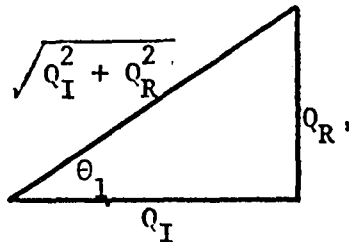
Define:

$$\frac{Q_I}{Q_R} = \cot \theta_1,$$

then,

$$q_R = -\frac{Q_R}{\sin \theta_1} \sin (\sigma t - \theta_1).$$

The phase triangle,



shows that

$$\frac{Q_R}{\sin \theta_1} = \sqrt{Q_R^2 + Q_I^2},$$

thus,

$$q_R = -\sqrt{Q_R^2 + Q_I^2} \sin(\sigma t - \theta_1).$$

Let

$$\theta = \sigma t - \theta_1,$$

then,

$$d\theta = d(\sigma t),$$

and

$$q_R = -\sqrt{Q_R^2 + Q_I^2} \sin \theta,$$

thus,

$$q_R > 0 : (2n - 1)\Pi < \theta < 2n\Pi,$$

$$q_R < 0 : 2(n - 1)\Pi < \theta < (2n - 1)\Pi.$$

Integrals involving the absolute value of functions of q present no problem if the above limits are observed, e.g.,

$$\begin{aligned} \int_{\sigma}^{\sigma t + 2\Pi} |q_R^3| d(\sigma t) &= \int_{(2n-1)\Pi}^{2n\Pi} q_R^3 d\theta - \int_{2(n-1)\Pi}^{(2n-1)\Pi} q_R^3 d\theta \\ &= (Q_R^2 + Q_I^2)^{3/2} \left\{ \int_{(2n-1)\Pi}^{2n\Pi} -\sin^3 \theta d\theta + \int_{2(n-1)\Pi}^{(2n-1)\Pi} \sin^3 \theta d\theta \right\} \\ &= \frac{8}{3} (Q_R^2 + Q_I^2)^{3/2} \frac{1}{T} \int_t^{t+T} |q_R^3| dt = \frac{1}{2\Pi} \int_{\sigma t}^{\sigma t + 2\Pi} |q_R^3| d(\sigma t) \\ &= \frac{4}{3\Pi} (Q_R^2 + Q_I^2)^{3/2}. \end{aligned} \tag{C-1}$$

Also,

$$\begin{aligned}
 \int_{\sigma t}^{\sigma t + 2\pi} q_R^2 d(\sigma t) &= \int_{2(n-1)\pi}^{2n\pi} q_R^2 d\theta = (Q_R^2 + Q_I^2) \int_{2(n-1)\pi}^{2n\pi} \sin^2 \theta d\theta \\
 &= \pi (Q_R^2 + Q_I^2) \frac{1}{T} \int_t^{t+T} q_R^2 dt = \frac{1}{2\pi} \int_{\sigma t}^{\sigma t + 2\pi} q_R^2 d(\sigma t) \\
 &= \frac{1}{2} (Q_R^2 + Q_I^2). \tag{C-2}
 \end{aligned}$$

Dividing the numerator and denominator of equation (72) by the wave period, T, and substituting in equations (C-1) and (C-2) yield:

$$f\sigma = \frac{\int_{-h}^0 dz \int_0^b dx \epsilon^2 \left\{ \frac{v}{K_p} \frac{1}{2} (Q_R^2 + Q_I^2) + \frac{C_f}{K_p^{1/2}} \epsilon \frac{4}{3\pi} (Q_R^2 + Q_I^2)^{3/2} \right\}}{\int_{-h}^0 dz \int_0^b dx \epsilon \frac{1}{2} (Q_R^2 + Q_I^2)}, \tag{C-3}$$

where

$$Q_R = \text{Real}(q/e^{i\sigma t}),$$

$$Q_I = \text{Imag}(q/e^{i\sigma t}).$$

The denominator of equation (C-3) may be evaluated analytically by defining a few auxiliary variables in terms of complex conjugates of known functions. Let the complex velocity field vector, with the temporal dependence removed, be denoted by:

$$Q = \hat{i}Q_x + \hat{k}Q_z = q/e^{i\sigma t},$$

Then,

$$Q_R^2 + Q_I^2 = Q \cdot Q^* = Q_x \cdot Q_x^* + Q_z \cdot Q_z^*,$$

where the superscript, (*), denotes the complex conjugate. Q_x and Q_z are evaluated from equation (36) as:

$$Q_x = \frac{\partial}{\partial x} \sum_{m=1}^n \phi_n / e^{i\sigma t},$$

$$Q_z = \frac{\partial}{\partial z} \sum_{m=1}^n \phi_n / e^{i\sigma t}.$$

Substituting the above into the denominator of equation (C-3) and evaluating the integrals produces the following result after much algebra,

$$\int_{-h}^0 dz \int_0^b dx \frac{\epsilon}{2} (Q_R^2 + Q_I^2) = \epsilon \sigma^2 \sum_{m=1}^n \frac{1}{\alpha_m \Gamma_m^2} \frac{1}{\text{ch} 2\Gamma_m h - \cos 2\alpha_m \Gamma_m h}$$

$$\left\{ \frac{(1 - e^{-2\alpha_m \Gamma_m d})}{4} \text{sh} 2\Gamma_m h \right.$$

$$\left. (a_{1m} a_{1m}^* + a_{2m} a_{2m}^*) - \frac{e^{-\alpha_m \Gamma_m b}}{2} \sin 2\alpha_m \Gamma_m h \sin \Gamma_m b (a_{1m} a_{2m}^* + a_{1m}^* a_{2m}) \right\}. \quad (C-4)$$

The complex conjugate amplitude products may be replaced by the following:

$$(a_{1m} a_{1m}^* + a_{2m} a_{2m}^*) = a_i^2 (C_{1R_m}^2 + C_{1I_m}^2 + C_{2R_m}^2 + C_{2I_m}^2), \quad (C-5)$$

and

$$(a_{1m} a_{2m}^* + a_{1m}^* a_{2m}) = 2a_i^2 (C_{1R_m} C_{2R_m} + C_{1I_m} C_{2I_m}), \quad (C-6)$$

where

$$C_{1R_m}, C_{2R_m} = \text{Real} (C_{1m}, C_{2m}),$$

$$C_{1I_m}, C_{2I_m} = \text{Imag.} (C_{1m}, C_{2m}).$$

Combining equations (C-4), (C-5), and (C-6) yields the form of the definite integral which is used in the computer program of Appendix D.

The results also apply to the first term in the numerator if the permeability is constant. The second term must be evaluated numerically because of the absolute value requirements.

The numerical integration is accomplished by discretizing the break-water cross section according to Appendix E and evaluating Q_x and Q_z at each grid point. The absolute values are taken and a summation is performed using a trapezoidal rule. Sufficient comment cards are presented in the computer program listing to make this clear.

APPENDIX D

COMPUTER PROGRAM LISTING

This appendix lists the computer program used to solve the trapezoidal-layered breakwater problem. Sufficient comment cards are included to make the computation scheme clear. A sample output is also presented.

C		MAIN0001
C	WAVE REFLECTION AND TRANSMISSION AT PERMEABLE BREAKWATERS	MAIN0002
C		MAIN0003
	COMPLEX CCH,CSF,CRG,IP,CPLX,OMEGA,ESF,SFE,YG,CHK,YH,YA,YB,CHI	MAIN0004
	COMPLEX ZETA,CEXP	MAIN0005
	COMPLEX C1X(27,5),C2X(27,5),CZ(8,5),SZ(8,5)	MAIN0006
	COMPLEX KE(5),KI(5),YC(5),SHK(5),YI(5),CR(5),CT(5),C1(5),C2(5)	MAIN0007
	COMPLEX YE(5,5),YF(5,5),YD(5),Y(10,10),C(10)	MAIN0008
	REAL EPL(5),CFL(5),PERML(5),AKH(10),CAMBR(10)	MAIN0009
	REAL EPS(8,27),CF(8,27),PERM(8,27),EXZ(8,27)	MAIN0010
	REAL KH(5),CIR(5),CII(5),C2R(5),C2I(5),CFR(5),CRI(5),CTR(5)	MAIN0011
	REAL CTI(5),PHZR(5),PHZ1(5),PHZ2(5),PHZT(5),GAMA(5),BETA(5)	MAIN0012
	REAL T1(5),T2(5),REF(5),TRANS(5)	MAIN0013
	INTEGER LAYER(8,27)	MAIN0014
C		MAIN0015
C	IN THE DIMENSION STATEMENTS ABOVE, THE PARTICULAR INTEGERS USED	MAIN0016
C	CORRESPOND TO 5=N, 1C=LIMIT=2*N, 8=NZ, 27=NX	MAIN0017
C		MAIN0018
C	THE FOLLOWING ARE STATEMENT FUNCTIONS	MAIN0019
C		MAIN0020
	CH(ARG)=0.5*(EXP(ARG)+EXP(-ARG))	MAIN0021
	SH(ARG)=0.5*(EXP(ARG)-EXP(-ARG))	MAIN0022
	CCH(CRG)=0.5*(CEXP(CRG)+CEXP(-CRG))	MAIN0023
	CCH(CRG)=0.5*(CEXP(CRG)-CEXP(-CRG))	MAIN0024
C		MAIN0025
C	FGCT, POUND, SECCND UNITS USED FOR DIMENSIONAL QUANTITIES	MAIN0026
C		MAIN0027
C	IM=SQRT OF MINUS ONE	MAIN0028
C	VISCO=KINEMATIC VISCOSITY	MAIN0029
C	G=GRAVITY	MAIN0030
C		MAIN0031
	IM=CMPLX(C,C,1.0)	MAIN0032
	VISCO=1.05E-5	MAIN0033
	G=32.2	MAIN0034
	PI=3.14159265	MAIN0035
	DEGRE=180./PI	MAIN0036

C	EP=C.C	MAIN0027
C	READ IN BREAKWATER PROPERTIES	MAIN0028
C		MAIN0039
C	S=INERTIAL COEFF	MAIN0040
C	EH=BREAKWATER WIDTH	MAIN0041
C	F=DEPTH OF SWL	MAIN0042
C	SLCPE=COTANGENT OF ANGLE OF INCLINATION OF WINDWARD BREAKWATER FACE	MAIN0043
C	BREAK=SURFACE BREAKING COEFF OF SLCPE	MAIN0044
C		MAIN0045
C	READ(5,1010)S,B,F,H,SLCPE,BREAK	MAIN0046
C		MAIN0047
C	NZ,NX=DIMENSION OF ARRAY WHICH SPECIFIES SPATIAL VARIATION OF	MAIN0048
C	BREAKWATER PROPERTIES	MAIN0049
C	NL=NO. OF DISCRETE LAYERS IN BREAKWATER	MAIN0050
C	N=NO. OF EIGEN FUNCTIONS	MAIN0051
C	NK=NO. OF WAVE NOS. USED AS INCIDENT WAVE EXCITATION	MAIN0052
C	NC=NO. OF WAVE CAMBERS(STEEPNESS) USED AS INCIDENT WAVE EXCITATION	MAIN0053
C	IFMAX=MAX. NO. OF CYCLES ALLOWED IN ITERATIVE SOLUTION	MAIN0054
C		MAIN0055
C	READ(5,1015)NX,NZ,NL,N,NK,NC,IFMAX	MAIN0056
C		MAIN0057
C		MAIN0058
C	LAYER(I,J)=IDENTIFIES PROPERTIES OF LOCATION I,J WITH ONE OF NL LAYERS	MAIN0059
C		MAIN0060
C	READ(5,1020)((LAYER(I,J),J=1,NX),I=1,NZ)	MAIN0061
C		MAIN0062
C	SET PREFIX OF I IN 1020 FORMAT EQUAL TO NX	MAIN0063
C	EPL(I)=POROSITY OF LAYER I	MAIN0064
C	CFL(I)=TURBULENT FRICTION COEFF OF LAYER I	MAIN0065
C	PERML(I)=PERMEABILITY OF LAYER I	MAIN0066
C		MAIN0067
C	READ(5,1030)(EPL(I),CFL(I),PERML(I),I=1,NL)	MAIN0068
C	CO 10 I=1,NZ	MAIN0069
C		MAIN0070
C	EP=MEAN POROSITY OF SEAWARD FACE OF RECTANGULAR BREAKWATER	MAIN0071
C		MAIN0072

C	EP=EP+EPL(LAYER(I,1))	MAIN0073
	DO IC J=1,NX	MAIN0074
	IJ=LAYER(I,J)	MAIN0075
C		MAIN0076
C	EPS(I,J)=POROSITY AT LOCATION I,J	MAIN0077
C	CF(I,J)=TURBULENT FRICTION COEF AT LOCATION I,J	MAIN0078
C	PERM(I,J)=PERMEABILITY AT LOCATION I,J	MAIN0079
C		MAIN0080
	EPS(I,J)=EPL(IJ)	MAIN0081
	CF(I,J)=CFL(IJ)	MAIN0082
10	FERM(I,J)=PERML(IJ)	MAIN0083
	EP=EP/NZ	MAIN0084
	LIMIT=2*N	MAIN0085
	LIME=LIMIT-1	MAIN0086
	B=BH/H	MAIN0087
	NI=NZ-1	MAIN0088
	NJ=NX-1	MAIN0089
C		MAIN0090
C	DELZ,DELX=DIMENSIONLESS GRID SPACING BETWEEN POINTS SPECIFYING	MAIN0091
C	BREAKWATER PROPERTIES	MAIN0092
C		MAIN0093
	DELX=B/NJ	MAIN0094
	DELZ=1.0/NI	MAIN0095
C		MAIN0096
C	ALPHA=ANGLE OF INCLINATION OF BREAKWATER SLOPE.	MAIN0097
C		MAIN0098
	IF(SLOPE.LE..1E-5)ALPHA=PI/2.	MAIN0099
	IF(SLOPE.GE..1E-5)ALPHA=ATAN(1.0/SLOPE)	MAIN0100
	SIA=SIN(ALPHA)	MAIN0101
C		MAIN0102
C	HLMAX=MAX. WAVE STEEPNESS WHICH WILL NOT BREAK ON SLOPE (MICHE'S	MAIN0103
C	CRITERION)	MAIN0104
C		MAIN0105
	HLMAX=SQRT(2.*ALPHA/PI)*SIA*SIA/PI	MAIN0106
C		MAIN0107
		MAIN0108

C	WRITE OUT BREAKWATER PROPERTIES	MAIN0109
C		MAIN0110
	WRITE(6,1040)	MAIN0111
	WRITE(6,1050)NX,BH,NZ,H	MAIN0112
	WRITE(6,1055)SLCPE	MAIN0113
	WRITE(6,1060)((LAYER(I,J),J=1,NX),I=1,NZ)	MAIN0114
C		MAIN0115
C	SET THE PREFIX OF I IN 1060 FORMAT EQUAL TO NX	MAIN0116
C		MAIN0117
	WRITE(6,1070)	MAIN0118
	WRITE(6,1080)	MAIN0119
	WRITE(6,1090)(I,EPL(I),PERML(I),CFL(I),I=1,NL)	MAIN0120
C		MAIN0121
C	READ IN WAVE PROPERTIES	MAIN0122
C	AKH(I)=PRODUCT OF INCIDENT WAVE NO. WITH DEPTH (PROGRESSIVE MODE)	MAIN0123
C	CAMBR(I)=INCIDENT WAVE STEEPNESS	MAIN0124
C		MAIN0125
	READ(5,1100)(AKH(I),I=1,NK)	MAIN0126
	READ(5,1100)(CAMBR(I),I=1,NC)	MAIN0127
	WRITE(6,1110)S,EP,VISCC	MAIN0128
	WRITE(6,1115)BREAK	MAIN0129
	CG 1000 IK=1,NK	MAIN0130
C		MAIN0131
C	SOLVE EIGEN VALUE WAVE NOS. OUTSIDE BREAKWATER, KE(M)	MAIN0132
C		MAIN0133
C	NOTE: ALL WAVE NOS. IN THIS PROGRAM ARE DIMENSIONLESS, I.E.,	MAIN0134
C	INCLUDE THE PRODUCT WITH DEPTH. LIKEWISE THE HORIZONTAL SCALE IS	MAIN0135
C	MADE DIMENSIONLESS BY DIVIDING THROUGH BY DEPTH	MAIN0136
C		MAIN0137
	KE(1)=AKH(IK)	MAIN0138
	KH(1)=AKH(IK)	MAIN0139
C		MAIN0140
C	SIG= WAVE ANGULAR FREQUENCY	MAIN0141
C		MAIN0142
	SIG=SQRT(G*KH(1)*TAN(KH(1))/H)	MAIN0143
	SIG4=SIG**4	MAIN0144

```

C          SHG=SIG*SIG*F/G                                MAIN0145
C          PER=WAVE PERIOD                                MAIN0146
C          PER=2.*PI/SIG                                  MAIN0147
C          PER=2.*PI/SIG                                  MAIN0148
C          WAVEL=INCIDENT WAVE LENGTH                    MAIN0149
C          WAVEL=INCIDENT WAVE LENGTH                    MAIN0150
C          WAVEL=2.*C*PI*H/KH(1)                          MAIN0151
C          ARG=KH(1)                                       MAIN0152
C          CO=CH(ARG)                                       MAIN0153
C          SI=SH(ARG)                                       MAIN0154
C          FXH=(KH(1)+SI*CO)/(CC*CO)                       MAIN0155
C          DELTA=MIC*E*S INTRINSIC REFLECTICN COEF      MAIN0156
C          DELTA=MIC*E*S INTRINSIC REFLECTICN COEF      MAIN0157
C          DELTA=MIC*E*S INTRINSIC REFLECTICN COEF      MAIN0158
C          DELTA=MIC*E*S INTRINSIC REFLECTICN COEF      MAIN0159
C          IF(SLOPE.LE..1E-5)DELTA=1.0                    MAIN0160
C          IF(SLOPE.GE..1E-5)DELTA=1.0-EXP(-1./(SLOPE*BREAK*SHG)) MAIN0161
C          WRITE(6,1120)KH(1),S*CO,PER,WAVEL              MAIN0162
C          WRITE(6,1125)DELTA                              MAIN0163
C          CC 20 M=2,N                                      MAIN0164
C          KE(M)=-[M*PI*(M-1)                              MAIN0165
C          CMEGA=SHG                                       MAIN0166
C          CALL EIGEN(M,CMEGA,KE(M),LARM)                   MAIN0167
C          IF(LARM.EQ.1)GO TO 1CCC                           MAIN0168
C          20 KH(M)=-AIMAG(KE(M))                          MAIN0169
C          F=1.C                                           MAIN0170
C          CD 990 IC=1,NC                                    MAIN0171
C          BEGIN ITERATION CN F                             MAIN0172
C          F=LINEARIZED DAMPING COEF                       MAIN0173
C          ITERF=0                                          MAIN0174
C          A=INCIDENT WAVE AMPLITUDE                       MAIN0175
C          A=INCIDENT WAVE AMPLITUDE                       MAIN0176
C          A=INCIDENT WAVE AMPLITUDE                       MAIN0177
C          A=INCIDENT WAVE AMPLITUDE                       MAIN0178
C          A=INCIDENT WAVE AMPLITUDE                       MAIN0179
C          A=INCIDENT WAVE AMPLITUDE                       MAIN0180

```

```

      A=CAMBR(IC)*WAVEL/2.C
      WRITE(6,113C)CAMBR(IC)
C
C
C
      SCLVE FOR BREAKING LOSSSES
C
      FLC=A*SIG*SIG*SQRT(FKT)/(PI*G)
      RMICH=HLMAX/FLC
      IF(RMICH.GT.1.0)RMICH=1.0
      EMICH=(DELTA*RMICH)**2
C
C
C
      ELOSS=DIMENSIONLESS ENERGY LCST TO BREAKING
C
      ELCSS=G*G*FKT*(1.0-EMICH)/(2.0*BT*H*SIG4)
      IF(ELOSS.LT.C.C)ELOSS=C.C
      IF(SLOPE.LT..1)ELCSS=C.0
30  ITERF=ITERF+1
      IF(ITERF.GT.IFMAX)GO TO 410
      IF(ITERF.EQ.1.AND.IC.GT.1)F=F*SQRT(CAMBR(IC)/CAMBR(IC-1))
C
C
C
      SCLVE EIGEN VALUE WAVE NOS. INSIDE BREAKWATER, KI(M)
C
      FSTG=F*STG
      SSHG=S*STG
      M=1
C
C
C
      CMEGA=SIGMA*SIGMA*H/G*(S-IM*F) IN THESIS NOTATION
C
      CMEGA=SSHG-IM*FSHG
      XR=SSHG+F/LC.
      IF(SSHG.LE.1.0.AND.FSTG.GT.4.C)XR=SSHG*(1.0+F/10.)
      YIM=FSHG
      NFS=FSHG/3.+1.
      IF(SSHG.LT.2..AND.FSTG.LT.3.*NFS.AND.FSHG.GT.3.*NFS-1)YIM=NFS*PI
C
C
C
      ESTIMATE AN INITIAL VALUE TO KI(M) AND THEN CALL 'EIGEN' TO
      SCLVE FOR EXACT VALUE VIA NEWTON-RAPHSON METHOD
C

```

```

      MAIN0181
      MAIN0182
      MAIN0183
      MAIN0184
      MAIN0185
      MAIN0186
      MAIN0187
      MAIN0188
      MAIN0189
      MAIN0190
      MAIN0191
      MAIN0192
      MAIN0193
      MAIN0194
      MAIN0195
      MAIN0196
      MAIN0197
      MAIN0198
      MAIN0199
      MAIN0200
      MAIN0201
      MAIN0202
      MAIN0203
      MAIN0204
      MAIN0205
      MAIN0206
      MAIN0207
      MAIN0208
      MAIN0209
      MAIN0210
      MAIN0211
      MAIN0212
      MAIN0213
      MAIN0214
      MAIN0215
      MAIN0216

```

C	SEE APPENDIX B FOR EXPLANATION OF INITIAL ESTIMATES TO KI(M)	MAINC217
C		MAINC218
	KI(M)=XR-IM*YIM	MAINC219
	CALL EIGEN(M,CMEGA,KI(M),LARM)	MAINC220
	IF(LARM.EQ.1)GO TO 1CCO	MAINC221
	NPI=FSHG/PI+C.25	MAINC222
	IF(NPI.LT.1)GO TO 5C	MAINC223
	CC 40 I=1,NPI	MAINC224
	M=I+1	MAINC225
	YIM=(I-0.5)*PI	MAINC226
	XR=PI*I*(I-0.25)/(2.C+FSHG)	MAINC227
	KI(M)=XR-IM*YIM	MAINC228
	CALL EIGEN(M,OMEGA,KI(M),LARM)	MAINC229
	IF(LARM.EQ.1)GO TO 1CCO	MAINC230
	IF(M.GE.N)GO TO 7C	MAINC231
40	CCCONTINUE	MAINC232
50	NPI=NPI+2	MAINC233
	CO 60 M=NPI,N	MAINC234
	XR=FSHG*C.4/(2.0**(M-2))	MAINC235
	IF(M.EQ.NPI.AND.SSHG.GE.2*(NPI-1))XR=(NPI-1)/SSHG	MAINC236
	KI(M)=XR+KE(M)	MAINC237
	CALL EIGEN(M,CMEGA,KI(M),LARM)	MAINC238
	IF(LARM.EQ.1)GO TO 1CCO	MAINC239
60	CCCONTINUE	MAINC240
70	N1=N-1	MAINC241
	CO 80 M=1,N1	MAINC242
	N2=M+1	MAINC243
	CO 8C MP=N2,N	MAINC244
80	IF(CABS((KI(M)-KI(MP))/(KI(M)+KI(MP))).LT.0.C1)WRITE(6,1140)M,MP	MAINC245
C		MAINC246
C	SOLVE FOR CCEF MATRIX IN ORTHOGONAL INTERFACIAL BCLNDRY CONDITICNS	MAINC247
C		MAINC248
	ESF=EP/(S-IM*F)	MAINC249
	SFE=(S-IM*F-1.0)/EP	MAINC250
	CC 110 MI=1,N	MAINC251
	YC(MI)=ESF*KI(MI)/KE(I)	MAINC252


```

YD(MI)=CEXP(-IM*KI(MI)*B)
YG=KE(1)*KI(MI)/(KI(MI)**2-KE(1)**2)
CRG=KI(MI)
SHK(MI)=CSH(CRG)
CHK=CCH(CRG)
YH=SHK(MI)*CHK/(SHK(MI)*CHK+KI(MI))
YI(MI)=SFE*YC*YH
CC 110 ME=1,N
YA=(KI(MI)**2-KE(1)**2)/(KI(MI)**2-KE(ME)**2)
YB=KE(ME)/KE(1)
YE(MI,ME)=YA*(YB+YC(MI))
110 YF(MI,ME)=YA*(YB-YC(MI))
DO 120 I=1,LIME,2
MI=(I+1)/2
C(I)=1.0-YC(MI)
C(I+1)=1.0+YC(MI)
DO 120 J=1,LIME,2
ME=(J+1)/2
Y(I,J)=YE(MI,ME)
Y(I,J+1)=YF(MI,ME)*YC(MI)
Y(I+1,J)=YF(MI,ME)
120 Y(I+1,J+1)=YE(MI,ME)/YD(MI)
C
C CALL SIMQ TO SOLVE FOR UNKNOWN COMPLEX DIMENSIONLESS AMPLITUDES
C NOTE THAT Y MUST BE DIMENSIONED EXACTLY AS LIMIT BY LIMIT,
C OTHERWISE CONVERT TO COLUMN MATRIX BEFORE CALLING SIMQ
C
C CALL SIMQ(Y,C,LIMIT,KS)
C IF(KS.EQ.0)GC TC 140
C WRITE(6,1150)
C GC TC 1000
C
C ALL COMPLEX AMPLITUDES ARE MADE DIMENSIONLESS BY DIVIDING THROUGH
C BY THE INCIDENT WAVE AMPLITUDE
C
C CR(M),CT(M)=COMPLEX REFLECTED, TRANSMITTED WAVE AMPLITUDES

```

```

MAIN0253
MAIN0254
MAIN0255
MAIN0256
MAIN0257
MAIN0258
MAIN0259
MAIN0260
MAIN0261
MAIN0262
MAIN0263
MAIN0264
MAIN0265
MAIN0266
MAIN0267
MAIN0268
MAIN0269
MAIN0270
MAIN0271
MAIN0272
MAIN0273
MAIN0274
MAIN0275
MAIN0276
MAIN0277
MAIN0278
MAIN0279
MAIN0280
MAIN0281
MAIN0282
MAIN0283
MAIN0284
MAIN0285
MAIN0286
MAIN0287
MAIN0288

```

C	140	CO 15C M=1,N	MAIN0289
		I=2*M	MAIN0290
		CR(M)=C(I-1)	MAIN0291
	150	CT(M)=C(I)	MAIN0292
		CC 170 M=1,N	MAIN0293
C			MAIN0294
C		C1(M),C2(M)=COMPLEX WAVE AMPLITUDES INSIDE BREAKWATER	MAIN0295
C			MAIN0296
		C1(M)=1.C+YC(M)	MAIN0297
		C2(M)=0.0	MAIN0298
		CG 160 ME=1,N	MAIN0299
		C1(M)=C1(M)-CR(ME)*YF(M,ME)	MAIN0300
	160	C2(M)=C2(M)-CT(ME)*YF(M,ME)	MAIN0301
		C1(M)=YI(M)*C1(M)	MAIN0302
		C2(M)=YI(M)*C2(M)	MAIN0303
		C1R(M)=REAL(C1(M))	MAIN0304
		C1I(M)=AIMAG(C1(M))	MAIN0305
		C2R(M)=REAL(C2(M))	MAIN0306
		C2I(M)=AIMAG(C2(M))	MAIN0307
		CRR(M)=REAL(CR(M))	MAIN0308
		CRI(M)=AIMAG(CR(M))	MAIN0309
		CTR(M)=REAL(CT(M))	MAIN0310
		CTI(M)=AIMAG(CT(M))	MAIN0311
C			MAIN0312
C		COMPUTE PHASE OF WAVES	MAIN0313
C			MAIN0314
		PHAZR(M)=ATAN2(CRI(M),CRR(M))*DEGRE	MAIN0315
		PHAZI(M)=ATAN2(C1I(M),C1R(M))*DEGRE	MAIN0316
		PHAZ2(M)=ATAN2(C2I(M),C2R(M))*DEGRE	MAIN0317
		PHAZT(M)=ATAN2(CTI(M),CTR(M))*DEGRE	MAIN0318
			MAIN0319
C			MAIN0320
C		GAMA=REAL PART OF INTERNAL WAVE NO.	MAIN0321
C		BETA=IMAGINARY PART OF INTERNAL WAVE NO.	MAIN0322
C			MAIN0323
		GAMA(M)=REAL(KI(M))	MAIN0324

```

      BETA(M)=-AIMAG(KI(M))
C
C      COMPLTE ABSCLLTE VALUE OF DIMENSIONLESS WAVE AMPLITUDES
C      NOTE REF(1),TRANS(1) ARE THE REFLECTION AND TRANSMISSIION COEFS OF
C      THE BREAKWATER
      REF(M)=CABS(CR(M))
      T1(M)=CABS(CI(M))
      T2(M)=CABS(CZ(M))
170  TRANS(M)=CABS(CT(M))
      DENCM=0.0
C
C      COMPUTE DENOMINATOR IN LORENTZ'S COND. OF EQUIV. WCRK (EXACT INTEGRATION)
C
      DO 180 M=1,N
      AA=1.0/(B*BETA(M)*GAMA(M))
      ARG=2.0*C*GAMA(M)
      ARF=2.0*BETA(M)
      AB=1.0/(CH(ARG)-CCS(AFF))
      AC=(1.0-EXP(-ARF*B))/4.0
      AD=SH(ARG)
      AE=C1R(M)**2+C1I(M)**2+C2R(M)**2+C2I(M)**2
      AF=EXP(-BETA(M)*B)*SIN(ARG)*SIN(GAMA(M)*B)
      AG=C1R(M)*C2F(M)+C1I(M)*C2I(M)
180  DENOM=DENCM+AA*AB*(AC*AD*AE-AF*AG)
      DENCM=2.0*EP*DENCM
C
C      COMPUTE NUMERATOR IN LORENTZ'S COND. OF EQUIV. WCRK(NUMERICAL INTEGRATION)
C
      DO 190 J=1,N
      X=(J-1)*DELX
      DO 190 M=1,N
      C1X(J,M)=C1(M)*CEXP(-IM*KI(M)*X)
190  C2X(J,M)=C2(M)*CEXP(IM*KI(M)*(X-B))
      DO 240 I=1,NZ
      Z=-((I-1)*DELZ
      MAIN0325
      MAIN0326
      MAIN0327
      MAIN0328
      MAIN0329
      MAIN0330
      MAIN0331
      MAIN0332
      MAIN0333
      MAIN0334
      MAIN0335
      MAIN0336
      MAIN0337
      MAIN0338
      MAIN0339
      MAIN0340
      MAIN0341
      MAIN0342
      MAIN0343
      MAIN0344
      MAIN0345
      MAIN0346
      MAIN0347
      MAIN0348
      MAIN0349
      MAIN0350
      MAIN0351
      MAIN0352
      MAIN0353
      MAIN0354
      MAIN0355
      MAIN0356
      MAIN0357
      MAIN0358
      MAIN0359
      MAIN0360

```

	DO 200 M=1,N	MAIN0361
	CRG=KI(M)*(1.0+Z)	MAIN0362
	CZ(I,M)=CCH(CRG)/SHK(M)	MAIN0363
200	SZ(I,M)=IM*CSH(CRG)/SPK(M)	MAIN0364
	DO 240 J=1,N	MAIN0365
	IF(CF(I,J).LT..1E-5)GC TC 230	MAIN0366
	CHI=CMPLX(0.0,0.0)	MAIN0367
	ZETA=CMPLX(0.0,0.0)	MAIN0368
	CO 210 M=1,N	MAIN0369
C		MAIN0370
C	CHI=COMPLEX DIMENSIONLESS HORIZONTAL VELOCITY INSIDE BREAKWATER AT X,Z	MAIN0371
C	ZETA=COMPLEX DIMENSIONLESS VERTICAL VELOCITY INSIDE BREAKWATER AT X,Z	MAIN0372
C		MAIN0373
	CHI=CHI+CZ(I,M)*(C1X(J,M)-C2X(J,M))	MAIN0374
210	ZETA=ZETA+SZ(I,M)*(C1X(J,M)+C2X(J,M))	MAIN0375
	AX=REAL(CHI)	MAIN0376
	EX=AIMAG(CHI)	MAIN0377
	AZ=REAL(ZETA)	MAIN0378
	BZ=AIMAG(ZETA)	MAIN0379
	EAT=AX*AX+AZ*AZ+BX*BX+BZ*BZ	MAIN0380
	ELAM=VISCO/(PERM(I,J)*SIG)	MAIN0381
	ETURB=EPS(I,J)*A*8.0*CF(I,J)*SQRT(EAT)/(SQRT(PERM(I,J))*3.0*PI)	MAIN0382
C		MAIN0383
C	EXZ(I,J)=DIMENSIONLESS FRICTIONAL ENERGY LOSS PER UNIT WEIGHT OF	MAIN0384
C	FLUID AT X,Z	MAIN0385
C		MAIN0386
	EXZ(I,J)=EAT*(ELAM+ETURB)*(EPS(I,J)**2)	MAIN0387
	GC TC 240	MAIN0388
230	EXZ(I,J)=C.C	MAIN0389
240	CONTINUE	MAIN0390
	ANUMR=0.0	MAIN0391
	CO 250 J=1,NJ	MAIN0392
	CO 250 I=1,NI	MAIN0393
250	ANUMR=ANUMR+(EXZ(I,J)+EXZ(I,J+1)+EXZ(I+1,J)+EXZ(I+1,J+1))/4.C	MAIN0394
	ANUMR=ANUMR/(NI*NJ)	MAIN0395
C		MAIN0396

```

C      FC=CALCULATED VALUE OF LINEARIZED DAMPING COEF
C
C      FC=(ANUMR+ELCSS)/DENCF
C
C      COMPARE WITH ASSUMED VALUE AND ITERATE IF NECESSARY
C
C      IF(2.0*ABS(FC-F)/(FC+F).LT.0.01)GC TC 4CC
      WRITE(6,1160)F,FC
      FCC=F
      F=(F+FC)/2.0
      IF(FC.GT.10.*FCC)F=10.*FCC
      IF(FCC.GT.10.*FC)F=FCC/10.
C
C      WRITE OUT INTERMEDIATE SOLUTIONS FOR ASSUMED F
C
C      WRITE(6,1170)
      WRITE(6,1180)(M,KH(M),KI(M),REF(M),PHAZR(M),T1(M),PHAZI(M),T2(M),P
XHAZ2(M),TRANS(M),PHAZT(M),M=1,N)
      GC TC 30
400  WRITE(6,1190)
C
C      WRITE OUT FINAL SOLUTION FOR CLOSED ITERATION
C
C      WRITE(6,1160)F,FC
      WRITE(6,1170)
      WRITE(6,1180)(M,KH(M),KI(M),REF(M),PHAZR(M),T1(M),PHAZI(M),T2(M),F
XHAZ2(M),TRANS(M),PHAZT(M),M=1,N)
      GC TC 590
410  WRITE(6,1200)IFMAX
590  CONTINUE
1000 CONTINUE
1010  FORMAT(5F10.4)
1015  FORMAT(7I5)
1020  FORMAT(27I1)
1030  FORMAT(2F10.5,E10.5)
1040  FORMAT(1H1, 'THE BREAKWATER HAS BEEN DISCRETIZED BELOW THE SWL AS
MAIN0397
MAIN0398
MAIN0399
MAIN0400
MAIN0401
MAIN0402
MAIN0403
MAIN0404
MAIN0405
MAIN0406
MAIN0407
MAIN0408
MAIN0409
MAIN0410
MAIN0411
MAIN0412
MAIN0413
MAIN0414
MAIN0415
MAIN0416
MAIN0417
MAIN0418
MAIN0419
MAIN0420
MAIN0421
MAIN0422
MAIN0423
MAIN0424
MAIN0425
MAIN0426
MAIN0427
MAIN0428
MAIN0429
MAIN0430
MAIN0431
MAIN0432

```

```

XIN THE FOLLOWING DIAGRAM (DO NOT SCALE)')
1C50 FORMAT(1H0,'THERE ARE',I4,' COLUMNS EQUALLY SPACED OVER THE',F6.3,
X' FOOT DISTANCE TCE TC TGE, AND',I4,' ROWS EQUALLY SPACED OVER THE
X',F6.3,' FOOT DEPTH')
1C55 FCRMAT(1HC,'SLOPE CF FRONT FACE = 1/',F4.2)
1C60 FORMAT(1HC,27I3)
1C70 FORMAT(1H0,'EACH NUMBERED LAYER HAS THE FOLLOWING PROPERTIES')
1C80 FCRMAT(1HC,'LAYER NO.   POROSITY   PERMEABILITY (FT**2)   TURBUL
XENT DAMPING COEF.')
```

1C90 FCRMAT(1H ,4X,I2,4X,E13.5,6X,E13.5;11X,E13.5)
1100 FCRMAT(7F10.4)
1110 FORMAT(1HC,'THE EQUIVALENT RECTANGULAR BREAKWATER HAS AN INERTIAL
XCOEFFICIENT =',F6.3,', MEAN POROSITY=',F6.3,', KINEMATIC VISCOSITY
X =',E13.5)
1115 FORMAT(1HC,'SURFACE BREAKING COEF=',F6.3)
1120 FORMAT(1H0,'K*H=',E13.5,', SIGMA**2*H/G=',E13.5,', PERIOD=',E13.5,
X' SECS, WAVE LENGTH =',E13.5,' FEET')
1125 FCRMAT(1H0,'MICHES INTRINSIC REFLECTION CCEF=',F6.3)
1130 FORMAT(1HC,'WAVE CAMBER=',E13.5)
1140 FORMAT(1HC,'MODE NUMBERS',I3,' AND',I3,' ARE IDENTICAL, SO FOLLOWI
XNG SCLUTION IS SINGULAR')
1150 FORMAT(1HC,'SIMQ REJECTS COEFFICIENT MATRIX AS SINGULAR')
1160 FORMAT(1H0,'ASSUMED F=',E13.5,', CALCULATED F=',E13.5)
1170 FORMAT(1HC,' M KF(M) KI(M) REF(M) PHAZ
XR(M) T1(M) PHAZ1(M) T2(M) PHAZ2(M) TRANS(M) PHAZ
XT(M)')
1180 FCRMAT(1H ,I4,11E11.4)
1190 FORMAT(1HC,'F ITERATION CONVERGED, FINAL SOLUTION FOLLOWS *****
X*****')
1200 FORMAT(1HC,'F ITERATION EXCEEDED',I3,' CYCLES, GO TO NEXT CAMBER')
STCF
END

```

MAIN0433
MAIN0434
MAIN0435
MAIN0436
MAIN0437
MAIN0438
MAIN0439
MAIN0440
MAIN0441
MAIN0442
MAIN0443
MAIN0444
MAIN0445
MAIN0446
MAIN0447
MAIN0448
MAIN0449
MAIN0450
MAIN0451
MAIN0452
MAIN0453
MAIN0454
MAIN0455
MAIN0456
MAIN0457
MAIN0458
MAIN0459
MAIN0460
MAIN0461
MAIN0462
MAIN0463
MAIN0464
```

```

SUBROUTINE EIGEN(M,OMEGA,PSI,LAMP)
C
C
C
NEWTON-RAPHSON SOLUTION TO DIMENSIONLESS DISPERSION EQUATION
COMPLEX OMEGA,PSI,SI(60),F(60),CF(60),TH,CEXP,CABS,X,Y
MAX=50
LAMP=0
C
C
C
SI(1)=INITIAL GUESS TO SOLUTION
SI(1)=PSI
DO IC I=1,MAX
X=CEXP(SI(I))
Y=CEXP(-SI(I))
TH=(X-Y)/(X+Y)
C
C
C
F=DIMENSIONLESS DISPERSION EQUATION
CF=DERIVATIVE OF F
F(I)=SI(I)*TH-OMEGA
DF(I)=TH+SI(I)*(1.0-TH**2)
SI(I+1)=(SI(I)-F(I))/DF(I)
IF(CABS((SI(I+1)-SI(I))/SI(I+1)).GT.0.001)GO TO 10
IF(CABS(F(I)/SI(I+1)).LT.0.001)GO TO 20
10 CONTINUE
LAMP=1
WRITE(6,11)M
11 FORMAT(1H0, ' NO SOLUTION FOR MODE NUMBER ',I3)
WRITE(6,12)
12 FORMAT(1H0, ' I          SI(I)          F(I)
X          DF(I)          ')
WRITE(6,13)(I,SI(I),F(I),DF(I),I=1,MAX)
13 FORMAT(1H ,I4,6E13.5)
RETURN
C
C
C
PSI=SOLUTION TO WAVE NO.
20 PSI=SI(I+1)
RETURN
END
EIGN0001
EIGN0002
EIGN0003
EIGN0004
EIGN0005
EIGN0006
EIGN0007
EIGN0008
EIGN0009
EIGN0010
EIGN0011
EIGN0012
EIGN0013
EIGN0014
EIGN0015
EIGN0016
EIGN0017
EIGN0018
EIGN0019
EIGN0020
EIGN0021
EIGN0022
EIGN0023
EIGN0024
EIGN0025
EIGN0026
EIGN0027
EIGN0028
EIGN0029
EIGN0030
EIGN0031
EIGN0032
EIGN0033
EIGN0034
EIGN0035
EIGN0036
EIGN0037
EIGN0038
EIGN0039
EIGN0040

```


C	ELEMENTS.	SIMQ 370	SIMQ0037
C	THE FORWARD SOLUTION TO OBTAIN VARIABLE N IS DONE IN	SIMQ 380	SIMQ0038
C	N STAGES. THE BACK SOLUTION FOR THE OTHER VARIABLES IS	SIMQ 390	SIMQ0039
C	CALCULATED BY SUCCESSIVE SUBSTITUTIONS. FINAL SOLUTION	SIMQ 400	SIMQ0040
C	VALUES ARE DEVELOPED IN VECTOR B, WITH VARIABLE 1 IN B(1),	SIMQ 410	SIMQ0041
C	VARIABLE 2 IN B(2),....., VARIABLE N IN B(N).	SIMQ 420	SIMQ0042
C	IF NO PIVOT CAN BE FOUND EXCEEDING A TOLERANCE OF 0.0,	SIMQ 430	SIMQ0043
C	THE MATRIX IS CONSIDERED SINGULAR AND KS IS SET TO 1. THIS	SIMQ 440	SIMQ0044
C	TOLERANCE CAN BE MODIFIED BY REPLACING THE FIRST STATEMENT.	SIMQ 450	SIMQ0045
C	SIMQ 460	SIMQ0046
C	SIMQ 470	SIMQ0047
C	SIMQ 480	SIMQ0048
C	SIMQ 490	SIMQ0049
C		SIMQ0050
C	SUBROUTINE SIMQ(A,B,N,KS)	SIMQ 520	SIMQ0051
C	COMPLEX A(1),B(1),BIGA,SAVE	SIMQ 540	SIMQ0052
C	FORWARD SOLUTION	SIMQ 550	SIMQ0053
C	TOL=0.0	SIMQ 560	SIMQ0054
C	KS=0,	SIMQ 570	SIMQ0055
C	JJ=-N	SIMQ 580	SIMQ0056
C	DO 65 J=1,N	SIMQ 590	SIMQ0057
C	JY=J+1	SIMQ 600	SIMQ0058
C	JJ=JJ+N+1	SIMQ 610	SIMQ0059
C	BIGA=0	SIMQ 620	SIMQ0060
C	IT=JJ-J	SIMQ 640	SIMQ0061
C	DO 30 I=J,N	SIMQ 660	SIMQ0062
C	SEARCH FOR MAXIMUM COEFFICIENT IN COLUMN	SIMQ 670	SIMQ0063
C	IJ=IT+I	SIMQ 680	SIMQ0064
C	IF(CABS(BIGA)-CABS(A(IJ)))20,30,30	SIMQ 690	SIMQ0065
C	20 BIGA=A(IJ)	SIMQ 700	SIMQ0066
C	IMAX=I	SIMQ 720	SIMQ0067
C	3C CONTINUE	SIMQ 740	SIMQ0068
C	TEST FOR PIVOT LESS THAN TOLERANCE (SINGULAR MATRIX)	SIMQ 750	SIMQ0069
C	IF(CABS(BIGA)-TCL)35,35,40	SIMQ 760	SIMQ0070
C	35 KS=1	SIMQ 780	SIMQ0071
C	RETURN	SIMQ 800	SIMQ0072
C	INTERCHANGE ROWS IF NECESSARY		
C	40 II=J+N*(J-2)		

```

IT=IMAX-J
DO 50 K=J,N
I1=I1+N
I2=I1+IT
SAVE=A(I1)
A(I1)=A(I2)
A(I2)=SAVE
C      DIVIDE EQUATION BY LEADING COEFFICIENT
50 A(I1)=A(I1)/BIGA
SAVE=B(IMAX)
B(IMAX)=B(J)
B(J)=SAVE/BIGA
C      ELIMINATE NEXT VARIABLE
IF(J-N) 55,70,55
55 IQS=N*(J-1)
DO 65 IX=JY,N
IXJ=IQS+IX
IT=J-IX
DO 60 JX=JY,N
IXJX=N*(JX-1)+IX
JJX=IXJX+IT
60 A(IXJX)=A(IXJX)-(A(IXJ)*A(JJX))
65 B(IX)=B(IX)-(B(J)*A(IXJ))
C      BACK SOLUTION
70 NY=N-1
IT=N*N
DO 80 J=1,NY
IA=IT-J
IB=N-J
IC=N
DO 80 K=1,J
B(IB)=B(IB)-A(IA)*B(IC)
IA=IA-N
80 IC=IC-1
RETURN
END
SIMQ 810 SIMQ0073
SIMQ 820 SIMQ0074
SIMQ 830 SIMQ0075
SIMQ 840 SIMQ0076
SIMQ 850 SIMQ0077
SIMQ 860 SIMQ0078
SIMQ 870 SIMQ0079
SIMQ 890 SIMQ0080
SIMQ 910 SIMQ0081
SIMQ 920 SIMQ0082
SIMQ 930 SIMQ0083
SIMQ 940 SIMQ0084
SIMQ 960 SIMQ0085
SIMQ 980 SIMQ0086
SIMQ 990 SIMQ0087
SIMQ1000 SIMQ0088
SIMQ1010 SIMQ0089
SIMQ1020 SIMQ0090
SIMQ1030 SIMQ0091
SIMQ1040 SIMQ0092
SIMQ1050 SIMQ0093
SIMQ1060 SIMQ0094
SIMQ1070 SIMQ0095
SIMQ1090 SIMQ0096
SIMQ1110 SIMQ0097
SIMQ1120 SIMQ0098
SIMQ1130 SIMQ0099
SIMQ1140 SIMQ0100
SIMQ1150 SIMQ0101
SIMQ1160 SIMQ0102
SIMQ1170 SIMQ0103
SIMQ1180 SIMQ0104
SIMQ1190 SIMQ0105
SIMQ1200 SIMQ0106
SIMQ1210 SIMQ0107
SIMQ1220 SIMQ0108

```

```

C
C DATA CARDS FOLLOW
C
C BREAKWATER PARAMETERS
1.0      3.25      1.167      1.5      C.333
 27      8        4        5        6        2        10
C BREAKWATER DESCRETIZATICN SCHEME
11111112222222222221111111
1111122222233322222211111
111222222333333222222111
12222223333444333222221
2323233333444444333323232
333333334444444443333333
3434343444444444443434343
444444444444444444444444444
C LAYER PFOPERTIES
1.0      0.0      .1E1
.434      .282      .482E-5
.439      .295      .1138E-5
.430      .4056     .374E-6
C WAVE NUMBERS
0.5      1.0      1.5      2.0      2.5      3.0
C WAVE CAMBERS
.005      .04

```

```

DATA0001
DATA0002
DATA0003
DATA0004
DATA0005
DATA0006
DATA0007
DATA0008
DATA0009
DATA0010
DATA0011
DATA0012
DATA0013
DATA0014
DATA0015
DATA0016
DATA0017
DATA0018
DATA0019
DATA0020
DATA0021
DATA0022
DATA0023
DATA0024

```

APPENDIX E

DISCRETIZATION OF NONHOMOGENEOUS BREAKWATER CROSS SECTIONS .

The media properties are evaluated at discrete points within the confines of the equivalent rectangular breakwater. This becomes an input to the numerical spatial integration of the numerator in the Lorentz equation (81). The breakwater cross section is discretized in a pattern which adequately samples each layer. A rough rule of thumb is to select a grid size which yields at least two points across the minimum dimension of the thinnest layer. The particular pattern chosen is shown in Figure E. An 8 by 27 scheme is used, each grid being 1.5 inches wide by 2 inches deep. Only half of the pattern is shown because the breakwater is symmetric about the centerline.

There are four distinct layers in this structure (Fig. E): 1 is a triangular wedge of seawater; 2 is a coarse armor-layer material; 3 is an intermediate grade layer; and 4 is a relatively fine central core. Each layer has a unique porosity, permeability, and turbulent damping coefficient. In addition, each grid point is assigned a layer number which identifies the media properties of that point.

The particular technique developed for reading this information into the computer is to input the layer number associated with each point first, and then input the properties of each layer number. One card contains all of the layer numbers for a particular row in the grid. For example, the card representing the third row (I=3) (Fig. E) reads from left to right

111222222233333332222222111.

The entire pattern is presented in Appendix F with a sample of the program output. The layer properties are read in as a short array and properties of each point are assigned internally. Sufficient comment cards are provided in the program to make this clear.

Layer	ϵ	C_f	K_p	d
1	1.0	0.0	1.0	0
2	0.434	0.282	$0.482 \cdot 10^{-5}$	1.37 in.
3	0.439	0.295	$0.1138 \cdot 10^{-5}$	0.774 in.
4	0.430	0.4056	$0.375 \cdot 10^{-6}$	0.382 in.

165

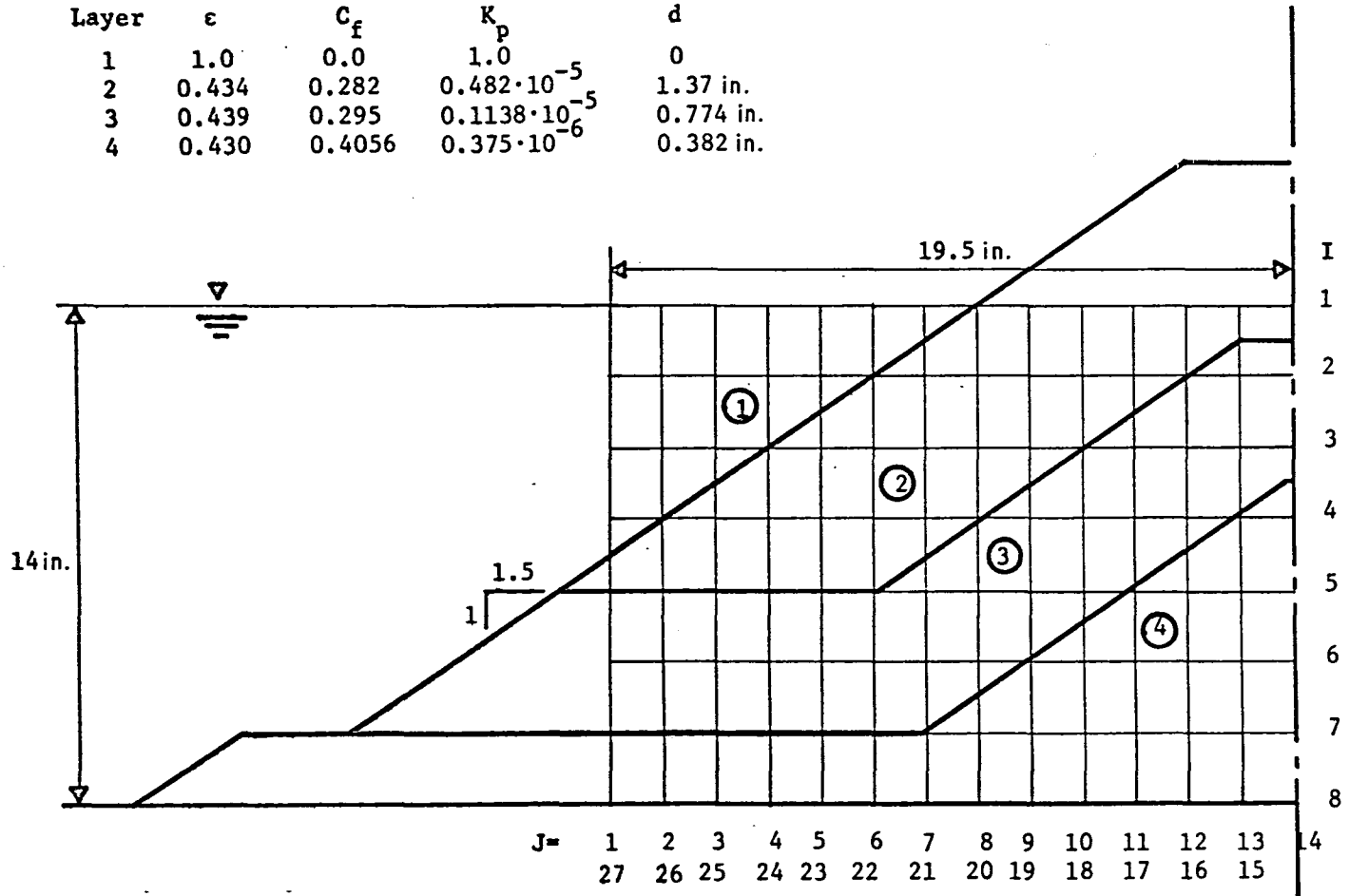


Figure E. Discretization pattern.

APPENDIX F

PERMEABILITY AND FRICTION-FACTOR CALCULATIONS

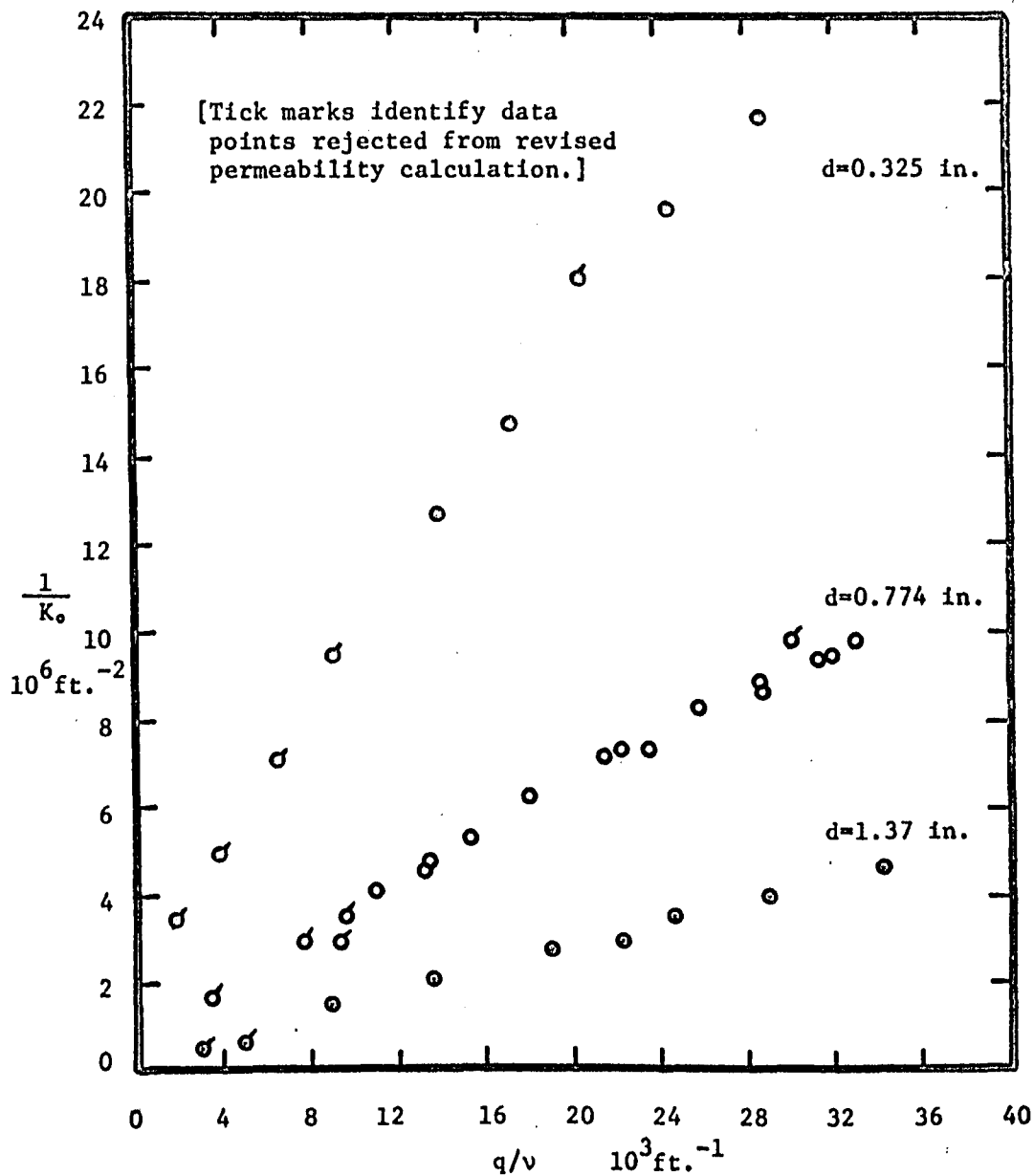


Figure F. Permeability data.

Table F-1. Permeability and friction-factor calculations.

v $\cdot 10^5$ (ft ² /s)	$-\frac{\Delta h}{\Delta l}$	q_d (ft/s)	$\frac{q_d}{v}$ $\cdot 10^{-4}$ (ft ⁻¹)	$\frac{1}{K_{po}} = \frac{-g \frac{\Delta h}{\Delta l}}{v q_d}$ $\cdot 10^{-7}$ (ft ⁻²)	$R_{K_p} = \frac{q_d}{v} K_p^{\frac{1}{2}}$	$f_{K_p} = \frac{-g K_p^{\frac{1}{2}} \frac{\Delta h}{\Delta l}}{q_d^2}$	$C_f = f_{K_p} - \frac{1}{R_{K_p}}$
1.09	0.935	0.1872	1.717	1.475	10.50	0.525	0.430
1.102	1.38	0.224	2.033	1.800	12.43	0.542	0.461
1.09	2.30	0.314	2.881	2.164	17.62	0.459	0.403
1.072	1.71	0.262	2.444	1.960	14.95	0.491	0.424
1.102	0.173	0.0716	0.6497	0.7060	3.97	0.664	0.413
1.102	0.0729	0.0427	0.3875	0.4989	2.37	0.787	0.365
1.053	0.0216	0.0192	0.1823	0.3440	1.12	1.154	0.257
1.118	0.690	0.156	1.395	1.274	8.53	0.588	0.441
1.118	0.339	0.1025	0.9168	0.9526	5.61	0.635	0.457
Least squares yields $K_p = 3.74 \cdot 10^{-7} \text{ ft}^2$							0.406

$d = 0.0271 \text{ feet}$ $\epsilon = 0.430 \text{ feet}$

Table F-2. Permeability and friction-factor calculations.

v *10 ⁵ (ft ² /s)	$-\frac{\Delta h}{\Delta \ell}$	q_d (ft/s)	$\frac{q_d}{v}$ *10 ⁻⁴ (ft ⁻¹)	$\frac{1}{K_{po}} = \frac{-g \frac{\Delta h}{\Delta \ell}}{v q_d}$ *10 ⁻⁶ (ft ⁻²)	$R_{K_p} = \frac{q_d}{v} K_p^{1/2}$	$f_{K_p} = \frac{-g K_p^{1/2}}{q_d^2} \frac{\Delta h}{\Delta \ell}$	$C_f = f_{K_p} - \frac{1}{R_{K_p}}$
1.04	0.0050	0.0311	0.2990	0.4978	8.79	0.489	0.375
1.063	0.01043	0.0528	0.4967	0.5984	14.60	0.354	0.286
1.072	0.0467	0.0957	0.8927	1.466	26.24	0.483	0.444
1.053	0.0951	0.1431	1.359	2.032	39.94	0.440	0.414
1.053	0.181	0.2005	1.904	2.761	55.96	0.426	0.408
1.090	0.230	0.2325	2.133	2.922	62.69	0.403	0.387
1.090	0.320	0.268	2.459	3.527	72.26	0.422	0.408
1.072	0.411	0.310	2.892	3.982	84.99	0.405	0.393
1.102	0.602	0.377	3.421	4.666	100.55	0.401	<u>0.391</u>
Least squares yields $K_p = 8.64 \cdot 10^{-6} \text{ ft}^2$							0.390

$d = 0.114 \text{ feet}$ $c = 0.434 \text{ feet}$

Table F-3. Permeability and friction-factor calculations.

v $\cdot 10^5$ (ft ² /s)	$-\frac{\Delta h}{\Delta \ell}$	q_d (ft/s)	$\frac{q_d}{v}$ $\cdot 10^{-4}$ (ft ⁻¹)	$\frac{1}{K_{po}} = \frac{-g \frac{\Delta h}{\Delta \ell}}{v q_d}$ $\cdot 10^{-6}$ (ft ⁻²)	$R_{K_p} = \frac{q_d}{v} K_p^{1/2}$	$f_{K_p} = \frac{-g K_p^{1/2}}{q_d^2} \frac{\Delta h}{\Delta \ell}$	$C_f = f_{K_p} - \frac{1}{R_{K_p}}$
1.053	0.0196	0.0366	0.3476	1.638	3.703	0.503	0.233
1.058	0.118	0.102	0.9641	3.521	10.28	0.390	0.292
1.053	0.207	0.138	1.311	4.587	13.98	0.373	0.302
1.053	0.534	0.227	2.156	7.194	23.00	0.356	0.312
1.063	0.568	0.236	2.220	7.291	23.68	0.350	0.308
1.063	0.876	0.306	2.879	8.672	30.71	0.321	0.289
1.058	0.890	0.304	2.873	8.910	30.65	0.331	0.298
1.058	1.048	0.338	3.195	9.437	34.08	0.315	0.286
1.063	1.042	0.321	3.020	9.833	32.21	0.347	0.316
1.058	1.028	0.332	3.138	9.424	33.47	0.320	0.290
1.063	1.132	0.350	3.293	9.797	35.12	0.317	0.289
1.053	0.388	0.190	1.804	6.245	19.25	0.369	0.317
1.058	0.744	0.272	2.571	8.325	27.42	0.345	0.309
1.058	0.599	0.248	2.344	7.351	25.00	0.334	0.295
1.042	0.091	0.0956	0.9175	2.942	9.79	0.342	0.240
1.058	0.223	0.142	1.342	4.780	14.23	0.380	0.310
1.053	0.0779	0.0802	0.7616	2.970	8.12	0.416	0.293
1.053	0.280	0.161	1.527	5.325	16.29	0.372	0.311
1.053	0.156	0.116	1.104	4.105	11.77	0.397	0.312
Least squares yields $K_p = 1.14 \cdot 10^{-6}$ ft ²							0.295

$d = 0.0645$ feet $\epsilon = 0.439$ feet

Table F-4. Permeability and friction-factor calculations.

v *10 ⁵ (ft ² /s)	$-\frac{\Delta h}{\Delta l}$	q_d (ft/s)	$\frac{q_d}{v}$ *10 ⁻⁴ (ft ⁻¹)	$\frac{1}{K_{po}} = \frac{-g\frac{\Delta h}{\Delta l}}{vq_d}$ *10 ⁻⁶ (ft ⁻²)	$R_{K_p} = \frac{q_d}{v} K_p^{\frac{1}{2}}$	$f_{K_p} = \frac{-gK_p^{\frac{1}{2}}}{q_d^2} \frac{\Delta h}{\Delta l}$	$C_f = f_{K_p} - \frac{1}{R_{K_p}}$
1.053	0.207	0.138	1.311	4.587	11.11	0.297	0.207
1.053	0.534	0.227	2.156	7.194	18.28	0.283	0.228
1.063	0.568	0.236	2.220	7.291	18.82	0.278	0.225
1.063	0.876	0.306	2.877	8.672	24.41	0.255	0.214
1.058	0.89	0.304	2.873	8.910	24.36	0.263	0.222
1.058	1.048	0.338	3.195	9.437	27.09	0.251	0.214
1.058	1.028	0.332	3.138	9.424	26.61	0.255	0.217
1.063	1.132	0.350	3.293	9.797	27.92	0.252	0.216
1.053	0.388	0.190	1.804	6.245	15.30	0.293	0.228
1.058	0.744	0.272	2.571	8.325	21.80	0.275	0.229
1.058	0.599	0.248	2.344	7.351	19.88	0.266	0.215
1.058	0.223	0.142	1.342	4.780	11.38	0.302	0.214
1.053	0.280	0.161	1.527	5.325	12.95	0.296	0.218
1.053	0.156	0.1162	1.104	4.105	9.36	0.315	0.209
Least squares yields $K_p = 7.19 \cdot 10^{-7} \text{ ft}^2$							0.218

$d = 0.0271 \text{ feet}$ $\epsilon = 0.439 \text{ feet}$

Table F-5. Permeability and friction-factor calculations.

v *10 ⁵ (ft ² /s)	$-\frac{\Delta h}{\Delta l}$	q_d (ft/s)	$\frac{q_d}{v}$ *10 ⁻⁴ (ft ⁻¹)	$\frac{1}{K_{po}} = \frac{-g \frac{\Delta h}{\Delta l}}{v q_d}$ *10 ⁻⁷ (ft ⁻²)	$R_{K_p} = \frac{q_d}{v} K_p^{1/2}$	$f_{K_p} = \frac{-g K_p^{1/2} \Delta h}{q_d^2 \Delta l}$	$C_f = f_{K_p} - \frac{1}{R_{K_p}}$	
1.09	0.935	0.1872	1.717	1.475	8.63	0.432	0.316	
1.09	2.3	0.314	2.881	2.164	14.48	0.378	0.309	
1.072	1.71	0.262	2.444	1.960	12.29	0.403	0.322	
1.118	0.339	0.1025	0.917	0.953	4.61	0.522	0.306	
1.118	0.690	0.156	1.395	1.274	7.01	0.459	<u>0.316</u>	
Least squares yields $K_p = 2.53 \cdot 10^{-7} \text{ ft}^2$								0.314

$d = 0.0271 \text{ feet}$ $\epsilon = 0.430 \text{ feet}$

Table F-6. Permeability and friction-factor calculations.

v *10 ⁵ (ft ² /s)	$-\frac{\Delta h}{\Delta l}$	q_d (ft/s)	$\frac{q_d}{v}$ *10 ⁻⁴ (ft ⁻¹)	$\frac{1}{K_{po}} = \frac{-g \frac{\Delta h}{\Delta l}}{v q_d}$ *10 ⁻⁶ (ft ⁻²)	$R_{K_p} = \frac{q_d}{v} K_p^{1/2}$	$f_{K_p} = \frac{-g K_p^{1/2} \Delta h}{q_d^2 \Delta l}$	$C_f = f_{K_p} - \frac{1}{R_{K_p}}$	
1.072	0.0467	0.0957	0.8927	1.466	15.96	0.294	0.231	
1.053	0.0951	0.1431	1.359	2.032	24.30	0.267	0.226	
1.053	0.181	0.2005	1.904	2.761	34.04	0.259	0.230	
1.09	0.230	0.2325	2.133	2.922	38.14	0.244	0.219	
1.09	0.320	0.268	2.459	3.527	43.96	0.256	0.234	
1.072	0.411	0.310	2.892	3.982	51.70	0.246	0.227	
1.102	0.602	0.377	3.421	4.666	61.17	0.244	<u>0.228</u>	
Least squares yields $K_p = 3.20 \cdot 10^{-6} \text{ ft}^2$								0.228

$d = 0.114 \text{ feet}$ $\epsilon = 0.434 \text{ feet}$

APPENDIX G

WAVE DATA FOR TRAPEZOIDAL-LAYERED BREAKWATER

Table G. Wave data for trapezoidal-layered breakwater.

Run No.	h (ft)	T (s)	L (ft)	$kh = \frac{2\pi h}{L}$	H_{max} (ft)	H_{min} (ft)	$C_R = \frac{H_{max} - H_{min}}{H_{max} + H_{min}}$	$H_I = \frac{H_{max} + H_{min}}{2}$ (ft)	H_T (ft)	$C_T = \frac{H_T}{H_I}$	$\frac{H_I}{L}$
419	1.167	1.376	7.36	0.995	0.150	0.08	0.304	0.115	0.019	0.165	0.0156
420					0.120	0.065	0.297	0.0926	0.017	0.183	0.0126
421					0.088	0.048	0.294	0.0680	0.0140	0.208	0.0092
422					0.062	0.034	0.292	0.0480	0.0115	0.240	0.0065
423					0.038	0.020	0.312	0.0290	0.0085	0.293	0.0039
424					0.084	0.046	0.292	0.065	0.0140	0.216	0.0088
425					0.018	0.008	0.385	0.0130	0.005	0.385	0.0018
426					0.160	0.088	0.290	0.124	0.0180	0.145	0.0169
427	1.167	2.488	14.65	0.500	0.088	0.024	0.571	0.056	0.016	0.286	0.0038
428					0.056	0.015	0.578	0.0355	0.0115	0.324	0.0024
429					0.057	0.016	0.562	0.0365	0.0125	0.342	0.0025
430					0.075	0.020	0.580	0.0474	0.014	0.296	0.0032
431	1.167	1.025	4.88	1.500	0.115	0.072	0.230	0.094	0.0092	0.098	0.0192
432					0.145	0.090	0.234	0.117	0.0115	0.098	0.0240
433					0.160	0.105	0.208	0.133	0.011	0.083	0.0273
434					0.200	0.135	0.194	0.167	0.0120	0.072	0.0342
435					0.095	0.060	0.226	0.0775	0.010	0.129	0.0159
436					0.075	0.045	0.250	0.060	0.0082	0.137	0.0123
437					0.054	0.032	0.256	0.0430	0.0072	0.167	0.00901
438					0.030	0.017	0.277	0.0235	0.0056	0.238	0.0043
439	1.167	0.860	3.65	2.01	0.037	0.022	0.254	0.0295	0.0050	0.169	0.0081
440					0.062	0.040	0.216	0.0510	0.0060	0.118	0.0140
441					0.090	0.060	0.200	0.075	0.0065	0.0867	0.0206
442					0.115	0.078	0.192	0.0965	0.0072	0.0746	0.0274
443					0.135	0.095	0.174	0.115	0.0074	0.0644	0.0315
444					0.157	0.111	0.172	0.134	0.0073	0.0545	0.0368
445					0.175	0.125	0.167	0.1500	0.0075	0.500	0.0411
446					0.195	0.142	0.157	0.168	0.0078	0.0460	0.0461
447					0.215	0.155	0.162	0.185	0.0081	0.0437	0.0506
448					0.024	0.0130	0.298	0.0185	0.0031	0.168	0.00506
449	1.167	0.688	2.42	3.02	0.0250	0.0120	0.351	0.0185	0.0015	0.081	0.00765
450					0.037	0.018	0.345	0.0275	0.0017	0.062	0.0114
451					0.065	0.035	0.300	0.050	0.0017	0.034	0.0206
452					0.088	0.048	0.294	0.068	0.0020	0.029	0.0281
453					0.125	0.065	0.316	0.095	0.0026	0.029	0.0392
454					0.161	0.080	0.336	0.120	0.0030	0.025	0.0496
455					0.175	0.092	0.311	0.133	0.0030	0.023	0.055
456	1.167	0.760	2.92	2.51	0.155	0.112	0.161	0.133	0.0051	0.038	0.0456
457					0.175	0.130	0.147	0.153	0.0050	0.033	0.0525
458					0.200	0.150	0.143	0.175	0.0052	0.030	0.0600
459					0.130	0.092	0.171	0.111	0.0045	0.041	0.0380
460					0.112	0.080	0.167	0.096	0.0042	0.044	0.0329
461					0.090	0.060	0.200	0.075	0.0040	0.053	0.0257
462					0.062	0.040	0.216	0.051	0.0032	0.063	0.0175
463					0.042	0.027	0.217	0.035	0.0025	0.072	0.0120
464					0.028	0.018	0.217	0.023	0.0020	0.087	0.00788
465	1.167	2.488	14.65	0.500	0.305	0.100	0.506	0.202	0.0365	0.181	0.0138
466					0.380	0.140	0.462	0.260	0.0400	0.154	0.0178
467					0.450	0.170	0.452	0.310	0.044	0.142	0.0212
468					0.530	0.220	0.414	0.374	0.048	0.128	0.0255
469					0.245	0.080	0.508	0.162	0.032	0.198	0.0111
470					0.180	0.050	0.565	0.115	0.026	0.226	0.00785
471					0.118	0.032	0.573	0.0750	0.021	0.280	0.00511
472					0.065	0.016	0.605	0.0405	0.013	0.321	0.00276

Sollitt, Charles K.

Wave reflection and transmission at permeable breakwaters / by Charles K. Sollitt and Ralph H. Cross III. - Fort Belvoir, Va. : U.S. Coastal Engineering Research Center, 1976.

172 p. : ill. (Technical paper - Coastal Engineering Research Center ; DACW72-68-C-0032)

Bibliography: p. 133-136.

Results of an investigation to develop a theoretical analysis to account for wave reflection and transmission at permeable breakwaters are presented. The effectiveness of alternative breakwater configurations independent of repetitive experimental programs is compared.

1. Breakwaters. 2. Wave reflection. 3. Wave propagation.
I. Title. II. Cross, Ralph H., joint author. III. Series: U.S. Coastal Engineering Research Center. Technical paper no. 76-8. IV. U.S. Coastal Engineering Research Center. Contract DACW72-68-C-0032.

TC203 .U581tp no. 76-8 627 .U581tp

Sollitt, Charles K.

Wave reflection and transmission at permeable breakwaters / by Charles K. Sollitt and Ralph H. Cross III. - Fort Belvoir, Va. : U.S. Coastal Engineering Research Center, 1976.

172 p. : ill. (Technical paper - Coastal Engineering Research Center ; DACW72-68-C-0032)

Bibliography: p. 133-136.

Results of an investigation to develop a theoretical analysis to account for wave reflection and transmission at permeable breakwaters are presented. The effectiveness of alternative breakwater configurations independent of repetitive experimental programs is compared.

1. Breakwaters. 2. Wave reflection. 3. Wave propagation.
I. Title. II. Cross, Ralph H., joint author. III. Series: U.S. Coastal Engineering Research Center. Technical paper no. 76-8. IV. U.S. Coastal Engineering Research Center. Contract DACW72-68-C-0032.

TC203 .U581tp no. 76-8 627 .U581tp

Sollitt, Charles K.

Wave reflection and transmission at permeable breakwaters / by Charles K. Sollitt and Ralph H. Cross III. - Fort Belvoir, Va. : U.S. Coastal Engineering Research Center, 1976.

172 p. : ill. (Technical paper - Coastal Engineering Research Center ; DACW72-68-C-0032)

Bibliography: p. 133-136.

Results of an investigation to develop a theoretical analysis to account for wave reflection and transmission at permeable breakwaters are presented. The effectiveness of alternative breakwater configurations independent of repetitive experimental programs is compared.

1. Breakwaters. 2. Wave reflection. 3. Wave propagation.
I. Title. II. Cross, Ralph H., joint author. III. Series: U.S. Coastal Engineering Research Center. Technical paper no. 76-8. IV. U.S. Coastal Engineering Research Center. Contract DACW72-68-C-0032.

TC203 .U581tp no. 76-8 627 .U581tp

Sollitt, Charles K.

Wave reflection and transmission at permeable breakwaters / by Charles K. Sollitt and Ralph H. Cross III. - Fort Belvoir, Va. : U.S. Coastal Engineering Research Center, 1976.

172 p. : ill. (Technical paper - Coastal Engineering Research Center ; DACW72-68-C-0032)

Bibliography: p. 133-136.

Results of an investigation to develop a theoretical analysis to account for wave reflection and transmission at permeable breakwaters are presented. The effectiveness of alternative breakwater configurations independent of repetitive experimental programs is compared.

1. Breakwaters. 2. Wave reflection. 3. Wave propagation.
I. Title. II. Cross, Ralph H., joint author. III. Series: U.S. Coastal Engineering Research Center. Technical paper no. 76-8. IV. U.S. Coastal Engineering Research Center. Contract DACW72-68-C-0032.

TC203 .U581tp no. 76-8 627 .U581tp